# THÈSE DE DOCTORAT

Numéro national de thèse/suffixe local

Soutenue à Aix-Marseille Université
Le 01/10/2021 par

**Mehrnaz Modaresialam-Bochet**

# Fabrication of dielectric nanostructures by Nano Imprint Lithography and sol-gel chemistry for optical applications

**Discipline**

**Spécialité**
PHYSIQUE-SCIENCES DE LA MATIERE CONDENSEE& NANOSCIENCE

**École doctorale**
Ecole doctorale 352 Physique et science de la matière

**Laboratoire/Partenaires de recherche**
Institut Matériaux Microélectronique et Nanosciences de Provence

| | |
|---|---|
| Prof. Yves Jourlin<br>Université St- Etienne | Rapporteur |
| Pro. Christophe Sinturel<br>Université d'Orléans | Rapporteur |
| Dr. Magali Putero<br>Université Aix-Marseille | Examinateur |
| Prof. Thierry Djenizian<br>Université mine St- Etienne | Examinateur |
| Dr. Lionel Santinacci<br>Université Aix-Marseille | Examinateur |
| Prof. David Grosso<br>Université Aix-Marseille | Directeur de thèse |
| Dr. Marco.Abbarchi<br>Université Aix-Marseille | Co-Directeur de thèse |

# AFFIDAVIT

I, undersigned, Mehrnaz Modaresialam-Bochet, hereby declare that the work presented in this manuscript is my own work, carried out under the scientific direction of Prof. David Grosso and Dr. Marco Abbarchi, in accordance with the principles of honesty, integrity and responsibility inherent to the research mission. The research work and the writing of this manuscript have been carried out in compliance with both the French national charter for Research Integrity and the Aix-Marseille University charter on the fight against plagiarism.

This work has not been submitted previously either in this country or in another country in the same or in a similar version to any other examination body.

Marseille, 30 juin 2021

# RESUME

Le but de cette thèse est de développer des méthodes d'élaboration de métasurfaces nanostructurées par combinaison de la Chimie Sol-gel et de la Lithographie par Nano Impression (soft-NIL). Celle-ci présente notamment des intérêts d'ordres scientifiques et technologiques. En outres, elle entre dans la tendance générale du développement des processus rapide à faibles couts utilisant des matériaux biocompatibles et non toxiques. Dans un premier temps, nous présenterons l'élaboration de nouveaux revêtements antireflets constitués de silice hydrophobe (modifiée méthyle) avec différentes nanostructures (piliers et trous). Ces nouveaux revêtements permettent de réduire la réflexion dans un intervalle spectral large tout en conservant une large tolérance angulaire à la lumière incidente. D'autre part, ces nanomatériaux présentent une stabilité chimique, thermique et mécanique améliorée par rapport à l'état de l'art. Par la suite, un nouveau système de couche sensible composé d'une métasurface de $TiO_2$ encapsulée dans une matrice hybride microporeuse pour capteur basée sur la transduction optique, et présentant une sensibilité spectrale de 4470 nm/RIU a été développé. Ce dernier a été exploiter pour sonder a présence de COV dans l'air avec une sélectivité partielle et une sensibilité de $0.5\times10^{-3}$ R/ppm. Finalement, le savoir-faire développé a ensuite été mis à contribution pour l'élaboration de réseaux de métasurfaces par empilements successifs de matériaux diélectriques $SiO_2$ poreuse et $TiO_2$ dense nano imprimés. Ce dernier travail est précurseur à la fabrication de méta matériaux 3D par procédé sol-gel.

# ABSTRACT

The purpose of this thesis is to develop methods to elaborate nanostructured metasurfaces by combining sol-gel chemistry and Nano Imprint Lithography (soft-NIL), which are of relevant scientific and technological interest as they inscribe themselves in the general trend of developing affordable and time-saving processes, using biocompatible and non-toxic materials. Firstly, we showcase the elaboration of new efficient antireflection coatings made of water-repellent methylated-silica nipple-dimple nano-architectures (pillars and holes). The interest of these results relies on the possibility to drastically reduce reflection in a broad spectral interval and within a broad acceptance angle of the incident light, rendering them adapted to photovoltaic, glass covers, laser windows, and much more. Furthermore, these nano-materials feature a high chemical, thermal and mechanical stability. Secondly, a highly sensitive optical gas sensor was elaborated based on $TiO_2$ nanopatterns embedded in a thin microporous hybrid-$SiO_2$ sensitive coating. The reflectivity of the layer has then been measured in the visible range with increasing vapor pressure. The measured sensing performances are sensitivity *S* up to 4500 nm/RIU (0.2 nm/ppm), reflection intensity changes up to R* = 17 ($0.55\times10^{-3}$ R/ppm), *FOM* up to 12, with a *Q*-Factor of 4 for a specific wavelength, which is compatible with sub-ppm gas detection by simple specular reflection. Finally, a novel generation of dielectric 3D stack nanostructured patterns (*e.g.* $TiO_2$ pillars - mesoporous $SiO_2$ - $TiO_2$ pillars) was developed as an innovative optical system that has never been experimentally studied before.

# ACKNOWLEDGE

The IM2NP laboratory (*'Equipe NOVA'*) at the University of Aix-Marseille in France carried out this Ph.D. research.

Prof. David Grosso, my director, deserves nothing but the highest praise. Thank you for your help throughout my thesis, your availability, and your willingness to include me in many projects. Thank you for your trust and all of your suggestions and scientific talks, which have always helped me focus my experimental effort. I've always been impressed by your enthusiasm and the amount of energy you exude not only in science but also in sport and music.

I'd also like to express my gratitude to Dr. Marco Abbarchi, my co-director. Thank you for your unwavering support, friendliness, and availability, as well as your patience with me and my inquiries during my Ph.D. He is not only my boss but also the guy I can turn to if I have a problem during these three years. The person who I can feel secure and calm working beside him. I appreciate the time and kindness he spent in our group. Thank you for assisting me in refining my scientific skills and orienting my research perspective. They regarded me as a scientist who was methodical, precise, and insightful.

Prof. Yves Jourlin and Prof. Christophe Sinturel have graciously agreed to serve as the thesis reporters. I'd also like to express my gratitude to Dr. Magali Putero, Dr. Lionel Santinacci, and Prof. Thierry Djenizian for accepting to examine my Ph.D. results.

I am appreciative for all of the facilities provided in the Aix-Marseille laboratory and the cleanroom in IM2NP, as well as all of the assistance and generosity of the entire *'Equipe NOVA,'* particularly Dr. Luc Favre, for his time and attention to devote to SEM imaging.

I'd like to express my gratitude to Dr. Zeinab Chehadi, Dr. Jean-Benoit, Claude, Dr. Jerome Loizillon, Dr. Nasser Benali, and Dr. Mohammed Bouabdellaoui for their friendship and scientific support during my thesis. Thank you for being available to me for as long as I needed you. I appreciate working with you, and I am glad for the opportunity to be surrounded by such wonderful people in my field. I'll never forget everything we did together, from chemistry to parties, cooking, traveling, and music performing.

On the administrative side, I'd like to express my gratitude to Mrs. Michele Francia and Veronique Buat, the doctoral school's secretaries, and Mrs. Delphine Sturma, IM2NP's human resource department. I'd want to express my gratitude for your assistance and valuable administrative suggestions.

I'd like to convey my gratitude to my husband, who has been patient, kind, and encouraging throughout these three years in all facets of my life.

This thesis is dedicated to my mother and father. I would not be where I am today without them, and I would not have completed this significant assignment in my life. Thank you to my mother for always teaching me how to be a motivated, strong woman and to my father for believing in me in whatever I do. Thank you for your support, encouragement, and belief in my ability to be educated and successful at any point in my life. Finally, I'd like to express my gratitude to anyone I may have forgotten.

# Table of content


AFFIDAVIT 3
RÉSUMÉ 5
ABSTRACT 7
ACKNOWLEDGE 9
GENERAL INTRODUCTION 1
INTRODUCTION GÉNÉRALE 3
CHAPTER 1: NANO-IMPRINT LITHOGRAPHY PROCESSING OF INORGANIC-BASED MATERIALS 10
1. Generalities 11
1.1. Nanofabrication techniques and Nano Imprint Lithography (NIL) 11
2. Nano Imprint Lithography (NIL) Methods 17
2.1. UV-NIL 17
2.2. Thermal NIL 18
2.3. Direct printing 22
3. Applications 23
3.1. Photonic Crystals 23
3.2. Solar cells 24
3.3. LEDs 25
3.4. Sensors 25
3.5. Anti-reflection coatings 26
4. Conclusion 27
5. References 28
CHAPTER 2: METHYLATED SILICA SURFACES HAVING TAPERED NIPPLE-DIMPLE NANO-PILLAR MORPHOLOGIES AS ROBUST, BROAD-ANGLE, AND BROADBAND ANTI-REFLECTION COATINGS 32
1. Introduction 33
2. Experimental part 35
2.1. Thin-film Methylated silica ($Si_4O_7Me_2$) preparation 35
2.2. Preparation of the nanopatterned ARC morphologies by environmental control T-NIL 35
3. Optical performance 39
3.1. Abrasion resistance 42
3.2. Thermal resistance 44
3.3. Chemical resistance 45
4. Conclusion 47
5. References 48
CHAPTER 3: SOL-GEL $TiO_2$ NANOIMPRINTED METASURFACE COMBINED TO HYBRID-SILICA SENSITIVE LAYERS WITH HIGH REFRACTIVE INDEX SENSITIVITY AND SELECTIVITY FOR GAS SENSING 51
1. Introduction 52
2. Experimental section 55
2.1. Preparation of hybrid-silica (H-$SiO_2$) sensitive plain coatings 55
2.2. Investigation of gas adsorption in the plain sensitive layer 55
2.3. Preparation of H-$SiO_2$/$TiO_2$ nanostructured composite system by environmental control T-NIL 58

3. Specular reflection of nanostructured sensitive layer composite systems 61
4. Conclusion 65
5. References 66
CHAPTER 4: 2D AND 3D (NANOSTRUCTURED PATTERNS) MULTI-STACK $TiO_2$ COMBINED WITH LOW REFRACTIVE INDEX MESOPOROUS METHYLATED SILICA THIN FILM BY SOL-GEL CHEMISTRY AND NANO IMPRINT LITHOGRAPHY 68
1. Introduction 69
2. Experimental section 71
2.1. Investigation of multi-stack thin films of mesoporous methylated silica and dense titania 71
2.2. Fabrication of 3D double-stack super-imposed nanopatterns by replication of $TiO_2$ nanostructures combined with meso-MS thin layer by pressure and environmental control T-NIL 75
3. Optical investigation 79
4. Conclusion 81
5. References 82
GENERAL CONCLUSION AND PERSPECTIVES 84
APPENDIX 1 87
1) The general concept of sol-gel chemistry 87
2) Liquid deposition technique 88
3) Dip coating 88
4) Spin coating 90
5) Evaporation Induced Self-Assembly 90
6) Micro-contact printer machine 91
APPENDIX 2 : OPTICAL CHARACTERIZATION 93
1) Ellipsometry 93
2) Environmental ellipsometry 94
3) Atomic Force Microscopy (AFM) 94
4) Spectroscopy, Spectrophotometry, and Goniometer 95
References 96
PUBLICATIONS AND CONFERENCES 98

# GENERAL INTRODUCTION

Nanoworld is a magnificent world where science and technology coexist in harmony. With a thorough understanding of nanotechnology, scientists have been able to achieve astonishing elaboration in a variety of applications. Nanoscience is now influencing the production, design, development of industrially important applications such as anti-reflective coatings, and photovoltaics solar cells, chemical/biological sensors, LED, C-MOS cameras, aeronautical, horology, intelligent textiles, biomedical and so forth.

Researchers, inspired by nature structure (*e.g.* some insect morphologies), are attempting to integrate the chemistry aspect of materials in order to develop nanofabrication in one, two- and three-dimension surfaces, in optics and photonics. Optics and photonics are important areas of scientific study that have a wide range of applications. As a result, a lot of work is being put into developing new techniques and practical ways of fabricating and manipulating light in order to expand the application possibilities.

In micro or nanoscale surfaces, the nanofabrication process transforms flat surfaces into three-dimensional patterns. This feat is based on two types of techniques: top-down and bottom-up. In the top-down approach, nanostructures are fabricated from bulk materials and are then templated for instance by lithography. The large majority of the nanofabrication techniques (in term of industrial use) falls into this category. Indeed, will focus on the study of selected lithography technique such as Nano Imprint Lithography (NIL). Nanostructures are also produced from the assembly of molecular building pieces in a bottom-up manner. This enables the creation of buildings with little scale or resolution constraints but confined to simple designs and short-range homogeneity.

The goal of this thesis is to develop the NIL process for/with sol-gel coating by combining a unique perspective on manufacturing originating from multiple chemical-physical situations. Furthermore, we show that boosting fabrication throughput and obtaining nanostructures in wide areas is possible. Improvements in the field of nanomanufacturing techniques will then be used in the burgeoning field of photonics in R&D for industrial productions. As a result, an important part of the R&D effort is devoted to meeting such requirements in order to acquire more minor features on larger surfaces at a cost that is suitable with industrial standards. Combining top-down and bottom-up approaches in a synergetic manner is a promising field in this regard, rising new technical advancements.

The Ph.D. is divided into four chapters.

**Chapter 1** is a compilation of the state-of-the-art nanofabrication as well as research into NIL surface texturing and material science during the last few decades. First, a brief overview of nanofabrication and recently developed Nano Imprint Lithography (NIL) is described. The main categories of NIL approaches are then outlined, followed by a comparison of the resolution and throughput of replicated surfaces. In the second section,

we'll look at how the steady and continual growth of nanofabrication is concocted and studied using various materials and processes each year. Furthermore, various important studies detail the performance, difficulties, and simplicity of implementation of relevant applications.

**Chapter 2** is dedicated to the improvements in NIL applied to the sol-gel coatings process and its application. The absolute replication of high aspect ratio nano-metric structures on a large glass surface area is achieved using the high throughput, fast, and effective NIL method: 'environmental control thermal NIL.' By introducing the resilient, chemically, thermally, and broad-angle Anti-Reflection Coating (ARC) surface for industry and photovoltaic ARC surfaces, the method's scalability, and cost-effectiveness are confirmed.

The goal of **Chapter 3** was to use a unique system of all-dielectric high aspect ratio nanostructure arrays fabricated by NIL and placed in a sensitive sol-gel thin layer atop nanopatterns to enhance gas sensing sensitivity. This nanocomposite optical transduction system has demonstrated improved performance in refractive index variation sensitivity while the selected microporous hybrid silica sensitive elements showed an interesting partial selectivity in gas sensing. A brief analysis of gas sensitivity based on altering inlet gas concentration (nm/ppm) is also detailed; nevertheless, it is far off from the thesis' primary points.

**Chapter 4** introduced the concept of multi-stack refractive index contrast initially as a multilayer film and then framed into super-positioned nanostructure patterns as an open path for revolutionary NIL manufacturing via the sol-gel chemistry process. The NIL fabrication machine is shown to be an efficient system for controlling the alignment of the imposed nanopatterns atop each other. Furthermore, the hexagonal diffraction of moiré patterning is revealed in this multi-stack 3D-imposed nanostructures, indicating improved optical performance across a variety of application domains. This chapter, on the other hand, required additional in-depth investigation and parameter adjustment, which were not included in this work. As a result of the preliminary findings in this chapter, we can chart a new course for future optimization and manufacturing.

Finally, the work's **conclusions and perspectives** are offered. The numerous explanations of methodologies and characterization devices utilized in this thesis are gathered in an **appendix**. Furthermore, at the end of this article, transcriptions of publications and conference participation completed during this thesis are provided.

# INTRODUCTION GENERALE

Le nanomonde est un monde où la science et la technologie coexistent en harmonie.

Grâce à une compréhension approfondie de la nanotechnologie, les scientifiques ont été en mesure de réaliser d'étonnantes découvertes d'ordres fondamentales et applicatives dans des domaines très variés. Les nanosciences influencent désormais la production, la conception et le développement d'applications industrielles importantes telles que les revêtements antireflets, les cellules solaires photovoltaïques, les capteurs chimiques/biologiques, les LED, les caméras C-MOS, l'horlogerie fine, les textiles intelligents, les agents de traitement et d'imagerie médical, *etc*.

Les chercheurs, inspirés toujours par la nature (par exemple, certaines morphologies d'insectes), tentent d'intégrer l'aspect chimique des matériaux afin de développer la nano fabrication aux surfaces à une, deux et trois dimensions. L'optique et la photonique bénéficient de ces avancées et sont désormais des domaines d'étude scientifique importants avec un large éventail d'applications. Par conséquent, de nombreux travaux sont consacrés au développement de nouvelles techniques pratiques de fabrication d'éléments destinés à la manipulation de la lumière.

Le processus de nano fabrication permet de transformer des surfaces planes en motifs tridimensionnels à l'échelle micro ou nanométrique. Cette prouesse repose sur deux types de techniques : l'approche descendante et l'approche ascendante. Dans l'approche descendante, les nanostructures sont fabriquées à partir de matériaux en volume que l'on grave sélectivement afin d'éliminer une partie du volume, comme par exemple en lithographie. La grande majorité des techniques de nano fabrication industrielle entre dans cette catégorie. La seconde met en œuvre des techniques additives de construction contrôlées par les lois de la chimie et de la physico chimie. Cela permet de créer des édifices avec peu de contraintes d'échelle ou de résolution mais limités à des designs simples et à une homogénéité à courte distance. Dans cette thèse, nous nous sommes concentrés sur la technique de lithographie par nano impression '*Nano Imprint Lithography* (NIL)'.

L'objectif de cette thèse est d'adapter le procédé NIL aux matériaux sol-gel en combinant dépôt par voie liquide et nano impression en atmosphère contrôlée, dans le but d'imprimer directement des oxydes métalliques sur de grandes surfaces en respectant les contraintes environnementales, industrielles et économiques. Les systèmes élaborés seront ensuite exploités dans le domaine florissant de la photonique et de l'optique.

Le but de cette thèse est donc de développer des méthodes d'élaboration de métasurfaces nanostructurées à partir de la chimie sol-gel et de la Lithographie par Nano Impression (soft-NIL). Celle-ci présente notamment des intérêts d'ordres scientifiques et technologiques. En outre, elle entre dans la tendance générale du développement des processus rapide à faibles coûts utilisant des matériaux biocompatibles et non toxiques. Dans un premier temps, nous présenterons l'élaboration de nouveaux revêtements antireflets constitués de silice hydrophobe (modifiée méthyle) avec différentes

nanostructures (piliers et trous). Ces nouveaux revêtements permettent de réduire la réflexion dans un intervalle spectral large tout en conservant une large tolérance angulaire à la lumière incidente. D'autre part, ces nanomatériaux présentent une stabilité chimique, thermique et mécanique améliorée par rapport à l'état de l'art. Par la suite, un nouveau système de couche sensible composé d'une métasurface de $TiO_2$ encapsulée dans une matrice hybride microporeuse pour capteur basée sur la transduction optique, et présentant une sensibilité spectrale de 4470 nm par unité d'indice de réfraction (RIU), a été développé. Ce dernier a été exploité pour sonder la présence de COV dans l'air avec une sélectivité partielle et une sensibilité de $0.5\times10^{-3}$ R/ppm. Finalement, le savoir-faire développé a ensuite été mis à contribution pour l'élaboration de réseaux de métasurfaces par empilements successifs de matériaux diélectriques : $SiO_2$ poreux et $TiO_2$ dense nano imprimés. Ce dernier travail est précurseur à la fabrication de méta matériaux 3D par procédé sol-gel.

La thèse est divisée en quatre chapitres.

**Le Chapitre 1** est dédié à la description des progrès passés et récents des méthodes de lithographie par NIL pour (nano-) structurer des matériaux inorganiques sur une surface à partir de formulations liquides sol-gel et de suspensions colloïdales. Cette technique, d'abord inspirée des techniques d'embossage, a été développée pour la mise en forme des polymères, mais elle est aujourd'hui totalement adaptée aux matériaux inorganiques à constante diélectrique élevée, tels que les oxydes métalliques, avec d'innombrables compositions chimiques fournies par la chimie sol-gel. Par conséquent, l'approche NIL est devenue une méthode de micro fabrication polyvalente, à haut débit et très précise pour les développements en laboratoire et la mise à l'échelle et la production sur de grandes surfaces. Dans la première partie, nous décrivons l'état de l'art des méthodes de nano fabrication et la pléthore d'approches développées au cours des derniers 10 ans pour imprimer des oxydes métalliques à partir de solutions inorganiques. Dans la deuxième partie, ces approches sont discutées et comparées en termes de performances, d'inconvénients, et de facilité de mise en œuvre. La dernière partie est consacrée aux applications pertinentes dans des domaines d'intérêt. Ce chapitre présentant la compatibilité de ces techniques réside dans la flexibilité de compositions de matériaux inorganiques.

Quelle que soit la méthode de traitement choisie, l'optimisation des réplications en matériaux inorganiques par soft-NIL est une question d'adaptation de la chimie de la solution initiale "résine" et des conditions de traitement. Par exemple, l''UV-NIL' a longtemps été la méthode privilégiée, cependant, elle nécessite une chimie complexe, impliquant des photo-initiateurs coûteux et souvent toxiques. Plus récemment, le 'Thermal-NIL' couplée à un contrôle de la pression ou un contrôle environnemental de l'atmosphère a été développée, permettant l'utilisation d'une chimie plus simple. Pour les systèmes inorganiques purs, lorsque les matériaux finaux doivent être exempts de substances organiques, un traitement thermique final est très souvent nécessaire, non seulement pour décomposer les résidus organiques mais aussi pour consolider mécaniquement l'édifice par frittage visqueux et diffus. Des compromis doivent être

trouvés car ce traitement final s'accompagne d'un retrait volumique plus ou moins prononcé.

Dans les chapitres suivants, les avancées dans l'utilisation de couches minces sol-gel, combinées à la méthode T-NIL couplée au contrôle environnemental, seront explorées. Les réseaux de motifs (nano-piliers) obtenus par cette approche présenteront un potentiel applicatif pour l'optique.

**Le Chapitre 2** est dédié à l'élaboration et à la caractérisation complète de nanostructures de silice méthylée ($Si_4O_7Me_2$) nano-imprimées par sol-gel comme un couche antireflet (ARC) efficace sur substrats de verre. Les revêtements antireflets sont utilisés comme composants hautement efficaces de réduction de la réflectance pour divers équipements optiques et opto-électriques. Ces dernières années, les revêtements antireflets ont été largement améliorés grâce aux techniques de nano fabrication. Dans notre cas, l'impression a été réalisée à l'aide d'un moule en PDMS qui a été répliqué à partir d'un ARC commercial en Perfluoropolyéther (PFPE) (master) qui est systématiquement utilisé comme référence pour comparer les performances de notre ARC en silice méthylée. Nous démontrons d'abord la possibilité d'élaborer des ARCs sol-gel, composés de structures nanométriques, sur une taille record de substrat de 10 cm de diamètre (qui est la taille maximale de notre moule PDMS), confirmant l'évolutivité et la rentabilité de la méthode.

La fabrication d'ARC est critique et compétitive, en effet il y a plusieurs facteurs de critères requis pour avoir des revêtements anti-reflets parfaits tels que (i) l'élaboration de motifs nanostructurés à haut rapport d'aspect conduisant à une bande spectrale et une gamme angulaire d'efficacité les plus larges possible, (ii) une robustesse à l'abrasion, à la température et aux attaques chimiques adaptée au milieu opérationnel, et (iii) une mise en œuvre sur de grandes surfaces. Ce chapitre présente des revêtements anti-reflets sur des substrats de verre de 10 cm de diamètre, respectant chacun de ces critères. En combinant le dépôt sol-gel (ex. : *spin coating*) et NIL (contrôle environnemental thermique-NIL), des nanostructures homogènes ont été fidèlement reproduites. Ces nanostructures ont un rapport d'aspect vertical d'approximativement 1.7. De plus, le gradient d'indice de réfraction effectif transversal créé par les piliers effilés est compris entre 1.2 et 1.26. La transmission totale de réplique double face atteint 96~97% dans le domaine visible, elle est limitée par la réflexion spéculaire et surtout par la diffusion intrinsèque du substrat de verre (3%). L'effet anti-reflet est efficace jusqu'à un angle d'incidence de ~60 degrés. Nous examinons la robustesse du revêtement inorganique dans diverses conditions réalistes et extrêmes en le comparant à son homologue organique, le perfluoropolyéther (PFPE) (référence principale). Le système sol-gel montre une résistance plus marquée que le polymère de référence, surtout à l'abrasion (plus de 2 ordres de grandeur), avec moins de 20% de perte de performance anti-reflet après 2000 cycles de frottement sous une pression de ~2 $Ncm^{-2}$. Cette différence provient du module élastique du matériau sol-gel combiné à une excellente adhésion au substrat et à la conformation spécifique piliers-trous. La présence de trous permet de maintenir un profil de gradient d'indice de réfraction même après avoir arraché une partie de la population de nano-piliers. Nos résultats sont pertinents pour les applications où des

fenêtres transparentes avec une transmission large bande et grand angle sont nécessaires, comme le revêtement de verres protecteurs pour les panneaux photovoltaïques ou les caméras C-MOS.

**Le Chapitre 3** se concentre sur l'élaboration de systèmes nano composites à haute sensibilité pour la variation de l'indice de réfraction (IR) et à haute sélectivité pour la détection des composés organiques volatils (COV). La détection des composés volatiles a été un domaine de recherche important en raison des besoins spécifiques de détecteurs chimiques dans les activités industrielles et médicales. Les besoins sociaux et économiques poussent au développement de dispositifs rentables, simples et portables qui peuvent également résoudre les problèmes liés à la sélectivité chimique. Ainsi, dans ce chapitre, nous illustrons un nouveau système de nano composites combinant des matériaux sensibles diélectriques à base d'oxydes métalliques déposés par sol-gel et des structures 3D à haut indice de réfraction obtenues par NIL. La métasurface est composée de $TiO_2$ nano piliers à haut rapport d'aspect vertical ($\sim 2$). Ces systèmes présentent des résonances relativement étroites avec un grand déplacement spectral par rapport aux changements d'indice de réfraction. Elle est ensuite recouverte d'une couche microporeuse de silice hybride (H-$SiO_2$). La réflectivité de la couche a ensuite été mesurée dans le domaine visible avec une pression de vapeur d'isopropanol croissante. Ces couches hybrides présentent des différences relatives marquées en termes d'affinité chimique avec différents COV. La présence de la métasurface de $TiO_2$ améliore le signal de près d'un ordre de grandeur que nous avons attribué à l'effet d'antenne, renforçant l'interaction de l'onde électromagnétique confinée avec le milieu sensible. Ce système nano composite sol-gel présente de nombreux avantages tels qu'une élaboration facilitée des éléments, une grande stabilité chimique, mécanique et thermique, assurant leur exploitabilité pour la détection sur de longues périodes.

Les performances mesurées sont : une sensibilité (S) jusqu'à 4500 nm/RIU (0.2 nm/ppm), des changements d'intensité de réflexion jusqu'à $R^* = 17$ ($0.55\times10^{-3}$ R/ppm), FOM jusqu'à 12, avec un Q-facteur de 4 pour une longueur d'onde spécifique, ce qui est compatible avec la détection de ppm de gaz par simple réflexion spéculaire. Même si le facteur Q et le FOM étaient relativement faibles, les sensibilités étaient sensiblement plus élevées que celles rapportées pour les systèmes basés sur les plasmons de surface et celles simulées pour les métasurfaces d'oxyde métallique. Ces performances ont été comparées aux simulations basées sur les calculs de milieux de mélanges effectifs 'Bruggeman Effective Medium Approximation (BEMA)' du système, confirmant le rôle critique des antennes dans l'exaltation du signal. Les caractérisations structurelles, chimiques et spectroscopiques ont été réalisées par infrarouge à transformée de Fourier (FTIR), microscopie électronique à balayage (MEB), microscopie à force atomique (MFA), diffraction des rayons X (DRX) et ellipsomètrie (toutes sont expliquées dans annexe).

En conclusion, la combinaison d'une métasurface de $TiO_2$ et de matériaux sensibles par sol-gel offre une bonne sensibilité et une bonne sélectivité qui constituent des éléments de transduction critiques pour concevoir et élaborer un "*artificial nose*" rentable pour la détection des COV. Les performances actuelles n'ont pas été optimisées en exploitant les simulations et pourraient être améliorées en concevant une métasurface plus appropriée.

Le **chapitre 4** est consacré à la nouvelle voie d'exploration de la chimie sol-gel et de la technique NIL basée sur la fabrication d'empilements successifs des couches d'indices de réfraction alternativement élevés ($TiO_2$, n = 2.2) et faibles ($SiO_2$ poreuse n = 1.2). Ensuite, en suivant la même stratégie, nous avons pu fabriquer deux empilements verticaux de piliers de $TiO_2$ par *Nano Imprint Lithography (NIL)* et chimie sol-gel séparés par une fine couche de silice évitant le mélange de doubles empilements de nanostructures 3D, nous avons évalué les réponses optiques par spectroscopique visible. La présence de l'alternance d'empilements successifs des couches à faible et à fort d'indice de réfraction incorporées avec un double empilement 3D de réseaux de nanostructures de $TiO_2$ (effet de Moiré) améliore la résonance et l'interférence lumineuse, en comparaison avec un empilement 2D de couche mince ou même avec la seule réplique de nanostructure de $TiO_2$ recouverte d'un film mince.

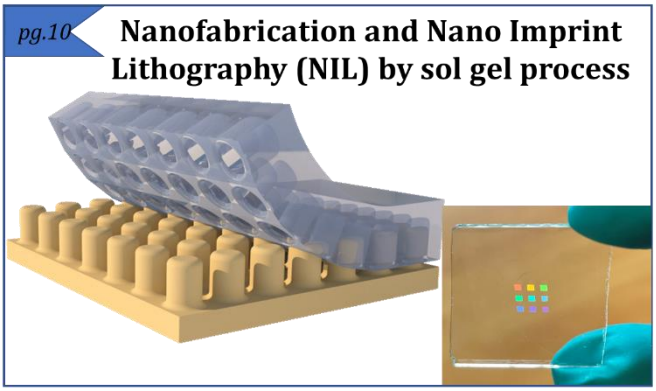
Ce travail n'est pas encore terminé, les résultats et observations sont au stade initial. Il est donc nécessaire d'approfondir les recherches pour bien explorer son potentiel en termes de performances, et les applications optiques potentielles.

Il faut considérer qu'il existe plusieurs paramètres critiques pour l'optimisation de ce système, à savoir :

1- Le contrôle de l'épaisseur des couches minces déposées.
2- Le nombre d'empilement successifs.
3- La forme de la géométrie du pilier nanostructure (rapport d'aspect et morphologies).
4- Les couches résiduelles exemptes de réseaux de nanostructures.

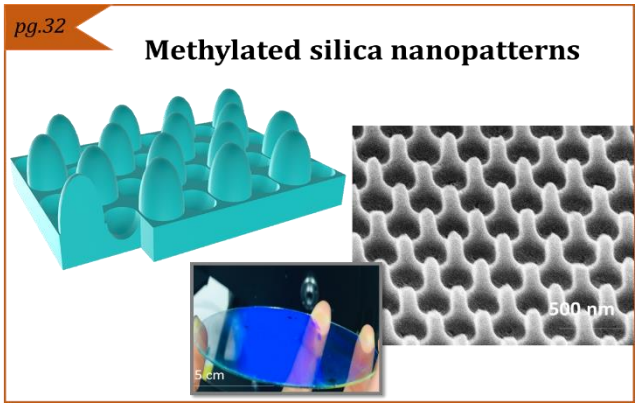
**Pour conclure**, cette thèse décrit la fabrication de réseaux de motifs (nanostructures) de silice hybride, de $TiO_2$ à haut rapport d'aspect et leur combinaison en structures 3D superposés dans un système d'empilement successifs. Elle montre ainsi la flexibilité du couplage chimie sol-gel / nano impression pour l'élaboration d'architectures 2D et 3D complexes sur de grande surfaces et à faibles coûts. Plus important, elle permet de s'affranchir de l'utilisation de résines commerciales couteuses et toxiques, dont les propriétés physiques restent limitées. En effet, la très grande versatilité de compositions chimiques accessibles par sol-gel apporte une dimension supplémentaire à ce mode de fabrication rendant ainsi possible la structuration directe de céramiques dont les propriétés optiques (n, k, émissivité), électrique (conductivité, piézoélectricité), mécanique (dureté), chimiques (surface, surface spécifiques associées à la porosité) peuvent être choisi parmi la très grande famille des matériaux inorganiques.

# *Graphic Table of Content*



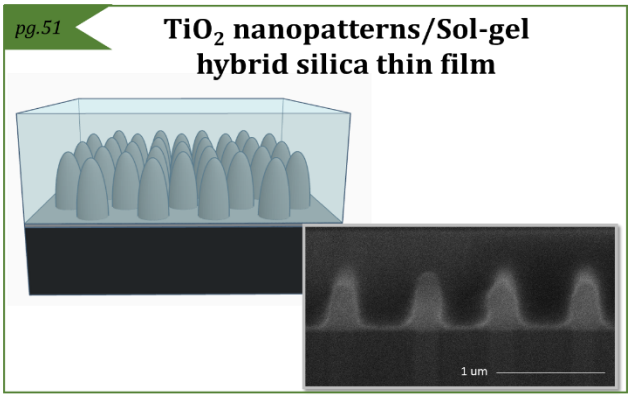

## ***Chapter 1***

State of the art



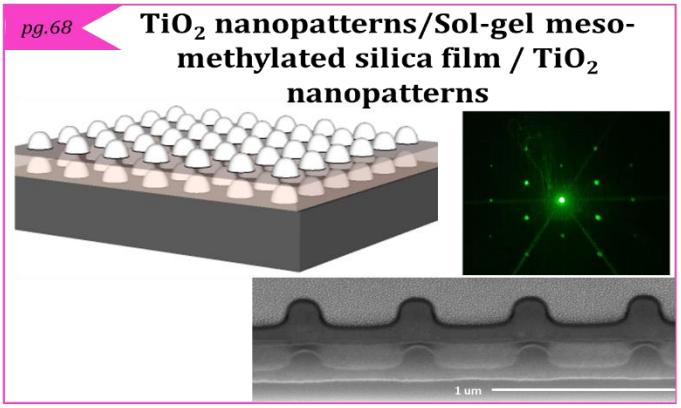

## ***Chapter 2***

Nanostructure
Anti-Reflection coating




## ***Chapter 3***

High sensitivity gas sensor for refractive index (RI) variations




## ***Chapter 4***

3D imposed multi-stack of moiré patterns

# CHAPTER 1: NANO-IMPRINT LITHOGRAPHY PROCESSING OF INORGANIC-BASED MATERIALS

In this chapter a review of the past and recent progress of Nano-Imprint Lithography (NIL) methods to (nano-) structure inorganic materials from sol-gel liquid formulations and colloidal suspensions onto a surface is provided. This technique, first inspired by embossing techniques, was developed for soft polymer processing, as final or intermediate materials, but is today fully adapted to hard inorganic materials with high dielectric constant, such as metal oxides, with countless chemical compositions provided by the sol-gel chemistry. Consequently, NIL has become a versatile, high throughput and highly precise microfabrication method that is mature for lab developments and scaling up. In the first part, we describe the state-of-the art in nanofabrication methods and the plethora of approaches developed in the last decades to imprint metal oxides from inorganic solutions. In the second part, these are discussed and compared in terms of performances, issues, and ease of implementation between several recent studies. The final part is devoted to relevant applications in domains of interest.

# 1. Generalities

## 1.1. Nanofabrication techniques and Nano Imprint Lithography (NIL)

From the early ages, technics to cut, sculpt, etch, mold, assemble pieces of matter have been developed and constantly optimized to satisfy the growing demand for functional materials. Since the inception of nanotechnology, these operations have to be mastered at the nanoscale. For these tasks, many top-down and bottom-up methods exist. However, they do not simultaneously fulfill all the necessary criteria of performance such as spatial resolution, pattern complexity, hierarchy, scalability, dimensionality, cost-effectiveness, a span of processable materials. Thus, motivations to optimize them and develop new ones persist as a flourishing domain of research and development.

Many materials exhibiting various intrinsic properties (mechanical, chemical, electrical, optical, thermal, *etc*.) are exploited in numberless functions once nanostructured onto a surface. Amongst them, metal oxides are extremely valuable for their extreme chemical, mechanical, and thermal stability and range of physical-chemical properties. Thanks to its hardness, chemical inertness, transparency, and low background fluorescence, glass is one of the preferred choices for micro-and nano-fluidics device fabrication. In photonics, metasurfaces require optical properties that are found in dielectrics such as $SiO_2$ often combined with high refractive index dielectric $TiO_2$ or (plasmonic) gold[1]. For nano-electronics, silica remains one of the key dielectric materials. Micro-mechanical scaffolds or persistent data storage systems need extremely stable materials such as $TiO_2$[2].

For planar nanofabrication, either bottom-up (self-assembly) or top-down (lithography, etching) methods exist. First, bottom-up nano-structuration approaches based on micellar block copolymers self-assembly have shown great successes during the last decade[3]. When combined with sol-gel chemistry and liquid deposition processes, periodically organized mesoporous inorganic and hybrid thin films were obtained through the so-called micellar templating method[4] or Evaporation-Induced Self-Assembly (EISA)[5] (see Appendix 1). A large variety of templating agents can be coupled with inorganic polymerization reactions for the design of periodically organized nanostructured hybrid phases. Careful control over the physical-chemical parameters leads to the elaboration of metal-oxide nanopatterns[6],[7]. A plethora of combinations have been reported in the past 20 years and are available in many metal-oxides with different structures such as lamellar, 2D hexagonal, or 3D (fcc, bcc, gyroid, grid-like, worm-like, *etc*.). Achievable periods and/or feature dimensions ranging from several nanometers to several tens of nanometers. However, the patterns adopt a periodical arrangement and exhibit many defects, no spatial control (position and direction), and poor long-range ordering limiting their applications.

Amongst the top technological achievements of the last century in nanofabrication, photon-assisted processing methods are with no doubt the more technologically advanced ones. Photolithography combined with a dry or wet etching of the hard metal oxides is today available with acceptable performances in terms of quality, versatility, resolution, throughput, cost, and achievable morphologies[8–11]. Still, these methods remain cumbersome and are constrained by a limited choice of required photosensitive selective masks containing complex organic radical or cationic non-linear absorbers (photo-initiators) which are expensive, often colored, poorly soluble in photopolymers, and could be toxic[12]. Photolithography faces an intrinsic critical limitation in resolution dictated by the wavelength of incident writing light waves. High-energy ultraviolet radiation (deep-UV) is used nowadays in production lines to elaborate features smaller than 40 nm[13]. For this kind of lithographic method, hard-masks are needed for replication. They are generally fabricated using Electron Beam Lithography (EBL) in photosensitive materials[14]. Another top-down approach is direct writing with a focused ions beam (FIB)[15] where accelerated ions sputter locally on the surface of the target material. These two methods provide a high lateral resolution but they are time-consuming, hardly-scalable rendering them cost-effective only for the elaboration of masters and masks.

Subtractive techniques involving laser/material interactions sharing similar non-linear optical effects but at much higher powers, are also available and are used to etch dense metal oxide surfaces. For such inorganic materials, these effects are initiated by multiphoton absorption and tunneling ionization, promoting electrons to the conduction band. It is then followed by an avalanche ionization when a certain degree of ionization is reached. At such a high ionization density, the free-electron plasma absorbs the laser radiation and transfers the energy to the lattice by non-radiative relaxation, inducing non-reversible breakdowns in the material. This approach has the advantage of ablating hard transparent materials such as glass at the nanoscale[16]. Advanced laser technologies, such as ultrafast Bessel beams, have also been used to attain processing accuracy beyond the diffraction limit, well into the nanoscale domain[17]. In both examples, the high anisotropy of the channel (depth-to-width) is due to the typical anisotropy of the voxel beam and leads to poor axial resolution with respect to the lateral one. Indeed, diffraction and nonlinear self-focusing effects result in a non-punctual focalization, limiting the process to anisotropic motifs. This may be improved by shaping the beam, which remains a complex task to achieve[18].

Moreover, soft lithography (as a non-photolithographic strategy) has been extensively developed since the 19$^{th}$ [19]. Soft lithography englobes different techniques depending on the mold used in a stamping process or filled as a template. Nano Imprint Lithography (NIL) is one of the soft lithography methods, applicable to a large number of materials, appealing thanks to its high performance associated with ease of implementation. The first work on NIL was developed by Stephen Chou and coworkers in the 1990s when its team reported 20 nm patterns, initially etched in a silicon mold, transferred in a polymeric resist[20],[21]. This experiment was performed by strongly pressing the mold (P=50-100 bars) while heating at 100 °C to deform and shape the thermoplastic polymer. This study opened the way to soft NIL at the sub-100 nm scale. Imprinting of sol-gel resists was first

demonstrated by Lukosz and coworkers in the 1980s at high pressure (P=280-500 bars) through hot embossing[22]. Even if the pressure used to imprint the sol-gel resist was rapidly reduced, it represented one of the major drawbacks of this technique. Indeed, silicon substrates used in microelectronics can easily break if the applied pressure is not perfectly homogeneous over the wafer surface. The use of hard and brittle molds (mostly silicon or fused silica) presented several downsides: (*i*) resist often sticks to the mold surface due to its high surface energy (*ii*) long range deformation can easily break the mold (*iii*) solvent and air bubbles cannot escape once trapped under the mold (*iv*) rigid molds cannot accommodate any curvature or defects. Due to all those limitations, costly hard molds could be used only a very limited number of times. The emergence of soft-NIL (Figure 1-1), by Whitesides and coworkers, tackled all those problems by the introduction of polydimethylsiloxane (PDMS) elastomeric molds[19]. Soft molds have low surface energy ($\Upsilon^{PDMS}$= 21 mJ.m$^{-2}$ compared to $\Upsilon^{Si}$= 52 mJ.m$^{-2}$), are permeable to solvent vapors, and can deform to follow the features of the substrate. PDMS is less expensive with respect to hard molds and can be used dozen times. Soft-NIL allowed to drastically reduce the pressure (P < 5 bars) and temperature applied to emboss the resist layer. With the huge improvements made in the past decades, Soft-NIL is currently performed at ambient pressure and room temperature and is now reaching sub-10 nm resolution[21] on sol-gel resists when performed with optimized PDMS molds.

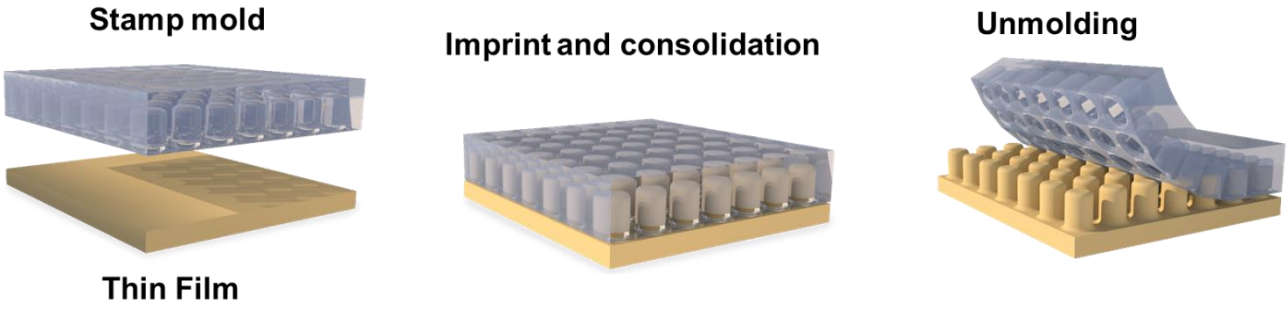
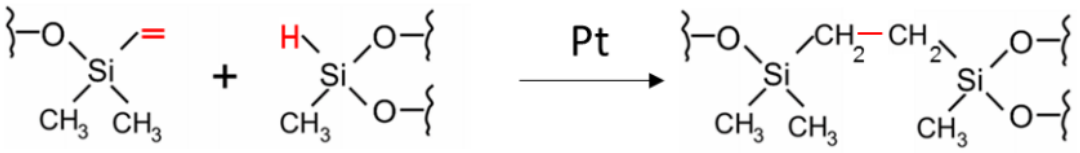



Figure 1-1. Schematic illustration of soft-NIL processing

PDMS stamps are generally fabricated from an initial master as a mold, stamp, or template. From a single master, generally made by an expensive and low throughput technique - such as EBL, FIB, or laser ablation on a silicon wafer - it is possible to easily fabricate many inexpensive PDMS molds bearing the same features. The fabrication of the molds is performed by using a prepolymer - generally composed of vinyl functionalized linear di-methyl-siloxane and a silicon-hydride functionalized linear di-methyl-siloxane – mixed with a catalyst – generally a platinum compound - and poured onto a prepared master as a pre-patterned surface. The cross-linking reaction, called hydrosilylation, is catalyzed by platinum and involves the addition of Si-H bonds across unsaturated bonds.




The transition of the prepolymer from a viscous liquid to a solid elastomer takes usually several hours at room temperature. It is generally accelerated by heating at a mild temperature for instance 70 °C. The hydrolyzation cross-linking route is generally preferred as no by-products are formed and it offers a comfortable time working window before extended cross-linking occurs [23,24]. Once fully cross-linked, the resulting mold is easily demolded from the master thanks to its elasticity (Figure 1-2). The mold perfectly replicates the initial master features (relative shrinkage between master and mold can be neglected). Many molds can be fabricated from a single master. However, with extensive use, defects will start to appear on the master owing to the local adhesion of PDMS during mold release. For this reason, the surface of the master (for instance often made of silicon) is functionalized (*e.g.* with fluoroalkyl silanes) to decrease the surface energy, reducing the interactions with the PDMS chains.

When patterns with features smaller than 100 nm are needed, the excessive softness of PDMS can induce deformations of the mold shape while printing. This phenomenon has been widely studied both theoretically and experimentally[25,26]. As first demonstrated by Delamarche and coworkers[25] only a fraction of the structures accessible by nanofabrication in hard materials will give stable structures in PDMS stamps. If the aspect ratio (AR = height/width) of the motifs is too low, insufficient relief exists on the surface of the stamp to withstand the compressive forces due to the adhesion between stamp and substrate. Thus, no patterns are achievable. Moreover, if the AR is too high, structures can collapse under their weight[25],[26]. High AR feature causes loss of structural integrity of the feature in a mold. During the stamping process, capillary forces can be strong enough to deform the stamp features and contact two neighboring structures. This is the case for densely packed structures, long grating lines, or tightly spaced pillars. These structures are prone to pairing due to their high surface-to-volume ratio. Once collapsed it is hard to restore the PDMS features. Different ways of restoring the structures have been explored such as washing with low surface tension solvents or with water-containing surfactants but with little success[25],[27]. The easiest way to prevent the deformation of small patterns is to increase the rigidity of the PDMS material. Such PDMS, called hard-PDMS (h-PDMS), has been firstly developed by Schmid and coworkers, in 2000[28]. Hard-PDMS uses branched siloxanes, shorter cross-linkers, and a higher concentration of reactive groups compared to standard PDMS to increase the cross-linking density and the rigidity between the cross-linking points. The different concentrations in reactants and their ratios have been extensively studied[27] and commercial products are now available. PDMS hardness is estimated through its Young's modulus that is about 20-30 MPa for conventional PDMS whereas it goes to 60 to 70 MPa for h-PDMS. Other materials than PDMS can be used, such as siloxane-composites[29] or thermo-plastic polymers[30]. However, they miss the intrinsic advantages of PDMS. Similarly, using pure h-PDMS has its limitations: (*i*) a high-modulus polymer can increase

the stress during the curing step, (*ii*) difficult rendering to separate it from the master, (*iii*) h-PDMS has low flexibility, (*iv*) making conformal contact on rough surfaces rather difficult. The increased rigidity leads also to a poor accommodation to inhomogeneous stress during imprinting that might lead to plastic deformation or cracking of the stamp or of the substrate. In order to increase the rigidity and, at the same time, keep the advantages of low-modulus PDMS, hybrid stamps have been developed with a thin h-PDMS layer of few microns that contains the patterns and a thick layer of standard PDMS of about 0.5 mm (Figure 1-2). In addition, to minimize in-plane deformation, for easier handling and automatization, this assembly (standard PDMS + hard PDMS) can then be backed by a thin glass plate.

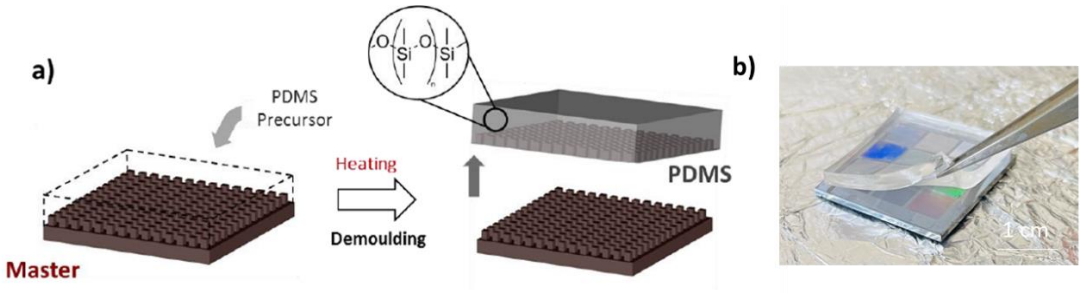



Figure 1-2. a) Schematic representation of the mold preparation. The precursor is poured onto the hydrophobized surface of the master and cured before demolding. b) Picture of a silicon master and its negative replica into a flexible mold.

Applying soft-NIL processes to directly imprint sol-gel metal oxides is highly interesting. However, it is quasi-unachievable due to two limitations: the impossibility to deform a brittle ceramic film and the difficulty to reach a plastic state at moderate temperature. A promising soft-NIL method on metal oxides exploits as-deposited sol-gel layers (xerogels). Xerogels are poorly cross-linked networks of sol-gel, organometallic precursors, or hydrolyzed intermediates. Such gels remain flexible and will stiffen from advancing polycondensation during drying and aging of the films and finally with thermal annealing to form the metal oxides[7,31,32]. The properties of xerogels can be exploited in soft-NIL at two conditions: (*i*) that imprinting takes place when the layer is in a gel-like phase and (*ii*) the demolding is made after sufficient solidification. Both these controls are challenging in sol-gel since the as-deposited layers undergo more or less fast cross-linking upon drying and mild thermal activation. These phenomena are generally accompanied by the release of water or solvent molecules that are trapped within the materials underneath the mold, affecting the replica morphology, density, and shrinkage factor. Eventually, the demolded material is converted into a purely inorganic and rigid metal oxide after calcination.

Sol-gel approaches rely on the use of polymeric or organic stabilizing agents in order to adjust the rheology, the precursor reactivity and achieve a good resolution and a large geometrical aspect ratio of the final printed 3D structures. The main drawback associated with this approach is the severe shrinkage following the evaporation of organic moieties during the annealing step (up to 60-80% vol)[33–36]. Sol-gel formulations containing metal

oxide nanoparticles (NPs) can be directly imprinted resulting in a reduced shrinkage[36] and materials having lower density (resulting from the presence of pores associated with the NP packing). A compromise thus needs to be found between lower shrinkage and denser material. Of course, stabilizing-agent-free xerogels can be used allowing for a reduced shrinkage factor. However, the very high viscosity of the intermediate xerogel will prevent efficient mass transfer within the sharp features of the mold.

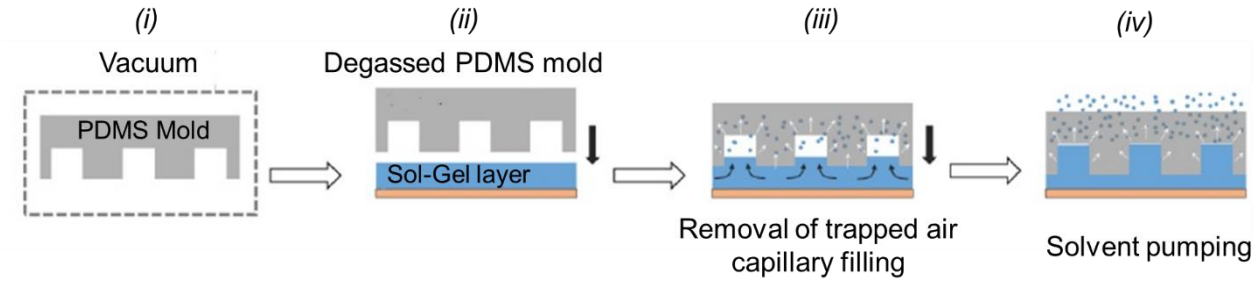



Figure 1-3. Scheme presenting the Degassed Assisted Patterning (DAP) process applied to the nano impression of sol-gel layers[61].

To promote the filling of the mold features, a technique called Degassed Assisted Patterning (DAP), taking advantage of the properties of PDMS to enhance its permittivity towards solvents has been developed. Historically, Degassed Assisted Patterning was used in microfluidics as a pump-free manipulation. First reported by Hosokawa and coworkers in 2004[37], it allowed to pre-store the pumping energy in the degassed PDMS in order to obtain a liquid flow in the PDMS channels during the experiment without the use of external pumping. Indeed, the solubility of a gas in PDMS follows Henry's law: the concentration of gas dissolved is proportional to the partial pressure of the gas around the mold.

When a PDMS is degassed and brought back to the atmosphere, it equilibrates by absorbing air[38]. Therefore, by using degassed PDMS molds, a better filling of the cavities can be achieved. The patterning process can thus be broken down into four steps (Figure 1-3): (*i*) the mold is first pumped under vacuum (P < 10 mbars) for a few minutes; (*ii*) straight after breaking the vacuum, the mold is deposited on as-prepared xerogels; (*iii*) Air trapped in the mold cavities is easily pumped through the mold, promoting the filling of the cavities; (*iv*) Solvents, generally trapped within the material underneath the mold, are pumped out improving the filling of the PDMS pattern cavities. To complete the imprinting step, consolidation of the xerogel is achieved through UV or thermal curing before demolding. Final thermal treatment is often required to achieve the pure metal oxide material.

# 2. Nano Imprint Lithography (NIL) Methods

## 2.1. UV-NIL

UV-NIL method is one of the most developed and used in recent years. From its outset till today, it has been adapted to a plethora of different materials, including organic, hybrid organic/inorganic[34,39–41], and inorganic metals and metal oxide materials from sol-gel solutions and/or nanoparticles (NPs) dispersions[42–46]. A prerequisite is that the imprinted materials (precursors) need to absorb UV radiation. UV-NIL processes involve several steps, starting first with liquid deposition (*e.g.* spin, dip, ink, spray, *etc*.) of the "resin" solution, followed by imprinting with a UV resistant and transparent mold stamp, composed of typically Polydimethylsiloxane (PDMS), poly-urethane-acrylate (PAU)[34], Quartz, or Perfluoropolyether (PFPE), so that curing through UV exposure takes place directly underneath the mold. Once the material is cross-linked enough, the mold is delicately peeled off to prevent damaging the replica. UV-NIL enables working at room temperature with low or no external pressure. UV-NIL has been used to replicate the patterns hybrid resins ($TiO_2$-$SiO_2$-PMMA) with relatively good aspect ratio patterns (AR = 1.2)[39]. Besides, using photosensitive titanium demonstrated the no-need photo-initiator in the solution, since the cross-section of Ti centers was sufficient to trigger the cross liking of the network. Patterns were thus obtained faithfully from PDMS and PUA mold[34]. Furthermore, using organic resins for a large proportion of the material composed of ZnO induced the role of UV-Binder for the UV-NIL method[40,41].

UV-NIL often does not require any temperature cycling and leads to relatively high throughput on substrates compatible with UV curing. In addition, UV-NIL has been demonstrated to be a high-volume and cost-effective patterning technique, able to achieve sub-10 nm resolution.

Step-and-Flash Imprint Lithography (S-FIL)[42],[43] is another way to replicate patterns from the mold by UV-NIL to prepare organic polymer patterns. Contrary to common UV-NIL, S-FIL relies on photopolymerization chemistry of low viscosity resins, enabling to fill the mold cavities by the capillary forces with low mechanical pressure at room temperature. This S-FIL UV-NIL method was exploited by Ganesam and coworkers in 2012[42] to elaborate $TiO_2$ nanostructures. The imprinted patterns were heat-treated finally at 450 °C for 1 h in the air to remove the organics and convert the inorganic parts into Anatase. The decomposition and the thermal treatments induce high shrinkage due to the high proportion of organic stabilizers and fluidizers required in this process.

Therefore, the impact of chemical formulation on the shrinkage and crack formation during densification of the replica through UV-NIL was determined in 2014[47]. Three formulations (spherical, branched and pure binder) were studied by mixing the two sol-gel sources of $SiO_2$ in different proportions. After curing the pattern by UV irradiation for 60 seconds under the PDMS mold, thermal annealing was applied between 200 and 500 °C for 1 h. When the annealing temperature increases from 200 to 500 °C, features lose

64% in volume, which can be considerably reduced when using high concentrations of dense silica sources. Besides, less shrinkage is accompanied by fewer cracks, suggesting that the presence of NPs allowed for better stress relaxation during densification.

Whatever the imprinting method, one has to find a compromise between allowing a faithful infiltration of the mold cavities with a fluid enough resin and with minimal deformation, while preventing as much as possible the shrinkage upon consolidation of the hard-inorganic final patterns. Organic fluidizers and binders are generally used to facilitate the replication, a minimal proportion of them is required to reduce as much as possible the related shrinkage. Lower shrinkage is obtained when solid inorganic nano-building blocks are used since they require fewer binders and fluidizers for the process as a result of their lower surface interacting with the medium. The issue of using these NPs lays in the need for longer treatment for consolidation, the creation of residual inter-particle porosity, and the formation of a rough surface associated with the size of the particles[47].

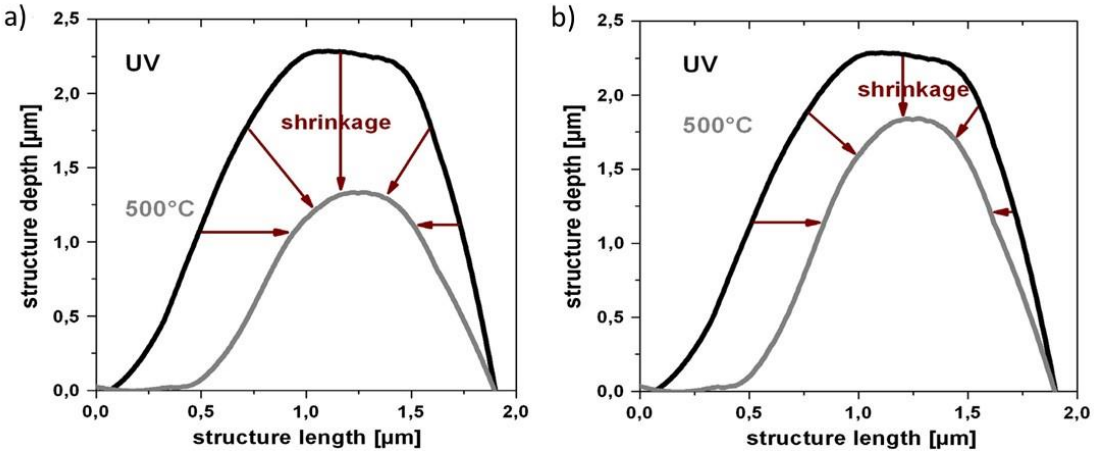



Figure 1-4. AFM profiles of 2-µm nanostructured film after thermal treatment, respective solutions were prepared with pure binder system (a) and a sol–gel matrix incorporating 40 wt% branched $SiO_2$ particle content (b). Thermal curing was carried out at 500 °C/h[47].

## 2.2. Thermal NIL

The thermal NIL (also known as hot embossing) process is the earliest type of NIL introduced by S.Y. Chou[20]. T-NIL is one of the most attractive NIL techniques due to its simplicity and capability to replicate nanostructures into various types of materials onto various thermally resistant substrates. Mold stamps can be PDMS, Nikel, Quartz, PFPE, PUA, *etc*. In typical T-NIL processes, a stamp mold is brought in contact with the resin, the whole system is heated up either to soften a thermoplastic resin (that will regain its rigidity after cooling) or to crosslink a thermally curable fluidic resin. T-NIL is categorized into three different methods: Pressure thermal NIL, Direct thermal NIL, and

environmental control thermal NIL. They differ by the underlying phenomena used to fill up the mold cavities.

In Pressure T-NIL, a slight mechanical pressure helps the viscous resin to infiltrate the mold. Inorganic metal oxides, hybrid organic/inorganic resins, and dispersed nanoparticles[50] replicated patterns were approached by the pressure T-NIL. Transfer patterning of inorganic materials was reported by Kang and coworkers in 2008[51]. They deposited by electron beam evaporation a 40 nm thick layer of metals on a patterned PDMS pressed (< 40 kPa) and thermally cross-linked at 80 °C to deposit electrode wires. More recently, $TiO_2$ Mie resonators on Si and glass substrates from a colloidal dispersion of anatase and rutile $TiO_2$ NPs[52] are obtained with slight pressure and crosslinked at 100 °C[53]. Moreover, the T-NIL process has been studied lately, with different metal oxides ($Al_2O_3$, $Ga_2O_3$, $In_2O_3$, $Y_2O_3$, $B_2O_3$, $TiO_2$, $SnO_2$, $ZrO_2$, $GeO_2$, $HfO_2$, $Nb_2O_5$, $Ta_2O_5$, $V_2O_5$, and $WO_2$) from hybrid formulations[43][54]. In this method, PDMS mold was brought in contact with film metal oxide under 30 bar and at 110 °C to 130 °C for 15 min. After demolding, patterns were annealed between 300 and 475 °C for 1-2 h. As expected, more or less high shrinkage accompanies the final annealing for each metal oxide. The reason for this variation of the shrinkage is likely attributed to the difference in organic content used for each metal oxide. Latterly, replication of materials such as ZnO[54] on large surfaces was demonstrated the relatively high throughput and faithfully results, using sol-gel via pressure T-NIL. Additionally, replication of the 3D patterns can be conceived by two steps of hot embossing. Hence, in order to obtain higher aspect ratio patterns, two steps rotational method by pressure T-NIL is demonstrated[33],[55]. In this method, the PDMS stamp was brought into contact with film and both were heated at 110 °C for 240 s under < 0.2 MPa pressure then PDMS was demolded and rotated at 90° for the second imprinting to take place in the same conditions. Finally, the sample was annealed at 550 °C for 15 min to yield amorphous $SiO_2$. The squares patterns were gained at a high aspect ratio around 5[33],[55].

Another method in T-NIL is direct T-NIL, which was developed after pressure T-NIL. The development of this technique in comparison with Pressure T-NIL is just the question of the stamp-filled cavity. In pressure T-NIL, the presence of slight pressure led the mold cavities to be filled easily and get into contact with the thin film. Whereas, in direct T-NIL, degassed molds are used. The pumping helps mold cavities to be filled (as mentioned in the Generalities, Figure 1-3) which technically replaces the extra pressure. Hence, developing the direct T-NIL was carried on by demonstrating the possibility to imprint a sol-gel solution such as zirconate titanate[56], $TiO_2$ sol-gel, and $TiO_2$ nanoparticles[36]. The method was improved by optimization the time and temperature during NIL. Therefore, $TiO_2$/NPs replicated patterns with AR = 1 obtained at 120 °C for 15s demonstrated as a convenient and time-consuming sol-gel mingled with direct T-NIL[36].

The third method of thermal NIL, environmental control T-NIL, is based on adjusting the vapor pressure of the solvent (mainly water or ethanol) in the chamber to stabilize the resin content in a solvent at a given value defined by adsorption/desorption equilibrium, altering then, the viscosity for infiltration. This latter method can be used in combination with pumping. An alternative approach to pressing the mold on the resin soft layer to trigger cavity infiltration is to maintain the resin as liquid as possible with a

volatile compound (the solvent phase) and pump it through the mold. Being the PDMS molds slightly microporous, a pre-degassing of the latter before the application is sufficient to allow this pumping (as mentioned in the Generalities part). Using a volatile solvent compound as a fluidizer requires preventing total evaporation from the resin by setting a proper environmental control in the NIL chamber before applying the degassed mold. Dalstein and coworkers[57] used such degassed PDMS molds to imprint $TiO_2$ from a simple sol-gel. After deposition of the sol-gel layer on Si or glass substrates, the degassed mold was gently applied on it and maintained at 110 °C for 5 min before demolding. Annealing at 450 °C for 5 min ensures the complete densification and crystallization of $TiO_2$ into anatase[57]. The 100 nm patterns had an aspect ratio of ~ 1[57], however, deposition of a too thick initial layer led to the presence of a 200 nm-thick residual layer. Later on, employing this method patterned surfaces for controlled wetting[58] and 250 nm $TiO_2$ dielectric Mie resonator pillar arrays (aspect ratio ~ 1)[59] were elaborated with a residual layer as thin as ~ 10 nm by applying a thinner initial sol-gel layer (see Figure 1-5).

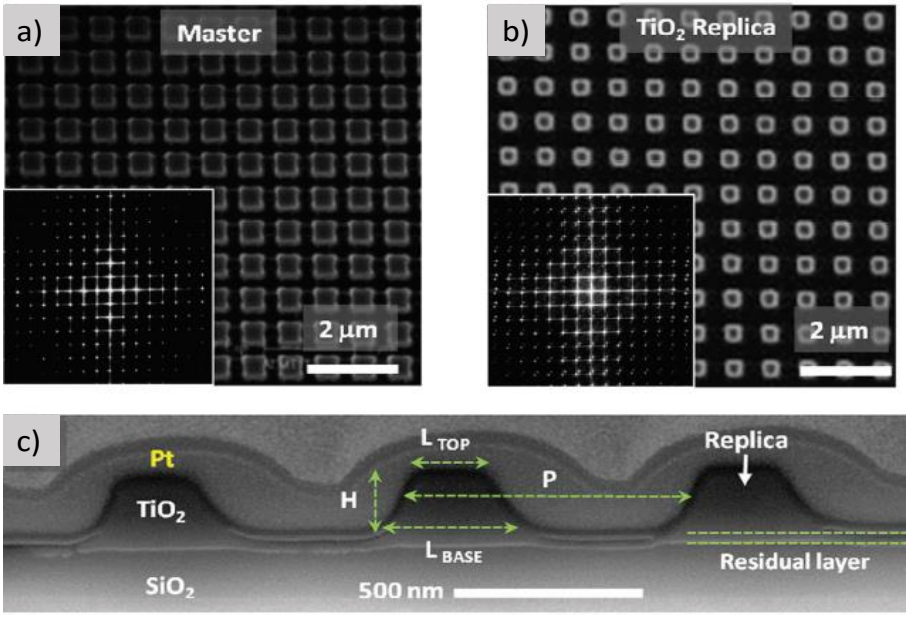



Figure 1-5. SEM image of a) Master, b) Replicated $TiO_2$, c) Cross-section nanopatterns $TiO_2$ indication the thin residual layer[58].

The imprinting was performed in a clean room, where temperature and humidity were kept constant. Imprinting outside the clean room was accompanied by a loss of reproducibility attributed to changes in the atmospheric humidity. A full study of the influence of humidity on replication quality was then performed with various metal oxides from metal chlorine, water-ethanol solutions by Bottein and coworkers[60] for the first time. The faithfulness of the replication of sol-gel systems ($TiO_2$, mesoporous $SiO_2$, Methyl-$SiO_2$, $Al_2O_3$, and Y-$ZrO_2$) can be optimized by simply adjusting relative humidity within a specific span during the NIL process that depends on the external temperature. Straight after deposition by dip-coating, the sol-gel layers were imprinted with a degassed PDMS mold at 22 °C in different relative humidity ranging from 20 to 85% depending on

the film mobility (*e.g.* $SiO_2$ for 70% and $TiO_2$ for 50% at 22 °C)[60]. Then, the sample is consolidated for 5 min at 120 °C and final annealing at 450 °C for 10 min after demolding. Figure 1-5 shows that for the $TiO_2$ system, a low humidity led to no, or low aspect-ratio, replicas, while at high humidity a dramatic loss of homogeneity is obtained. The best replication (homogeneous and high aspect ratio) was achieved with ~ 50% RH at 22 °C for $TiO_2$. Other systems did not show the same dependency and a systematic investigation of the quantity of water up-taken into the as-prepared sol-gel initial layers with respect to RH was undertaken by environmental ellipsometry (see Figure 1-6). The deduction was that even if the optimal RH is different for each metal oxide system, the optimal water content of 30% volume in the films is common to all the cases, which is related to the difference in hygroscopic property of the as-prepared films. Furthermore, in absence of a stabilizer, the sol-gel tends to spontaneously cross-link with time, which needs to be taken into account[60].

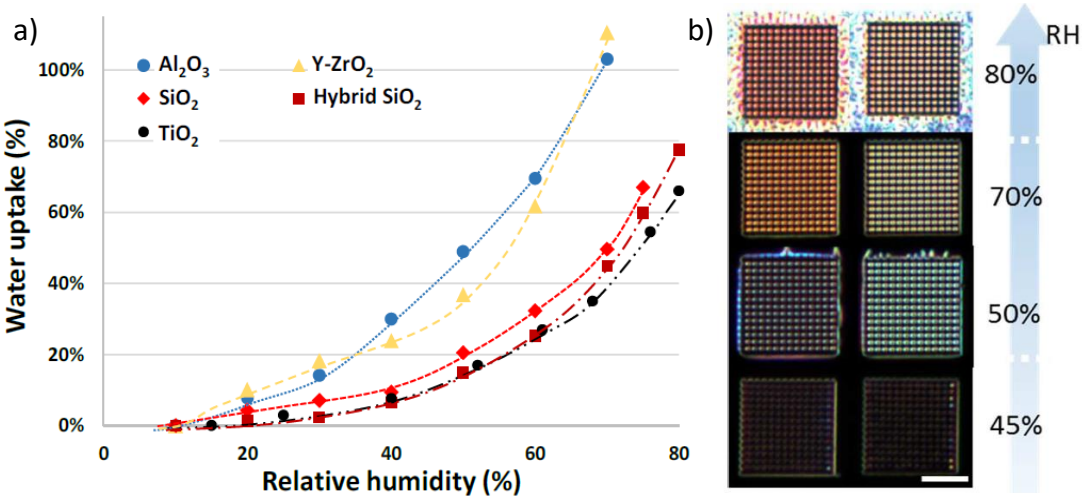



Figure 1-6. (a) Water uptake of various as-prepared xerogels concerning relative humidity measured by *in situ* time-resolved Ellipsometry. (b) Optical microscopy dark-field images of $TiO_2$ replicas imprinted at 45%, 50%, 70%, and 80% RH, replicated[61].

Relative humidity during NIL determines the optimal replication and ideal morphology of the nanopatterns, regarding xerogel viscosity. Figure 1-7 illustrates the ideal replication region for $TiO_2$ nanopatterns[60].

Environmental control T-NIL was then exploited by Naffouti and coworkers[61] and Checcucci and coworkers[62] in 2019 to prepare high aspect ratio pillar arrays as optical metasurfaces. They implemented the fabrication over a large area of arrays of titania-based Mie resonators with high throughput and at low-temperature providing structural colors (*e.g.* for displays), dynamic and reversible color change, and refractive index sensing[62].

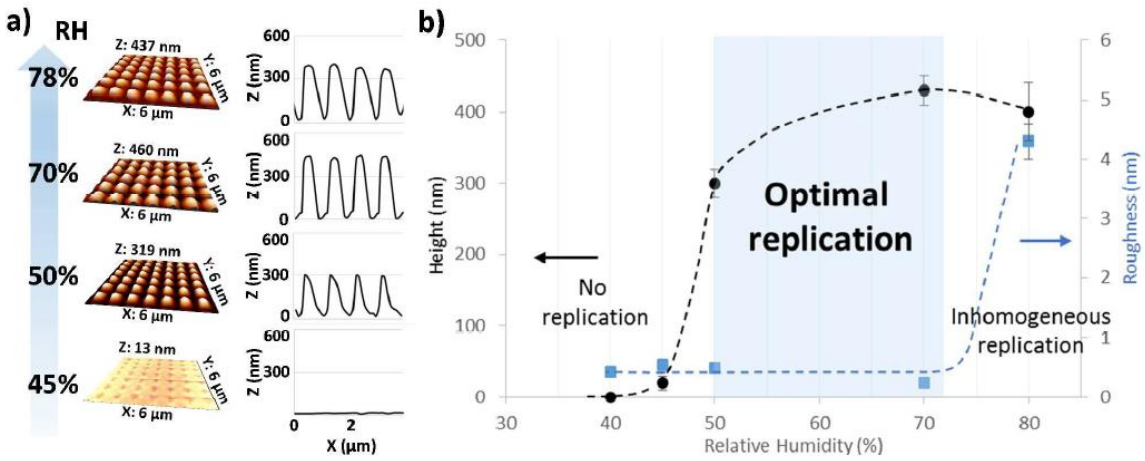



Figure 1-7. a) AFM maps and profiles of the square arrays imprinted at various humidity. b) Patterns's heigth and roughness after thermal curing as a function of humidity[61].

In this thesis, the replication of nanostructure patterns was accomplished via sol-gel environmental control T-NIL. Moreover, establishing some other NIL methods (such as Pressure T-NIL) is exhibited due to the enhancement of the aspect ratio and replication optimization, which will be described in upcoming chapters.

## 2.3. Direct printing

Printing by soft-NIL without UV and thermal, induced cross-linking cannot be performed with any systems. Sol-gel silica is however well adapted as its condensation rate is relatively slow when in solution but can become extremely fast upon evaporation of the solvent owing to the spatial gathering of the silica moieties. Therefore, one needs to make sure that the sol-gel initial layer is soft enough for the impregnation in the mold and cross-link after infiltration whatever the time needed to maintain the structure when demolding. In 2011, A. Polman's group[48] used simple silica sol-gel formulations, that they deposited and imprinted directly with PDMS stamps. Demolding was possible after 20 min without heat to yield 400 nm square arrays after further annealing at 200 °C (shrinkage 18%). The presence of a methyl group on the silica precursor is crucial to slow down the condensation and enable infiltration. In 2017, Shin and coworkers[49] prepared piezoelectric nano-generators via imprinting sol-gel Fe doped $BaTiO_3$ nano-pillars. The $BaTiO_3$ sol-gel layer was then poured on the pre-cleaned Indium Tin Oxide (ITO) surface, followed by covering with a PDMS mold with a nanohole array.

# 3. Applications

Thanks to its versatility in framing different materials in a wide range of 3D structures size and shape on arbitrary substrates (*e.g.* glass, semiconductor, metal, plastic) NIL has been efficiently exploited for a plethora of various applications such as photonic crystals[39,63], LEDs[40], solar cells[48,64,65], sensors[57], anti-reflection coatings[59,66,67], and biomedical[68]. During the years, refinement in NIL techniques induced major contributions with various fields of application based on the indicated materials and techniques. For instance, applying lithography approaches to metal oxides is highly attractive since robust and thermally stable patterned surfaces with adjusted mechanical, chemical, and optical properties can be directly produced. Thus, patterning of sol-gel materials was quickly developed to replace polymeric resist in many applications requiring patterned inorganic oxides such as microelectronics or optics. Most of the sol-gel resists used industrially are still inorganic-organic hybrids due to easier processing and compatibility with existent lithography processes developed for polymeric resists. Here, some of the recent research works are addressed to exhibit the dispensed exploitation in applications and industries by NIL techniques.

## 3.1. Photonic Crystals

Photonic crystals (PhCs) are periodic structures, typically made of high permittivity materials, widely employed for light management. They can be used to enhance light absorption (*e.g* atop a silicon-based photovoltaic device) or light extraction from a bulk material (*e.g.* atop of a LED), integrated circuits (*e.g.* guiding light on a photonic chip for information processing), confine light in small volumes (*e.g.* for lasing), beam steering (*e.g.* for light coupling in an optical fiber). NIL is a powerful tool for texturing a material modifying its properties for light manipulation. This approach has been successfully exploited in this field being a high throughput and low-cost technique.

At the beginning of the 21$^{st}$ century, PhCs based on organic-inorganic material with a high refractive index (n~1.63 at 633 nm) was developed with a novel NIL approach[39]. These periodic nanostructures were prepared by patterning a thin film of methacrylate silica-titania hybrid via UV-NIL. Later on, another type of hybrid nanoparticles/polymer resists composite was proposed[63]. A mixture of $TiO_2$ nanoparticles and photoresist was directly patterned into large areas of 3D PhCs via UV-assisted NIL. The 3D PhC exhibited a photonic bandgap at about 840 nm (maximum reflectance ~ 72% at 840 nm). Moreover, the observed full stop-band in all directions indicates the fabrication of a true 3D PhC. Feedback control for alignment could be in principle used to improve the quality of these structures. This approach has the potential to scale up the technique to larger areas and higher throughputs at a low cost by using roll-to-roll fabrication.

## 3.2. Solar cells

Photonic structures such as photonic crystals and transparent electrodes find their applications in optoelectronic devices. As an example, we report here some cases relevant to photovoltaic cells. Being a scalable fabrication process, NIL can be in principle extended to large surfaces and fits thus the needs for large solar panels with integrated micro and nano-patterns. Later on, Polman's group reported the fabrication of different types of solar cells configuration by using NIL techniques[48,67,69,70]. In 2011, Ferry and coworkers[48] designed and fabricated periodic and random nano-scatter arrays for solar cells. The cells consisted of Ag, coating the different nanopatterned silica sol-gel exhibited an efficiency of about 9.5%.

The high conductivity of metals has stimulated interest in metal nanowire (NW) networks and meshes as alternatives to ITO. These geometries can be designed to provide improved optoelectronic performance relative to ITO, achieving concurrent improvements in both optical transparency and electrical conductivity. Van de Groep and coworkers[65] reported silver nanowires (Ag NWs) as transparent conducting electrodes (TCE). The performance parameters for Ag NWs cells were measured and compared with ITO-based reference cells. The efficiency of the ITO reference of 3.45% is higher than for the NWs ~ 2.7%[65].

Photocurrent and photoelectrical enhancement in solar cells developed rapidly by using dielectric materials. Extensive research has been done on light trapping in Si thin-film and organic solar cells. However, only a limited number of research groups have worked on light management in copper indium gallium selenide (CIGSe) cells. Light trapping in ultrathin CIGSe cells is challenging because of the required stability of the light-trapping geometry during the high-temperature growth process. Van Lare and coworkers[69] reported a new ultra-thin Cu (In, Ga)$Se_2$ (CIGSe) solar cells by nanoscale dielectric light scattering ($SiO_2$, $TiO_2$)[69].

Zinc oxide (ZnO) is currently one of the key functional materials in advanced optoelectronic and photonic applications, including photovoltaics, thanks to its high transparency across the solar spectrum and its excellent electrical properties. The external quantum efficiency (EQE) of ZnO-based NIL patterns with PDMS and PEN molds were measured[46] showing the lower cell response on the replica stamped with PDMS than with cells replica with PEN stamp[44,45].

3D patterning of $TiO_2$ /Ag films in plasmonic dye-sensitized solar cells (DSSCs) was demonstrated[52]. The photovoltaic properties of the DSSCs were studied in different configurations: pure $TiO_2$ film, planar $TiO_2$/Ag film, and 3D patterned $TiO_2$/Ag film. The generated conversion efficiency was 4.59%, 5.35%, and 5.69%, respectively[52]. Ultrathin GaAs solar cells with $TiO_2$/Ag nanostructured back mirror achieved an efficiency of 25% accompanied by a strong enhancement of EQE in the 600-900 nm wavelength range[64].

## 3.3. LEDs

Nanostructured devices with a high aspect ratio, lead to several advantages in light interaction, such as reflection and transmission. 3D nano-fabrication surfaces with NIL methods attribute the optimization in light transparency efficiency in light-emitting and laser diodes devices.

Therefore, since ZnO has excellent optical and electrical properties, it can be used for transparent electrodes in UV light-emitting diodes and laser diodes. For example, In 2012 Jo and coworkers[71] reported the fabrication of ZnO nanoparticles/resin composite patterned by UV-NIL. The optimization of the refractive index was made by adjusting the NP concentration.

## 3.4. Sensors

Most recently, Zeolitic imidazolate frameworks (ZIF-8) MOF-based 2D photonic structures were prepared either by direct T-NIL of ZIF-8 or by its deposition on a $TiO_2$ line array prepared by T-NIL as a diffraction grating, enabling easy detection of organic solvent vapors, by a simple smartphone camera. The sensing approach is based on the variation of the optical properties of MOF patterns, induced by the selective adsorption of the organic solvent. The comparison of the optical responses reveals that both configurations exhibited similar sensitivity (Figure 1-8)[57].

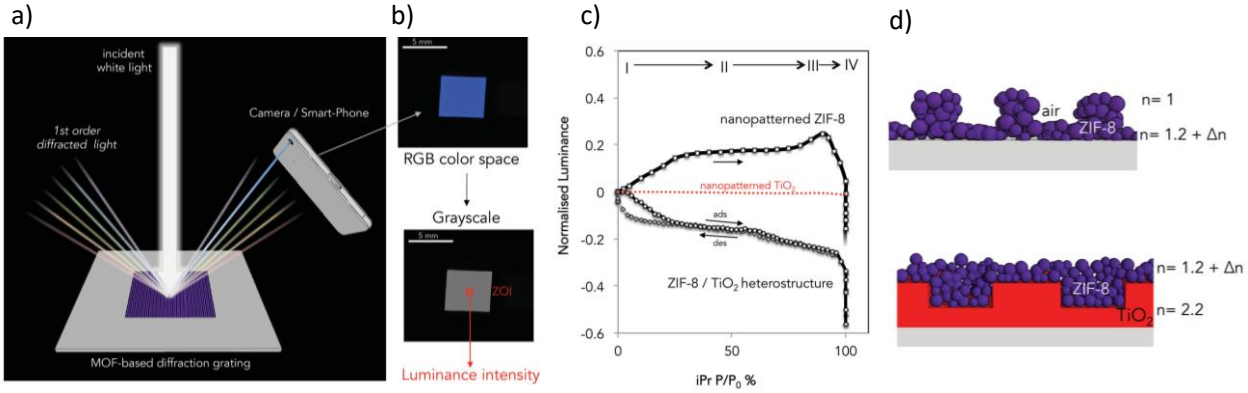



Figure 1-8. a) Illustration of the experimental set-up for the detection by a simple camera, b) Photographs of the diffracting grating in color and grayscale are taken by a smartphone photo camera, c) Isopropyl alcohol uptake measured by luminance difference, d) Illustration of the patterned ZIF-8 and ZIF-8/$TiO_2$ heterostructure with opposite refractive index evolution as a function of the vapor adsorption[58].

## 3.5. Anti-reflection coatings

Efficient Anti-Reflection Coatings (ARCs) have been extensively studied and are nowadays well established in industrial applications over large scales (*e.g.,* for photovoltaic, optoelectronic devices, laser windows, and much more). ARC-based multilayered thin films, refractive index gradient, and surface texturing with micro/nanostructures have been optimized with many different methods[66]. Van de Greop and coworkers in 2015[65] reported silica nano cylinders by conformal contact NIL. The obtained patterns have an effective-index of about 1.20, reducing the double-sided reflection from a glass slide from 7.35% to 0.57% (with a minimum reflectance <0.05% at 590 nm). A nanoimprinted AR coating was applied to Si photovoltaic cells encapsulated in glass. Photovoltaic modules showed a 3.8% relative increase in short-circuit current, corresponding to a 2.8% relative increase in power output.

# 4. Conclusion

This chapter presented substantial explanations in nanofabrication and NIL methods. Moreover, information from past and recent progress in NIL, optimization of replication in hard inorganic materials by soft-NIL, and its advantages compared to conventional lithography methods are described. The compatibility of these techniques lays in a plethora of inorganic material compositions. Such versatility and high throughput characteristics make it ideal for scale-up and production on large surfaces. This technique, first inspired by embossing techniques, was developed for soft polymer processing, as final or intermediate materials, but is today fully adapted to hard inorganic materials with high dielectric constant, such as metal oxides, with countless chemical compositions provided by the sol-gel chemistry. Whatever the chosen method of processing, optimizing replications in inorganic material by soft-NIL is a question of adapting the chemistry of the initial solution "resin" and the processing conditions. UV-NIL has been the preferred method for a long time, however, it requires complex chemistry, involving expensive and often toxic photo-initiators. More recently, thermal NIL coupled with pressure or vapor pressure control has been developed, allowing the use of simpler chemistry. For pure inorganic systems, when the final materials need to be organic-free, a final thermal treatment is very often necessary, not only to decompose the organic residues (binders, fluidizers, photo-initiators) but also to mechanically consolidate the edifice by viscous or diffuse sintering. Compromises must be found since this final treatment is accompanied by a more or less pronounced volume shrinkage. Two routes have been explored yet. The first one uses "small" (molecular) dissolved precursors, whereas the second one uses "large" building blocks (nanoparticles) from dispersion. Combinations of the two methods have been explored as composite precursors since they both originate from the same compatible sol-gel chemistry. On one hand, it has been proven that the higher is the concentration of dense nanoparticles, the lower is the shrinkage thanks to highly condensed buildings block. On the other hand, using nanoparticles induces the presence of high surface roughness and residual porosity that may be issued for some applications. For instance, when the features to reproduce are small, one would prefer using molecular precursors to obtain dense and smooth features. Obtaining a faithful replication that is at the same time smooth and dense (shrinkage-free) in pure inorganic material by soft-NIL remains a challenge and seems yet to be unreachable with the methods reported so far. Consequently, NIL has become a versatile, high throughput, and highly precise microfabrication method that is mature for lab developments and scaling up. Latterly, the final part is devoted to relevant applications in domains of interest. In the next chapter, advances in using sol-gel thin film, combined with the environmental control T-NIL method, will be explored. Moreover, nanopillars obtained by this approach will introduce an applicational potential as a robust and broadband antireflection coating.

# 5. References


[1] H.-T. Chen, A. J. Taylor, N. Yu, *Rep. Prog. Phys.* **2016**, *79*, 076401.
[2] D. Jang, L. R. Meza, F. Greer, J. R. Greer, *Nat. Mater.* **2013**, *12*, 893.
[3] F. H. Schacher, P. A. Rupar, I. Manners, *Angew. Chem. Int. Ed.* **2012**, *51*, 7898.
[4] C. Sanchez, C. Boissière, D. Grosso, C. Laberty, L. Nicole, *Chem. Mater.* **2008**, *20*, 682.
[5] M. Faustini, C. Boissière, L. Nicole, D. Grosso, *Chem. Mater.* **2014**, *26*, 709.
[6] C. Park, J. Yoon, E. L. Thomas, *Polymer* **2003**, *44*, 6725.
[7] M. Faustini, D. Grosso, *Comptes Rendus Chim.* **2016**, *19*, 248.
[8] C. Zheng, A. Hu, T. Chen, K. D. Oakes, S. Liu, *Appl. Phys. A* **2015**, *121*, 163.
[9] K. Sugioka, *Nanophotonics* **2017**, *6*, 393.
[10] M. Malinauskas, A. Žukauskas, S. Hasegawa, Y. Hayasaki, V. Mizeikis, R. Buividas, S. Juodkazis, *Light Sci. Appl.* **2016**, *5*, e16133.
[11] D. Bratton, D. Yang, J. Dai, C. K. Ober, *Polym. Adv. Technol.* **2006**, *17*, 94.
[12] R. P. Chaudhary, A. Jaiswal, G. Ummethala, S. R. Hawal, S. Saxena, S. Shukla, *Addit. Manuf.* **2017**, *16*, 30.
[13] M. Totzeck, W. Ulrich, A. Göhnermeier, W. Kaiser, *Nat. Photonics* **2007**, *1*, 629.
[14] E. Sakai, *ArXivquant-Ph0405069* **2005**.
[15] L. Bruchhaus, P. Mazarov, L. Bischoff, J. Gierak, A. D. Wieck, H. Hövel, *Appl. Phys. Rev.* **2017**, *4*, 011302.
[16] Y.-L. Liao, Y. Zhao, *Results Phys.* **2020**, *17*, 103072.
[17] R. Stoian, M. K. Bhuyan, G. Zhang, G. Cheng, R. Meyer, F. Courvoisier, *Adv. Opt. Technol.* **2018**, *7*, 165.
[18] R. Osellame, S. Taccheo, M. Marangoni, R. Ramponi, P. Laporta, D. Polli, S. De Silvestri, G. Cerullo, *J. Opt. Soc. Am. B* **2003**, *20*, 1559.
[19] Y. Xia, G. M. Whitesides, *Angew Chem Int Ed* **1998**, 26.
[20] S. Y. Chou, P. R. Krauss, P. J. Renstrom, *Science* **1996**, *272*, 85.
[21] M. A. Verschuuren, M. Megens, Y. Ni, H. van Sprang, A. Polman, *Adv. Opt. Technol.* **2017**, *6*.
[22] K. Heuberger, W. Lukosz, *Appl. Opt.* **1986**, *25*, 1499.
[23] S. Mani, 127.
[24] N. Stafie, D. F. Stamatialis, M. Wessling, *Sep. Purification Technol.* **2005**, 13.
[25] E. Delamarche, H. Schmid, B. Michel, H. Biebuyck, *Adv. Mater.* **1997**, *9*, 741.
[26] C. Y. Hui, A. Jagota, Y. Y. Lin, E. J. Kramer, *Langmuir* **2002**, *18*, 1394.
[27] M. A. Verschuuren, Substrate conformal imprint lithography for nanophotonics, [s.n.], S.l., **2010**.
[28] M. A. Schmidt, D. Y. Lei, L. Wondraczek, V. Nazabal, S. A. Maier, *Nat. Commun.* **2012**, *3*, 1108.
[29] N. Y. Lee, J. R. Lim, M. J. Lee, J. B. Kim, S. J. Jo, H. K. Baik, Y. S. Kim, *Langmuir* **2006**, *22*, 9018.
[30] D. Trimbach, K. Feldman, N. D. Spencer, D. J. Broer, C. W. M. Bastiaansen, *Langmuir* **2003**, *19*, 10957.
[31] C. Sanchez, C. Boissière, D. Grosso, C. Laberty, L. Nicole, *Chem. Mater.* **2008**, *20*, 682.

[32] C. J. Brinker, In *Chemical Solution Deposition of Functional Oxide Thin Films* (Eds.: Schneller, T.; Waser, R.; Kosec, M.; Payne, D.), Springer Vienna, Vienna, **2013**, pp. 233–261.
[33] C. Peroz, V. Chauveau, E. Barthel, E. Søndergård, *Adv. Mater.* **2009**, *21*, 555.
[34] H.-H. Park, D.-G. Choi, X. Zhang, S. Jeon, S.-J. Park, S.-W. Lee, S. Kim, K. Kim, J.-H. Choi, J. Lee, D. K. Yun, K. J. Lee, H.-H. Park, R. H. Hill, J.-H. Jeong, *J. Mater. Chem.* **2010**, *20*, 1921.
[35] H. Hlaing, X. Lu, C.-Y. Nam, B. M. Ocko, *Small* **2012**, *8*, 3443.
[36] R. Kothari, M. R. Beaulieu, N. R. Hendricks, S. Li, J. J. Watkins, *Chem. Mater.* **2017**, *29*, 3908.
[37] K. Hosokawa, K. Sato, N. Ichikawa, M. Maeda, *Lab. Chip* **2004**, *4*, 181.
[38] T. C. Merkel, V. I. Bondar, K. Nagai, B. D. Freeman, I. Pinnau, 20.
[39] K.-C. Kim, *Mater. Lett.* **2015**, *160*, 158.
[40] H.-B. Jo, K.-J. Byeon, H. Lee, M.-H. Kwon, K.-W. Choi, *J. Mater. Chem.* **2012**, *22*, 20742.
[41] E. Chong, S. Kim, J.-H. Choi, D.-G. Choi, J.-Y. Jung, J.-H. Jeong, E. Lee, J. Lee, I. Park, J. Lee, *Nanoscale Res. Lett.* **2014**, *9*, 428.
[42] R. Ganesan, J. Dumond, M. S. M. Saifullah, S. H. Lim, H. Hussain, H. Y. Low, *ACS Nano* **2012**, *6*, 1494.
[43] S. S. Dinachali, M. S. M. Saifullah, R. Ganesan, E. S. Thian, C. He, *Adv. Funct. Mater.* **2013**, *23*, 2201.
[44] C. Battaglia, J. Escarré, K. Söderström, L. Erni, L. Ding, G. Bugnon, A. Billet, M. Boccard, L. Barraud, S. De Wolf, F.-J. Haug, M. Despeisse, C. Ballif, *Nano Lett.* **2011**, *11*, 661.
[45] C. Battaglia, J. Escarré, K. Söderström, M. Charrière, M. Despeisse, F.-J. Haug, C. Ballif, *Nat. Photonics* **2011**, *5*, 535.
[46] J. Escarré, K. Söderström, C. Battaglia, F.-J. Haug, C. Ballif, *Sol. Energy Mater. Sol. Cells* **2011**, *95*, 881.
[47] F. Back, M. Bockmeyer, E. Rudigier-Voigt, P. Löbmann, *Thin Solid Films* **2014**, *562*, 274.
[48] V. E. Ferry, M. A. Verschuuren, M. C. van Lare, R. E. I. Schropp, H. A. Atwater, A. Polman, *Nano Lett.* **2011**, *11*, 4239.
[49] S.-H. Shin, S.-Y. Choi, M. H. Lee, J. Nah, *ACS Appl. Mater. Interfaces* **2017**, *9*, 41099.
[50] I. Park, S. H. Ko, H. Pan, C. P. Grigoropoulos, A. P. Pisano, J. M. J. Fréchet, E.-S. Lee, J.-H. Jeong, *Adv. Mater.* **2008**, *20*, 489.
[51] M.-G. Kang, M.-S. Kim, J. Kim, L. J. Guo, *Adv. Mater.* **2008**, *20*, 4408.
[52] W. Jiang, H. Liu, L. Yin, Y. Ding, *J. Mater. Chem. A* **2013**, *1*, 6433.
[53] D. Visser, D. Y. Chen, Y. Désières, A. P. Ravishankar, S. Anand, *Sci. Rep.* **2020**, *10*, 12527.
[54] W. Zhang, J. Tu, W. Long, W. Lai, Y. Sheng, T. Guo, *Energy Procedia* **2017**, *130*, 72.
[55] A. Letailleur, J. Teisseire, N. Chemin, E. Barthel, E. Søndergård, *Chem. Mater.* **2010**, *22*, 3143.
[56] S. B. Khan, H. Wu, Z. Xie, W. Wang, Z. Zhang, *ACS Appl. Mater. Interfaces* **2017**, *9*, 36327.
[57] O. Dalstein, D. R. Ceratti, C. Boissière, D. Grosso, A. Cattoni, M. Faustini, *Adv. Funct. Mater.* **2016**, *26*, 81.
[58] M. Faustini, A. Cattoni, J. Peron, C. Boissière, P. Ebrard, A. Malchère, P. Steyer, D. Grosso, *ACS Nano* **2018**, *12*, 3243.
[59] T. Bottein, T. Wood, T. David, J. B. Claude, L. Favre, I. Berbézier, A. Ronda, M. Abbarchi, D. Grosso, *Adv. Funct. Mater.* **2017**, *27*, 1604924.
[60] T. Bottein, O. Dalstein, M. Putero, A. Cattoni, M. Faustini, M. Abbarchi, D. Grosso, *Nanoscale* **2018**, *10*, 1420.

[61] M. Naffouti, R. Backofen, M. Salvalaglio, T. Bottein, M. Lodari, A. Voigt, T. David, A. Benkouider, I. Fraj, L. Favre, A. Ronda, I. Berbezier, D. Grosso, M. Abbarchi, M. Bollani, *Sci. Adv.* **2017**, *3*, eaao1472.
[62] S. Checcucci, T. Bottein, M. Gurioli, L. Favre, D. Grosso, M. Abbarchi, *Adv. Opt. Mater.* **2019**, 1801406.
[63] M. R. Beaulieu, N. R. Hendricks, J. J. Watkins, *ACS Photonics* **2014**, *1*, 799.
[64] H.-L. Chen, A. Cattoni, R. De Lépinau, A. W. Walker, O. Höhn, D. Lackner, G. Siefer, M. Faustini, N. Vandamme, J. Goffard, B. Behaghel, C. Dupuis, N. Bardou, F. Dimroth, S. Collin, *Nat. Energy* **2019**, *4*, 761.
[65] J. van de Groep, D. Gupta, M. A. Verschuuren, M. M. Wienk, R. A. J. Janssen, A. Polman, *Sci. Rep.* **2015**, *5*, 11414.
[66] H. K. Raut, V. A. Ganesh, A. S. Nair, S. Ramakrishna, *Energy Environ. Sci.* **2011**, *4*, 3779.
[67] J. van de Groep, P. Spinelli, A. Polman, *Nano Lett.* **2015**, *15*, 4223.
[68] C. M. Doherty, G. Grenci, R. Riccò, J. I. Mardel, J. Reboul, S. Furukawa, S. Kitagawa, A. J. Hill, P. Falcaro, *Adv. Mater.* **2013**, *25*, 4701.
[69] C. van Lare, G. Yin, A. Polman, M. Schmid, *ACS Nano* **2015**, *9*, 9603.
[70] M. W. Knight, J. van de Groep, P. C. P. Bronsveld, W. C. Sinke, A. Polman, *Nano Energy* **2016**, *30*, 398.
[71] H.-B. Jo, K.-J. Byeon, H. Lee, M.-H. Kwon, K.-W. Choi, *J. Mater. Chem.* **2012**, *22*, 20742.

# Chapter 2: Methylated Silica Surfaces Having Tapered Nipple-Dimple Nano-pillar Morphologies as Robust, Broad-Angle, and Broadband Anti-Reflection Coatings

Anti-Reflection coatings (ARCs) have been involved in the highly effective reflectance-reducing components for various optical and optoelectrical equipment. In recent years, the enhancement of anti-reflection coatings extensively developed by nanotechnology techniques. Fabricating ARC is critical and competitive, indeed there are several criteria factors required to have perfect anti-reflection coatings such as broadband, broad-angle, omnidirectional, high aspect ratio nanostructures patterns, robust and large area implementation. In this chapter mechanically, chemically, and thermally resistant broadband and broad-angle Anti-Reflection Coatings assembled on 10 cm diameter glass substrates will be demonstrated. By combining sol-gel deposition (*e.g.* spin coating) and nano-imprint lithography (environmental control T-NIL) homogenous and faithfully replicated nanostructures are fabricated. These nano-structured are composed of water-repellent methylated silica ($Si_4O_7Me_2$) with nipple-dimple featuring (pillars and holes) a record vertical aspect ratio of ~ 1.7. Moreover, its transverse refractive index gradient is created by tapered nipple-dimple pillars between 1.2 and 1.26. Total transmission for double-face nano-imprint wafers reaches 96~97% in the visible range, it is limited by specular reflection and mostly by the intrinsic diffusion of the glass substrate. The anti-reflective effect is effective up to ~ 60 degrees incidence angle. We address the robustness of the inorganic-based coating in various realistic and extreme conditions comparing them to the organic Perfluoropolyether (PFPE) counterpart (master reference). The sol-gel system is extremely more stable at high temperatures than the polymer reference. Both systems showed excellent chemical stability, except in strongly alkaline conditions. The inorganic nano-structure showed abrasion resistance more than two orders of magnitude superior to the polymer one, with less than 20% loss of anti-reflective performance after 2000 rubbing cycles under ~ 2 $Ncm^{-2}$ pressure. This difference springs from the large elastic modulus of the sol-gel material combined with excellent adhesion to the substrate and the specific nipple-dimple conformation. The presence of holes allows maintaining a refractive index gradient profile even after tearing out part of the nano-pillars population. Our results are relevant to applications where transparent windows with broad-band and broad-angle transmission are needed, such as protective glasses coating for photovoltaic panels or C-MOS cameras.

# 1. Introduction

Efficient Anti-Reflection Coatings (ARC) have been extensively studied and are nowadays well established in industrial applications over large scales (*e.g.* for photovoltaic, optoelectronic devices, laser windows, and much more)[1–5]. ARC-based multilayered thin films, refractive index gradient, and surface texturing films have been optimized with many different methods[1,6–9]. Thereby, for solving this issue, omnidirectional, broad-angle, and broad-band ARC have been developed. Beyond optical performances (*e.g.* improved transmission over a broad spectral band and a broad acceptance angle), there are several other features, such as ease of implementation over large scales, mechanical, thermal, and chemical stability, rendering an ARC a competitive device that is not commonly addressed in most reported works[6],[10],[11],[12].

The most common ARCs are two-dimensional layers. Their working principle is destructive interference of reflected and impinging light. This kind of 2D ARC is extremely well-developed thanks to the ease of implementation, cost-effectiveness, and hydrophobicity[9]. However, owing to the underlying working principle, they can be optimized only for a specific angle, limiting their performances in applications where the incidence of the impinging light beam can change (*e.g.* in photovoltaic)[1],[3]. This is why advanced nano-fabrication techniques were developed to produce ordered and disordered 3D sub-micrometric structures extending the performances of ARC to larger angles. Besides, the presence of such 3D structures is extremely useful to suppress diffraction and thus spectral and angular dependence of their optical properties. These structures can exploit resonance effects of high-permittivity particles (*e.g.* dielectric-based such as Si[13],[14] Ge[15] and $TiO_2$[16],[17], or metallic-based, such as Au resonators[18]). Other materials featuring a lower dielectric constant (such as polymers and silica) have been used to produce a refractive index gradient on glass, providing an adiabatic change of optical constant from air (n = 1) to the underlying material (*e.g.* n ~ 1.5 for glass)[19],[20]. For this latter working principle, the effective refractive index of the graded layer should be close to the square root of the substrate one (Fresnel's law[1]). If the substrate is glass, materials that are non-absorbing at visible frequencies and exhibit an intrinsic refractive index of typically between 1.37 and 1.70 are used in combination with voids[9]. The 3D structures must be composed of features having dimension and pitch much below the wavelength of the impinging visible radiation (typical size ~ 100 nm) to prevent scattering and diffraction, and have a large vertical to horizontal size aspect ratio. These features render their implementation challenging.

Ideal moldable materials gathering all the required properties can be found in organic polymers. They can be processed with high throughput soft-NIL methods[21],[22],[23],[24] that consist of imprinting the soft-viscous material with an elastomeric stamp before consolidation. 3D micro-and nanostructures made of thermoplastic organic polymers, such as PMMA, have been elaborated on a plethora of substrates. However, 3D structures made of plastic are mechanically fragile with respect to flat, dielectric layers. As such, they

do not provide the longevity necessary for instance, for integration onto photovoltaic panels (~ 20 years). Moreover, polymers are not very resistant to photobleaching and high temperature, rendering them more prone to deterioration. Furthermore, the detrimental impact of micro-and nano-plastic on the environment and their potential damage to human health demands a drastic reduction in the use of these materials. Alternatively, 3D nanostructures have been elaborated in hybrid (organic/inorganic)[25],[26],[27] silica through direct sol-gel NIL process[28] over relatively small glass wafers. They showed a remarkable reduction of reflection up to an acceptance angle of 60 degrees[3,13,15,17,29,30]. These results account for the relevance of this approach, however, mechanical, thermal, and chemical stability have not yet been properly addressed so far and the extension of the printed areas is still limited.

This chapter is dedicated to the elaboration and the complete characterization of sol-gel nano-imprinted methylated silica ($Si_4O_7Me_2$) nanostructures as an efficient graded ARC on the glass substrate. The imprint was performed by using a PDMS mold that was replicated from a commercial nipple-dimple Perfluoropolyether (PFPE) ARC (master) that is systematically used as a reference for comparing the performances of our methylated silica ARC. We first demonstrate the possibility to process sol-gel ARCs composed of nano-metric structures obtained by NIL over the record size of 10 cm diameter wafers (which is the maximal size of our PDMS mold), confirming the scalability and the cost-effectiveness of the method.

# 2. Experimental part

## 2.1. Thin-film Methylated silica ($Si_4O_7Me_2$) preparation

The methylated silica ($Si_4O_7Me_2$) sol-gel solution used to perform the investigation, was prepared from the molar ratio described in Table 2-1 (All chemicals were purchased from Aldrich).

Table 2-1. The molar ratio of precursors and chemical solvent for preparing methylated silica solution

| | **Precursors** | | **Solvents** | **Reactants** | **Surfactants** |
|---|---|---|---|---|---|
| **Materials** | Tetraethoxysilane (TEOS) | Methyltriethoxysilane (MTEOS) | EtOH | $H_2O$+HCl(1M) | Pluronic F127 (PEO-*b*-PBO) |
| **Molar ratios** | 0.5 | 0.5 | 20 | 5 | $4.10^{-4}$ |

After 24h aging, xerogel film was prepared by spin coating using POLOS TM equipment. Depositions were made on 10 cm glass substrates at 1500 rpm (10s) in room conditions. Thus, the refractive index n = 1.33 and the thickness of 480 nm methylated silica ($Si_4O_7Me_2$) sol-gel coating have been measured at a wavelength of 600 nm, using spectroscopic Ellipsometry (Woollan M2000V) and fitting the ellipsometry data with standard Cauchy model. The spin coating deposition technique and ellipsometry are explained in appendix 1 and 2.

## 2.2. Preparation of the nanopatterned ARC morphologies by environmental control T-NIL

Replication of the nanostructure patterns has occurred under the T-NIL method. As explained before in chapter one (generalities, T-NIL), one of the most recent and high-throughput methods is environmental control T-NIL. Environmental control during the NIL process is required. Therefore, as-prepared Methylated silica (MS) coating is transferred into a nano-imprint chamber in which a 70% relative humidity was maintained using a constant 5L.min$^{-1}$ flux of air generated from a homemade humidity controller system[28]. The nano-imprint was performed less than 1 min after spin-coating by applying the degassed PDMS mold onto the sol-gel film. Before unmolding, the system was cured at 70 °C for 20 min. Then, after peeling off the PDMS, the imprinted sample was annealed at 450 °C for 20 min to ensure the complete removal of the F127 polymer and

the condensation of the silica backbone. The PDMS mold was replicated from a commercial Perfluoropolyether Fluorolink (MD700) master. The master surface was rendered hydrophobic by immersion for 1h in a vapor of 1H,2H,2 Hperflunedectyl triethexysilane in a closed chamber, followed by an abundant rinsing with ethanol. The PDMS precursors and reactant mixture (90w% RTV141A; 10w% RTV141B from BLUESIL) was then poured onto the functionalized master surface and cured at 70 °C for one night. The PDMS mold is then peeled off the master surface after cooling. The mold is pumped in a primary vacuum for 10 min under ~ 10 mbar before imprinting as described previously.

The $Si_4O_7Me_2$ composition has been selected for its relatively low refractive index and hydrophobicity, as shown in a previous study[9]. Structural investigation of the nano-imprinted samples was performed by Atomic Force Microscopy (AFM) (PSIA XE-100 AFM) (see appendix 2) and high-resolution scanning electron microscopy (SEM) FEI Strata DB235 with 5 kV electron acceleration voltage.

First, the visual inspection of the coating revealed a slight diffused blue color all over the 10 cm coating if one observes at high incident angles (Figure 2-1 A)), originating from the diffraction of the nano-pillars array (see Figure 2-1 B)). Since this aspect is found all over the coating, one can state that the whole surface is homogeneously structured.

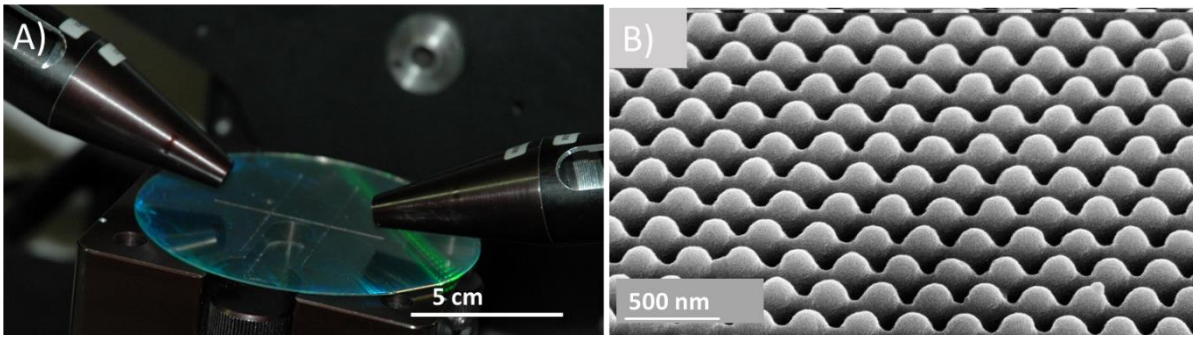



Figure 2-1. A) Picture of 10 cm diameter wafer coated with the nanoimprinted methylated silica ($Si_4O_7Me_2$) antireflection coating (MS ARC). B) Scanning electron microscopy (SEM) image tilted at 52 degree of MS ARC showed the faithfully replication.

Second, the profile scale of AFM microscopy from master polymer and nanoimprinted methylated silica ($Si_4O_7Me_2$) ARC is illustrated in Figures 2-2 A) and B). The reduction in height and pitch after replication has appeared. This lateral reduction is due to the shrinkage after the thermal annealing.

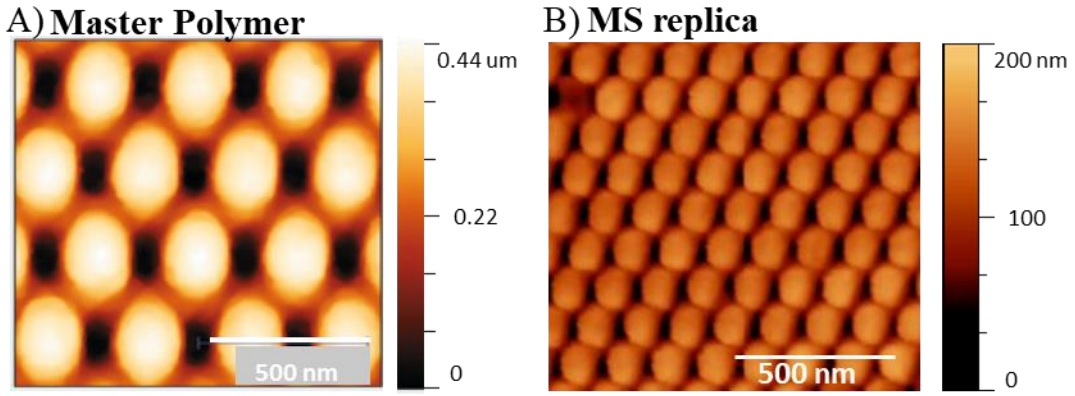



Figure 2-2. AFM images with the profile thickness scale from A) Master polymer and B) Replicated Methylated silica antireflection coating (MS ARC).

A more accurate description of the 3D structure of the surface has been deduced from SEM micrographs acquired in various configurations (Figure 2-3 C), D), E)). They revealed the expected nipple-dimple structure faithfully replicated from the perfluoropolyether ARC master. The structure is composed of intercalated hexagonal arrays of pillars and holes separated by a pitch of 270 nm. The pillars (nipples) have ~ 200 nm height and ~ 120 nm width (aspect ratio = 1.7), while the holes (dimples) are ~ 50 nm deep and ~ 100 nm width. Note that, previous reports on NIL of silica-based sol-gel coatings did not provide pillars featuring such a large vertical aspect ratio[31],[29] nor a nipple-dimple structure. Both characteristics are important to produce a smoother change of refractive index.

As it is mentioned before, the thickness and refractive index of the non-imprinted bare layer were measured around 480 nm and 1.33 at a wavelength of 600 nm, respectively. Since silica has a refractive index of around 1.5, the measured value of n = 1.33 suggests that the layer has a residual porosity P of around 33% vol. By taking into account these optical and structural features, we deduce the transverse profile of void-to-material volume fraction, the corresponding refractive index profile, and the global effective refractive index ($n_{eff}$). Figure 2-3 B) reports this profile assuming a linear effective medium approximation (EMT)[32],[33]. The coating is thus composed of three layers: the non-imprinted residual layer, which is pristine material at the bottom ($n_{bot}$ = 1.33, $h_{bot}$ = 350 nm), the layer bearing holes in the middle ($n_{mid}$ = 1.21, $h_{mid}$ = 50 nm), and the top layer composed of pillars ($n_{top}$ = 1.13, $h_{top}$ = 150 nm). Assuming a simplified geometry of the structure, the refractive index profile has been slightly smoothed at the top and bottom edges in order to better reproduce the edge shapes observed in the real structures. The resulting calculated effective refractive index is $n_{eff}$ = 1.27 at 600 nm.

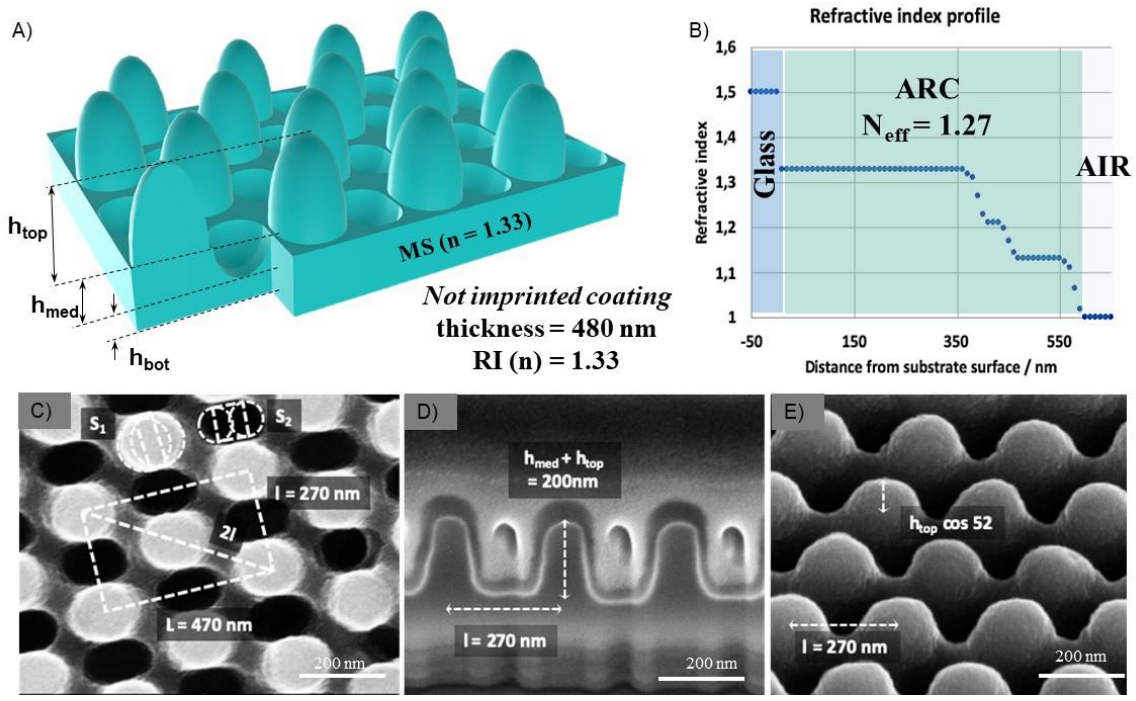



Figure 2-3. A) Scheme illustrating the topography of the nipple-dimple surface. B) Refractive index profile of the Methylated Silica (MS) ARC system deduced from the structure geometry. C) to E) SEM images of the MS ARC from the top (C), from the side after FIB-preparation (D), and from a 52° tilted angle (E). Typical dimensions of the structure have been measured on SEM images (E, F, G) and are reported in each image for clarity. These have been used to calculate the volume fraction transversal profile of the ARC, from which the refractive index profile (B) was deduced using a linear medium approximation (S1, S2 correspond to projected surface of the nipple and dimple, respectively, modeled using 2 half circles sandwiching a rectangle).

# 3. Optical performance

Optical performances of ARC have been addressed by measuring (see Figure 2-4 and Figure 2-5) reflection, transmission, and diffusion of $Si_4O_7Me_2$ sol-gel layers (plain non-imprinted, single-face sol-gel ARC imprinted, double-face sol-gel ARC imprinted) and comparing them with those of the bare glass substrate and of the polymer master ARC (all substrates are from the same producer batch). Double face ARC imprinted on the other side of the glass substrate, followed the same procedure of environmental control T-NIL as explained previously.

All spectra in Figure 2-4 A and B were collected at quasi-normal incidence (12 degrees) using a spectrophotometer mounting an integrating sphere allowing to measure the spectral features of total reflection, reflected diffusion (that is total reflection minus specular reflection), and total transmission. Absorption can be excluded in the investigated range of wavelength for both the substrate and the sol-gel coatings in use. The transmitted intensity is larger for nanostructured Methylated Silica (MS) ARC and spectrally flatter with respect to the plain sol-gel, confirming the superior performances of graded systems (Figure 2-4 A)). The single-face sol-gel MS ARC allows for a transmission increase of 3% corresponding to the bare glass substrate, which is 1% above the PFPE graded counterpart polymer ARC. This improved transmission property is likely due to a lower $n_{eff}$ of the sol-gel layer compared to that of the polymer. A double-face imprinted $Si_4O_7Me_2$ sol-gel (MS ARC DF) shows a rather flat transmission of about 97% over the full visible spectrum. It is limited by specular reflection and reflected diffusion. Measuring the reflected scattering allows assessing the haze of the structure, which is an important parameter for using these devices in transmission (Figure 2-4 B). It emerges that bare glass scatters almost 3% of the impinging light, which is very similar to the plain (not imprinted) $Si_4O_7Me_2$ coated glass, scattering about 3%. This accounts for the high quality in terms of homogeneity and flatness of our sol-gel coatings. From the same analysis on 3D NIL structures (Figure 2-4 B) we observe that the polymer ARC scatters about 4-4.5% of the impinging light, whereas the MS ARC is in the 3-4% range demonstrating a reduced haze in our inorganic material with respect to the organic counterpart. Provided flat layers scatter only ~ 3% of the light, we deduce that the diffusion from the nipple-dimple structure in MS ARC is about 1-2%. This also suggests that the intrinsic scattering from the underlying glass support is the main limiting factor for light transmission of the double face ARC shown in Figure 2-4 A.

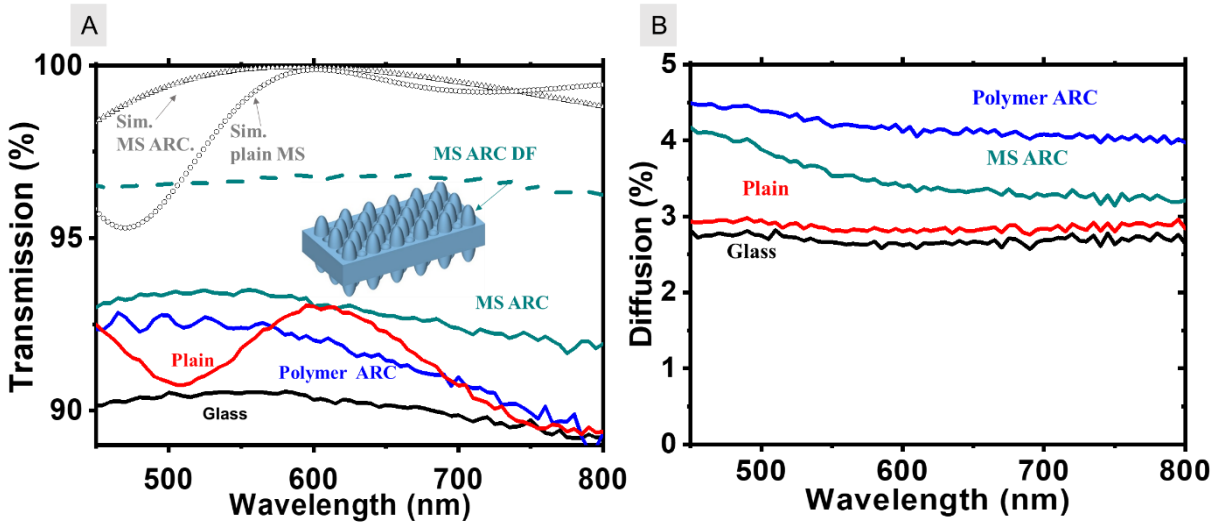



Figure 2-4. A) Total transmission spectra of single face NIL Methylated silica antireflection coating (MS ARC, green full curve), double-face NIL Methylated silica antireflection coating (MS ARC DF, green dashed curve), polymer ARC (blue curve), flat Methylated silica coating 480 nm thick (Plain, red curve) and bare glass (Glass, black curve). Symbols represent the theoretical prediction for a single layer of 120 nm with n = 1.225 (Sim. plain MS) and a composite layer (Sim. MS ARC.) composed by "bulk" sol-gel bottom layer ($n_{bot}$ = 1.33, $h_{bot}$ = 350 nm), the dimple middle layer ($n_{mid}$ = 1.21, $h_{mid}$ = 50 nm) and the nipple top layer ($n_{top}$ = 1.13, $h_{top}$ = 150 nm). B) Normalized diffusion spectra of samples MS ARC, Polymer ARC, Plain and Glass.

These performances in transmission are in line with those reported for double-side coated graded ARC systems[34],[35],[30],[36]. A graded ARC from a similar sol-gel hybrid material was reported[29], exhibiting an excellent ARC affect close to 0% in reflection (at ~ 560 nm) with a fluctuation of ~ 3% in the full visible range. Although no data for transmission were provided, the very low reflection for the double-coated system is likely due to the use of a high-quality, non-diffusive substrate, combined with the presence of nanostructures that provides a lower effective refractive index ($n_{eff}$ = 1.20)[29]. We trace the theoretical predictions (obtained with a transfer matrix method) for maximal transmission with single and multi-layered, double face ARC (Figure 2-4 A), gray curves). One case refers to a 120 nm thick layer having n ~ 1.225 (close to the square root of the refractive index of the underlying glass substrate), matching the conditions for maximal transmission at about 600 nm. The corresponding curve is rather flat and the fluctuation, in the considered spectral range, is less than 2%. The second simulation considers a more realistic structure, mimicking the composition of our graded-index, nipple-dimple ARC and it includes 3 (effective) layers: the "bulk" sol-gel bottom layer ($n_{bot}$ = 1.33, $h_{bot}$ = 350 nm), the dimple middle layer ($n_{mid}$ = 1.21, $h_{mid}$ = 50 nm) and the nipple top layer ($n_{top}$ = 1.13, $h_{top}$ = 150 nm). This structure shows a ~ 99% transmission at 600 nm, an overall fluctuation of about 5%, and a wavier behavior with respect to the single layer. This latter aspect depends mostly on the thick buffer layer of the "bulk" sol-gel bottom layer and could be improved, in principle, by choosing a thinner residual layer.

Comparing these simulations of flat layers with our data emerges that the use of a nipple-dimple architecture allows for a very small fluctuation in the investigated spectral range (about 1%), which is an appealing feature for broadband applications. We also note that the overall fluctuation in the measured transmission spectra is similar to that previously reported in similar structures[29].

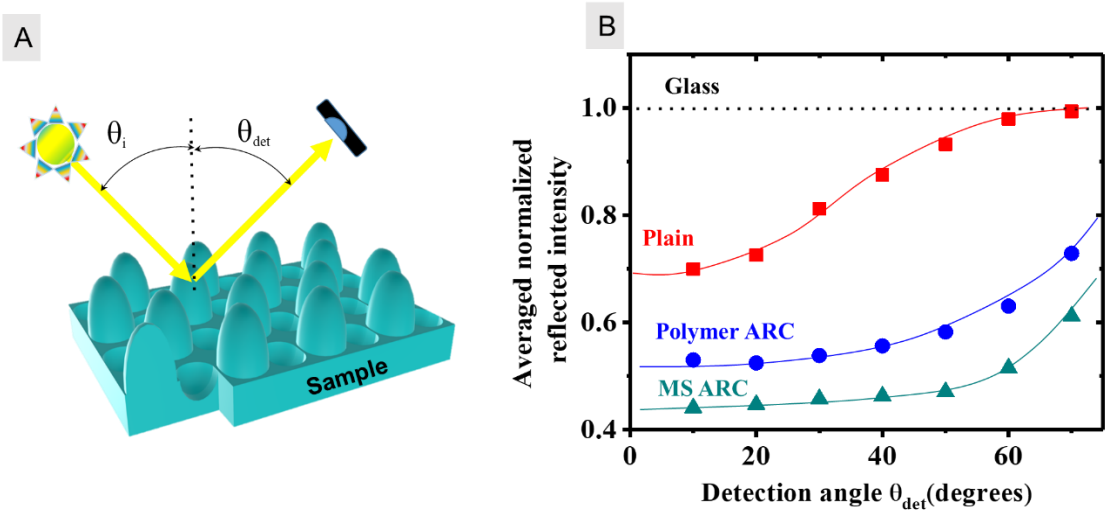



Figure 2-5. A) Scheme of the experimental setup for detecting the specular reflection. The angle of incidence of the illumination light beam ($\theta_{illumination}$) and that of the detection ($\theta_{detection}$) are the same. B) Angle-resolved specular reflection normalized to the reflection of the bare glass substrate (black dashed line, corresponding to MS ARC (green line), polymer ARC (blue line), MS (methylated silica) plain surface thin film (red line).

We assess the specular reflection of our samples by using a spectroscopic goniometer and setting illumination and detection angles to the same value ($\theta_i = \theta_{det}$, Figure 2-5 A) and B). In this setup, the light is almost collimated, thus defining a precise angle of incidence on the sample and focused in a spot of about 1 cm in diameter. As a reference for the specularly reflected intensity, we use the bare glass support that was used for all the NIL and flat coatings. The specular reflection was investigated from 10 to 70 degrees (in steps of 5 degrees) and each spectrum was normalized by that of glass specular reflection at the same angle (not shown). Thus, in this representation, the specular reflection of glass is, by definition, equal to 1 at any incidence angle. The normalized spectra are averaged in wavelength in the measured interval. From this investigation emerges that the flat sol-gel layer (Plain) progressively loses its ARC effect and quickly approaches 1 (at about 60 degrees of incidence it equals the glass, Figure 2-5 B). The specular reflection from the Polymer ARC is much flatter than the plain coating and keeps a value below 0.6 up to 50 degrees of beam incidence, accounting for the strength of the 3D ARC strategy concerning flat layers. Finally, our MS ARC is more performing than the polymer-based one both in terms of specular reflection intensity and acceptance angle, as it shows an even flatter response with angle. It shows an efficient anti-reflective effect up to about 60 degrees (< 0.5 corresponding to bare glass).

## 3.1. Abrasion resistance

Abrasion resistance was performed using a crock meter test, which consists of rubbing off, with a back and forth motion (an individual cycle corresponds to a back and forth movement of the pad), the top of the film with a pad covered with a calibrated fabric (ISO test method 105-F09) and loaded with a constant charge of 5 N (Pressure = 2.08 $Ncm^{-2}$). This crock meter has been used to evaluate the mechanical properties in terms of resistance to abrasion (Figure 2-6 A). Moreover, optical characterization of the reflected intensity after crock meter, was performed using a commercial ZEISS optical microscope (objective lens with magnification 10X, numerical aperture NA = 0.25). A confocal optical fiber (50 µm core diameter) is coupled with a spectrometer determining a lateral resolution of ~ 50 µm.

Scanning electron microscopy (at 52 degrees with respect to the sample normal) and optical microscopy images acquired every 10 cycles demonstrate that the master polymer is almost completely delaminated after only 20 cycles (Figure 2-6 B), whereas the methylated silica replica is almost intact after 1000 cycles (Figure 2-6 C). The detailed investigation of the surface appearance after 2000 crock meter cycles reveals the presence of trenches where holes (dimples) are observed together with bases of broken dimples. The presence of the residual dimples after rubbing contributes to maintaining a relatively good optical performance.

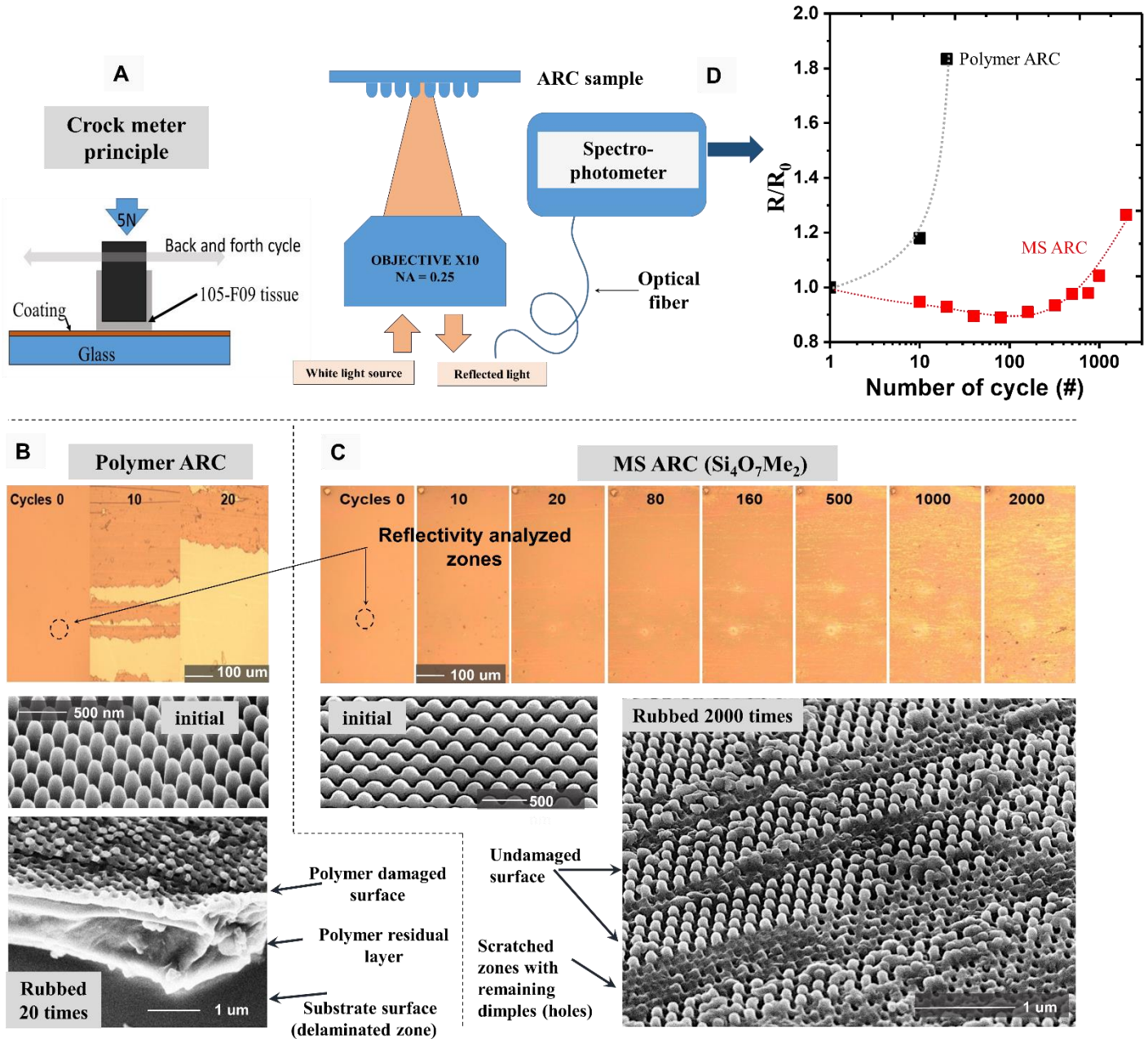



Figure 2-6. A) Scheme of the crock meter used for abrasion resistance of the coating against scratch by back and forth cycle. B) Optical and electronic microscope images collected from the polymer ARC surface before and after rubbing (0 to 20 cycles). C) Optical and electronic microscope images collected from the MS ARC (methylated silica) surface before and after rubbing (0 to 2000 cycles). D) Reflected intensity measured with an optical microscope for both Polymer ARC and MS ARC as a function of the number of abrasion cycles. The black circles on the optical images highlight the detection spot (diameter of about 50 μm) that is not changed during the mechanical test. The reflection was collected through an optical fiber and analyzed by spectrometer. It has been averaged over the investigated spectrum and integrated over the solid angle of 10X objective. The value has finally been normalized to the initial value at zero cycles ($R_0$) in order to monitor the evolution of the reflected intensity with the number of rubbing cycles. The dashed lines are guides to the eyes. All SEM images were collected with a 52 degrees tilted angle, respect to the sample normal.

This is confirmed by monitoring the evolution of the reflected intensity of both organic and inorganic samples during the crock meter test from 0 to 2000 cycles. The relative change of reflected intensity (with respect to the starting value $R_0$ measured at 0 cycles) was collected through an optical microscope equipped with a 10X objective lens and a confocal optical fiber fed into a spectrometer (lateral resolution ~ 50 µm, Figure 2-6 D). The evolution of the normalized reflection, that has been averaged over the investigated spectral range and integrated over the observation solid angle (the numerical aperture of the objective lens, NA = 0.25, defining a maximal acceptance angle of ~ 14.5 degrees), is provided for both polymers and inorganic ARC. Markers were used to reposition the sample under the microscope to always collect the light from the same area of the sample surface. Reflection spectra from the polymer master show a pronounced intensity increase after only 20 rubbing cycles, reaching a final value almost identical to that measured on the bare glass substrate (Figure 2-6 D). From SEM images in Figure 2-6 B), it is evident that the failure of the polymer ARC is due to delamination from the substrate, resulting from a poor adhesion of polymer materials on $SiO_2$. On the contrary, the methylated silica replica preserves a reflected intensity close to $R_0$ after 1000 cycles (Figure 2-6 D). The failure of this ARC is attributed to the pillar tearing-off, as observed and discussed above (Figure 2-6 C). However, in this case, no delamination is observed. Therefore, the slight and progressive decrease of reflectivity measured between 0 and 1000 cycles is related to the modification of the refractive index profile. Additional effects on the detected reflection within the limited NA of the objective lens in use may be the contribution of scattering induced by pillar scratching and reorganization on the surface. After 1000 cycles, the reflectivity increases due to the reduction of the effective refractive index associated with the elimination of part of the pillars. Nonetheless, the reflected intensity remains relatively low as a result of the presence of holes (dimples), reducing the effective refractive index and maintaining a refractive index gradient. This result clearly points out the superior performance of the nipples-dimples structure and of the sol-gel stiffness over the polymer-based ones.

A similar detailed analysis against mechanical abrasion was not performed in previous reports or was performed by measuring the resistance to scratch with a sharp tip[37], by tape stripping[29], and mostly on 2D thin film without any NIL pattern[2–4]. Moreover, a systematic investigation of the optical performances after scratch, as we show here, was not routinely performed[29], [37],[38],[39].

## 3.2. Thermal resistance

An assessment of the resilience of our structures against heating has been conducted to evaluate their thermal resistance (see Figure 2-7). We followed an optical protocol similar to that previously employed for the mechanical abrasion, to investigate the intensity reflected evolution. ARC based on Methylated silica and polymer were tested against annealing in air. The temperature ranged between 100 and 600 °C and was

changed in intervals of 50 °C. All the samples were exposed for 15 minutes for each temperature step.

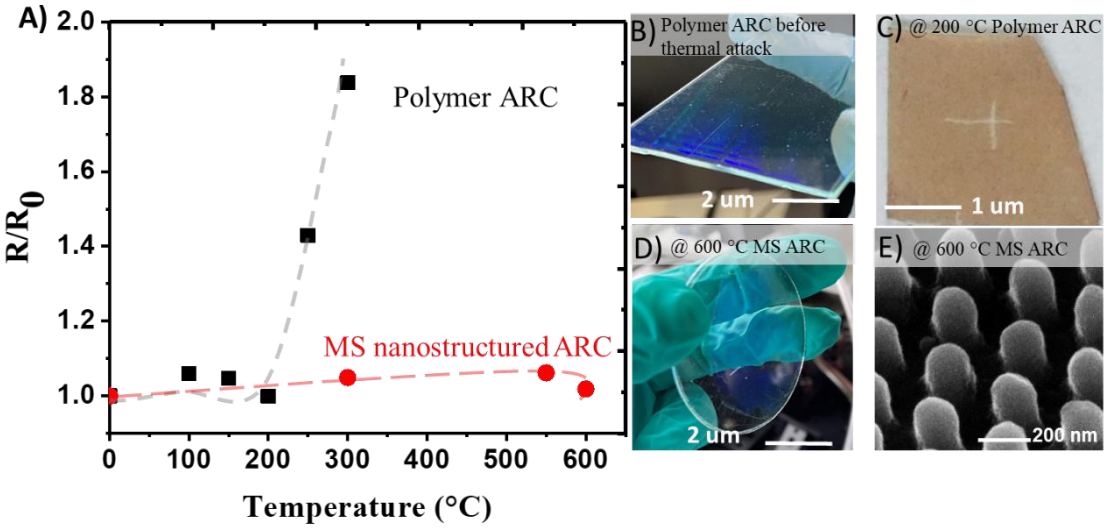



Figure 2-7. A) Reflection intensity, measured for both polymer ARC and MS ARC (methylated silica), under an optical microscope, as described in Figure 2-3 D (same conditions), with respect to temperature. The values of the reflected intensity have been averaged in the measured spectral range and normalized to the initial value at room temperature, ($R_0$). B) Optical image of polymer ARC before thermal annealing and C) after 15 min at 300 °C. D) MS ARC at 600 °C annealing temperature and E) SEM image of MS ARC after 15 min at 600 °C.

The reflectivity evolution has been monitored from room temperature up to 600 °C in steps of 50 °C (15 min annealing per step) in air. The increase in reflectivity is evident for the polymer after 300 °C, as a result of its thermal decomposition (also confirmed by optical inspection of the master polymer that becomes darker after annealing). However, the methylated silica replica features only a slight change of the reflectance ratio in all the investigated temperature ranges confirming its high thermal stability. SEM images after annealing account for this stability by revealing the unchanged features at the surface of the sample after 600 °C. This test demonstrates the remarkable robustness of silica-based ARCs and opens the possibility to use it for high optical transmission windows exposed to extreme conditions.

## 3.3. Chemical resistance

Once more, the same optical detection protocol was used to assess the stability of the ARCs when exposed to different, extreme, chemical conditions (pH, solvent). The test consists of dipping the samples for 15 minutes in acetone, ethanol, toluene, and acidic/oxidizing (aqueous 1M $HNO_3$) or alkaline (aqueous 1M NaOH) solutions. The

reflected intensity after dipping is normalized to that of the initial value before the chemical attack (Figure 2-8).

Both polymer and silica-based ARCs are stable in polar and non-polar solvents since no modification of the reflectivity has been observed. Concerning pH sensitivity, both systems are also extremely stable in acidic and oxidizing conditions. However, 15 min in 1 Mol sodium hydroxide induces an irreversible decrease of the reflectivity, suggesting that they have been chemically modified by the hydroxyl ions present in the solution. We attribute this change to the instability of silica at pH > 10[40]. In our case, it shows improved stability, comparable to the polymer one, as a result of its combination with methyl groups that makes it water repellent and therefore more stable in water. The difference in the spectral features of the reflectivity between both polymer and inorganic ARC is likely due to the difference in chemical attack mechanism that induces a different evolution of the refractive index profile. The study of the chemical mechanism behind this deterioration is out of the scope of this thesis and has not been investigated.

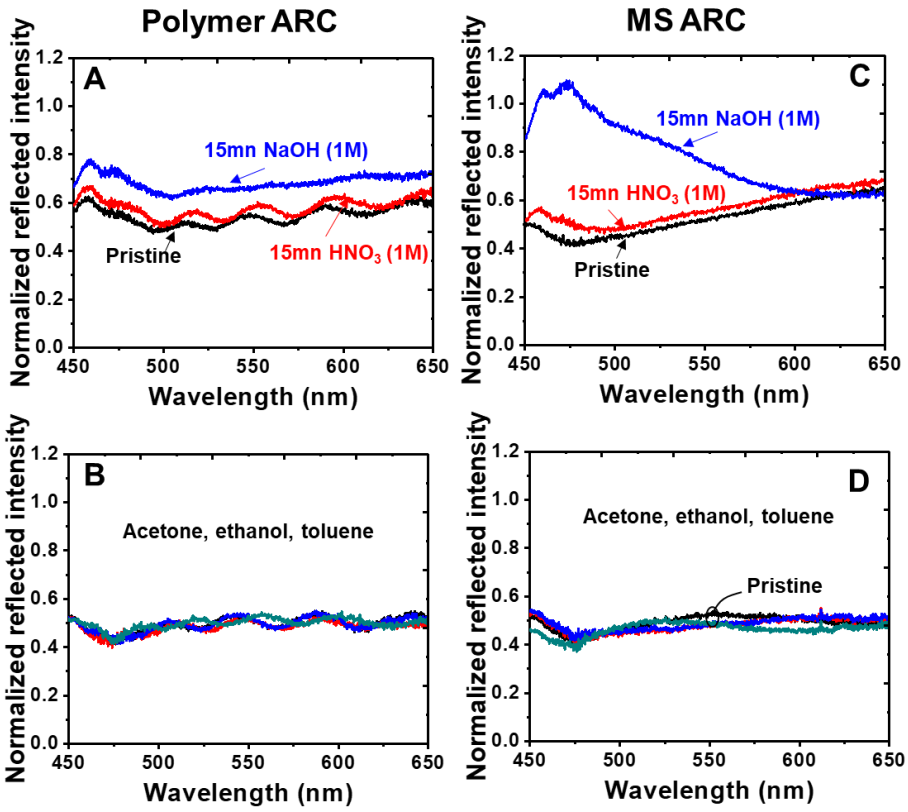



Figure 2-8. Reflection spectra for both polymer ARC and MS ARC before (pristine) and after immersion for 15 min in 1M nitrid acid ($HNO_3$), 1M sodium hydrixide (NaOH), (A and C, respectively), and acetone, ethanol and toluem (B and D, respectively).

# 4. Conclusion

In light of the previous considerations, direct printing of a sol-gel solution is a competitive and promising use of NIL processing for ARC. Indeed, it enables the formation of high[13,17] and low dielectric constant materials[31] and it skips many of the more or less cumbersome steps required by top-down etching.
Finally, NIL has been extensively exploited to form low-dimensional structures. Its direct use with polymers has been one of the first examples to produce efficient ARC[1,41]. However, owing to the limited dielectric constant of this class of materials, they can be used as ARC only on comparably low refractive index substrates (*e.g.* glass). In addition to this, as we thoroughly demonstrated in our work, they suffer from relatively low resistance to rubbing and to high temperature, rendering them less adapted to work in extreme conditions with respect to more stable, dielectric materials as the silica used here.
Further use of NIL of polymers for ARC includes further etching steps: first, a polymeric resist is spread on a surface, printed with a mold, and densified (*e.g.* by heating or UV curing). These printed structures are used to protect the parts of the underlying surface that should be preserved during the following etching step that can be performed via selective chemical attack or *via* reactive ion etching. Finally, the residual resist is removed with a solvent leaving 3D structures (that can be eventually of the larger refractive index of the polymer used for the NIL step). This is for instance the process used in some studies[13] to create a broad-band and broad-angle ARC on a Si wafer. Due to the many steps required in this approach, this kind of ARC, although performing, is hardly scalable (*e.g.* to a roll-to-roll chain of production). To summarize, we showed that the sol-gel soft-NIL method can be implemented on at least 10 cm diameter substrates, which is extremely well-adapted to elaborate graded ARCs (mostly single or double faces) on glass. The total transmission reaches ~ 97% in the whole visible range (limited by the scattering from the underlying glass substrate), and for angular incidences below 60 degrees, with less than 1% fluctuation in the investigated spectral range. We also demonstrate that sol-gel materials combined with a nipple-dimple conformation gather optimal optical performances high stability against abrasion, extreme temperatures, and chemical attacks. These results confirm that, due to their processability, the versatility to adjust their optical constants, and their robustness, sol-gel materials are ideal systems to serve as nanostructured ARC over large surfaces.

# 5. References


[1] H. K. Raut, V. A. Ganesh, A. S. Nair, S. Ramakrishna, *Energy Environ. Sci.* **2011**, *4*, 3779.
[2] T. Ootsuka, Z. Liu, M. Osamura, Y. Fukuzawa, R. Kuroda, Y. Suzuki, N. Otogawa, T. Mise, S. Wang, Y. Hoshino, Y. Nakayama, H. Tanoue, Y. Makita, *Thin Solid Films* **2005**, *476*, 30.
[3] H. K. Raut, S. S. Dinachali, Y. C. Loke, R. Ganesan, K. K. Ansah-Antwi, A. Góra, E. H. Khoo, V. A. Ganesh, M. S. M. Saifullah, S. Ramakrishna, *ACS Nano* **2015**, *9*, 1305.
[4] K.-S. Han, J.-H. Shin, W.-Y. Yoon, H. Lee, *Sol. Energy Mater. Sol. Cells* **2011**, *95*, 288.
[5] M. H. Elshorbagy, K. Abdel-Hady, H. Kamal, J. Alda, *Opt. Commun.* **2017**, *390*, 130.
[6] L. Ye, Y. Zhang, X. Zhang, T. Hu, R. Ji, B. Ding, B. Jiang, *Sol. Energy Mater. Sol. Cells* **2013**, *111*, 160.
[7] X. Li, J. Gao, L. Xue, Y. Han, *Adv. Funct. Mater.* **2010**, *20*, 259.
[8] J. Moghal, J. Kobler, A. A. R. Watt, G. Wakefield, *ACS Appl Mater Interfaces* **2012**, 6.
[9] M. Boudot, V. Gaud, M. Louarn, M. Selmane, D. Grosso, *Chem. Mater.* **2014**, *26*, 1822.
[10] T. Yanagishita, T. Kondo, H. Masuda, *J. Vac. Sci. Technol. B Nanotechnol. Microelectron. Mater. Process. Meas. Phenom.* **2018**, *36*, 031802.
[11] W. Wei, X. Zhu, Y. Zhao, Q. Wu, **2015**, 4.
[12] C.-J. Ting, M.-C. Huang, H.-Y. Tsai, C.-P. Chou, C.-C. Fu, *Nanotechnology* **2008**, *19*, 205301.
[13] P. Spinelli, M. A. Verschuuren, A. Polman, *Nat. Commun.* **2012**, *3*, 692.
[14] A. Cordaro, J. van de Groep, S. Raza, E. F. Pecora, F. Priolo, M. L. Brongersma, *ACS Photonics* **2019**, *6*, 453.
[15] M. Bouabdellaoui, S. Checcucci, T. Wood, M. Naffouti, R. P. Sena, K. Liu, C. M. Ruiz, D. Duche, J. le Rouzo, L. Escoubas, G. Berginc, N. Bonod, M. Zazoui, L. Favre, L. Metayer, A. Ronda, I. Berbezier, D. Grosso, M. Gurioli, M. Abbarchi, *Phys. Rev. Mater.* **2018**, *2*.
[16] A. Lin, Y.-K. Zhong, S.-M. Fu, *Opt. Express* **2013**, *21*, A1052.
[17] T. Bottein, T. Wood, T. David, J. B. Claude, L. Favre, I. Berbézier, A. Ronda, M. Abbarchi, D. Grosso, *Adv. Funct. Mater.* **2017**, *27*, 1604924.
[18] M. Keshavarz Hedayati, M. Abdelaziz, C. Etrich, S. Homaeigohar, C. Rockstuhl, M. Elbahri, *Materials* **2016**, *9*, 636.
[19] J. Hiller, J. D. Mendelsohn, M. F. Rubner, *Nat. Mater.* **2002**, *1*, 59.
[20] P. Buskens, M. Burghoorn, M. C. D. Mourad, Z. Vroon, *Langmuir* **2016**, *32*, 6781.
[21] B. Bläsi, N. Tucher, O. Höhn, V. Kübler, T. Kroyer, Ch. Wellens, H. Hauser, (Eds.: Thienpont, H.; Mohr, J.; Zappe, H.; Nakajima, H.), Brussels, Belgium, **2016**, p. 98880H.
[22] M. Burghoorn, D. Roosen-Melsen, J. de Riet, S. Sabik, Z. Vroon, I. Yakimets, P. Buskens, *Materials* **2013**, *6*, 3710.
[23] J.-H. Shin, B.-N. Go, H.-J. Choi, J.-Y. Cho, A. S. S. Lee, S. S. Hwang, H. J. Cha, H. Lee, *J. Mater. Chem. C* **2014**, *2*, 5864.
[24] Fabrication of n- and p-Type Organic Thin Film Transistors with Minimized Gate Overlaps by Self-Aligned Nanoimprinting, .
[25] Y. Zou, L. Moreel, H. Lin, J. Zhou, L. Li, S. Danto, J. D. Musgraves, E. Koontz, K. Richardson, K. D. Dobson, R. Birkmire, J. Hu, *Adv. Opt. Mater.* **2014**, *2*, 759.
[26] S. S. Dinachali, J. Dumond, M. S. M. Saifullah, K. K. Ansah-Antwi, R. Ganesan, E. S. Thian, C. He, *ACS Appl. Mater. Interfaces* **2013**, *5*, 13113.
[27] H.-H. Park, D.-G. Choi, X. Zhang, S. Jeon, S.-J. Park, S.-W. Lee, S. Kim, K. Kim, J.-H. Choi, J. Lee, D. K. Yun, K. J. Lee, H.-H. Park, R. H. Hill, J.-H. Jeong, *J. Mater. Chem.* **2010**, *20*, 1921.

[28] T. Bottein, O. Dalstein, M. Putero, A. Cattoni, M. Faustini, M. Abbarchi, D. Grosso, *Nanoscale* **2018**, *10*, 1420.
[29] J. van de Groep, P. Spinelli, A. Polman, *Nano Lett.* **2015**, *15*, 4223.
[30] I. Navarro-Baena, A. Jacobo-Martín, J. J. Hernández, J. R. Castro Smirnov, F. Viela, M. A. Monclús, M. R. Osorio, J. M. Molina-Aldareguia, I. Rodríguez, *Nanoscale* **2018**, *10*, 15496.
[31] Nanoimprint Lithography on Silica Sol–Gels: A Simple Route to Sequential Patterning, .
[32] C. Boissiere, D. Grosso, S. Lepoutre, L. Nicole, A. B. Bruneau, C. Sanchez, *Langmuir* **2005**, *21*, 12362.
[33] D. Grosso, C. Boissière, C. Sanchez, *Nat. Mater.* **2007**, *6*, 572.
[34] H. Deniz, T. Khudiyev, F. Buyukserin, M. Bayindir, *Appl. Phys. Lett.* **2011**, *99*, 183107.
[35] S.-H. Hong, B.-J. Bae, K.-S. Han, E.-J. Hong, H. Lee, K.-W. Choi, *Electron. Mater. Lett.* **2009**, *5*, 39.
[36] D. Berman, S. Guha, B. Lee, J. W. Elam, S. B. Darling, E. V. Shevchenko, *ACS Nano* **2017**, *11*, 2521.
[37] Y. J. Yoo, Y. J. Kim, S.-Y. Kim, J. H. Lee, K. Kim, J. H. Ko, J. W. Lee, B. H. Lee, Y. M. Song, *Opt. Mater. Express* **2019**, *9*, 4178.
[38] G. Womack, K. Isbilir, F. Lisco, G. Durand, A. Taylor, J. M. Walls, *Surf. Coat. Technol.* **2019**, *358*, 76.
[39] S. B. Khan, H. Wu, Z. Xie, W. Wang, Z. Zhang, *ACS Appl. Mater. Interfaces* **2017**, *9*, 36327.
[40] C. J. Brinker, In *Chemical Solution Deposition of Functional Oxide Thin Films* (Eds.: Schneller, T.; Waser, R.; Kosec, M.; Payne, D.), Springer Vienna, Vienna, **2013**, pp. 233–261.
[41] E. Tatsi, G. Griffini, *Sol. Energy Mater. Sol. Cells* **2019**, *196*, 43.

# CHAPTER 3: SOL-GEL $TiO_2$ NANOIMPRINTED METASURFACE COMBINED TO HYBRID-SILICA SENSITIVE LAYERS WITH HIGH REFRACTIVE INDEX SENSITIVITY AND SELECTIVITY FOR GAS SENSING

This chapter focuses on the elaboration of nanocomposite systems with high sensitivity for refractive index (RI) variation and high selectivity for Volatile Organic Compounds (VOC) detection. Detection of vapor compounds has been an important domain of research owing to the specific needs of chemical detectors in industrial and medical activities. The social and economic needs push towards the development of cost-effective, simple and portable devices that can also solve issues related to chemical selectivity. Hence, in this chapter, we illustrate a novel nanocomposite system combining all-dielectric sensitive materials based on metal oxides deposited via sol-gel and framed in 3D structures via Nano Imprint Lithography (NIL). This system shows relatively sharp resonances featuring a large spectral shift against refractive index changes. The metasurface is composed of $TiO_2$ framed in high vertical aspect ratio nanopillars, whereas the surrounding sensitive materials are hybrid silica microporous materials bearing various types of covalently bonded organic functions. These hybrid layers show marked relative differences in chemical affinity with different VOCs and can be exploited to detect them while eliminating interferences with air moisture for qualitative analysis of gas mixtures. The presence of the $TiO_2$ metasurface enhances the signal by almost an order of magnitude with respect to the 2D counterpart and is attributed to the antenna effect, enhancing the interaction of the confined electromagnetic wave with the sensitive medium. This sol-gel nanocomposite system presents many advantages such as high throughput and low-cost elaboration of the elements, high chemical, mechanical and thermal stability, ensuring their exploitability for detection over long periods.

# 1. Introduction

Refractive Index (RI) sensitive materials are critical elements for environmental analysis through optical transduction in chemical, biological, and physical sensors. They rely on variations of electromagnetic confinement in metals (Localized Surface Plasmonic Resonances, LSPR) or dielectrics (Fabry-Perot interferences, dielectric Mie resonances) upon small changes of RI in the confinement volume of the electromagnetic waves[1,2]. The size and geometry of micro and nanostructures are thus designed to enhance the electromagnetic resonances in the regions where the RI changes. In chemical sensing, such a variation is induced at the surface or inside the material (if porous) through the modification of the chemical environment triggered by the combination of a target molecule with a specific host chemical group or simply by adsorption[3]. Gas sensors are a category of detectors that suffers from a high competitivity of adsorption between the molecules composing the air. For instance, VOCs are more or less toxic molecules produced by different human activities or nature. There are many of them and they cohabit in the air at low concentrations (*e.g.* ppm levels)[4] with water that is the most critical interferent due to its high concentration. These small molecules tend to interact easily with surfaces, rendering them easy to quantify as this phenomenon is governed by thermodynamic equilibrium. However, designing a sensor that is selective to one VOC is extremely challenging[4].

Chemical sensors based on optical transduction through RI variations rely on measuring either wavelength shifts or intensity variations (Reflectance $R$, Transmittance $T$, or Scattering $S$). Many different metasurfaces or metamaterials have been designed and studied to enhance the optical signal and increase their performances generally based on the detection of a sharp resonance that shifts upon RI changes. Sensitivity $S$ ($S = \Delta\lambda/\Delta n$) and Figure of Merit $FOM$ ($FOM = S/FWHM$ with $FWHM$ being the Full Width at Half Maximum of the resonance) are indicators of performance considering both resonance sharpness and wavelength shift upon RI change. Alternatively, detection can be based on $R$, $S$, or $T$ intensity variation that are usually compared through the "alternative" Figure of Merit $R^*$ ($R^* = (\Delta I/I)/\Delta n$) given as *R, S, or T /* Refractive Index Unit (RIU). Due to their relatively sharp LSPR and narrow wavelength-shift, gold or silver nanostructures (core-shell) nanoparticles[5], pillars[6], disks[7], rods[8], pyramids[9], stars, etc., are the most attractive metasurfaces for RI sensing. Sensitivity up to $2\times10^3$ nm / RIU, with a $FOM$ of 100[6], has been experimentally evidenced with gold nanopillars, while simulations with gold nanoshell systems revealed a potential sensitivity of $3\times10^3$ with a $FOM$ around 10[10]. More recently, dielectric (Si, Ge, Metal oxides, $MO_n$) nanostructures have been considered as alternative RI-sensitive materials due to their low toxicity, low cost, and fabrication easiness. Interestingly, the possibility to select the intrinsic RI of some dielectrics, such as $MO_n$, enables optimizing sensing within specific RI spans. The electromagnetic confinement in dielectric nano-objects leads to a strong modification of $R$, $T$ and $S$ intensity and can be highly sensitive to the surrounding RI[2,11].

The first examples combined dielectrics and metals[12,13] in complex architectures. For instance, *FOM* values up to $6.7\times10^3$ are deduced from simulations with $Au/SiO_2$-$Al_2O_3$ pillar systems[14]. Finally, $Al/Al_2O_3$ ring systems provided an experimental *FOM* of 6 for $\delta n = 0.6$[13]. For pure dielectric systems, *R** of 6 was experimentally demonstrated for SiGeTe nanospheres[11] whereas the highest value simulated for metal oxide (*e.g.,* $V_2O_5$, $TiO_2$) patterns reaches 13[15]. The following Table 3-1 reports state-of-the-art *FOM*, *R**, *Q*-factors, and sensitivity for these classes of materials[16–20]. It reveals that high performances are achieved with complex metals or semiconductor (SC) architectures, while the more attractive ones have only been modeled without experimental corroborations.

Table 3-1. Comparison of state-of-the-art sensitivities, *FOM*, R*, and Q-factors of different refractive index-based sensors from the literature with those reported in this current work (Exp. and Sim. stand for experimental and simulated values, respectively).

| Materials | *S* nm/RIU | *FOM* | *S*,*T*,*R* / RIU | *Q*-factor | References |
|---|---|---|---|---|---|
| **Metals (Au, Al)** | Exp: up to $10^3$<br>*Sim.: up to 3.10³* | Exp: 10 to 110<br>- | -<br>- | - | [6,7,10,12,21–23] |
| **SC (Si, Ge, Te)** | Exp: 200 to 920<br>*Sim.: 350 to 2.10³* | Exp: 2 to 120<br>*Sim.: 80 to 2.10³* | Exp: 4 to 9<br>- | Exp: up to $10^3$<br>*Sim: up to 10⁵* | [2,16,18,19,24] |
| **Metal/$MO_n$** | Exp: up to $10^3$<br>*Sim.: up to 2.10³* | Exp: 6<br>*Sim.: 500 to 6.10³* | -<br>- | Exp: 26-27<br>- | [14,23,25] |
| **$MO_n$($V_2O_5$, $TiO_2$)** | *Sim.: 10 to 800* | *Sim.: 732* | *Sim.: 13* | - | [15,26] |
| *$TiO_2$* | ***Exp: 4500*** | ***Exp: 12*** | ***Exp: 17*** | ***Exp: 4*** | ***This work*** |

Detecting gas by optical transduction often requires a porous sensitive material with the inner pore surface is covered with a chemical group that has a good affinity with the target molecules. These materials need to be highly porous, with a high specific surface area (micro- or mesopores with high accessibility), robust and stable, easy to process as optical elements[27–29]. Among them, sol-gel-based materials gather these features providing an excellent versatility to tune porosity, chemical composition, and RI as thin coatings [30].

Silica-based layers have been exploited in this work as sensitive materials with a refractive index around $RI_0 \sim 1.5$. Since VOCs need to be detected at 0-100 ppm levels through adsorption, the porosity needs to be adapted so that the sensitivity is maximal, and ideally with a linear dependence on concentration, for extremely small RI increases from $RI_0$ ($RI_0$ correspond to the initial thin film RI) of the desorbed material. As such, microporous materials with pore dimensions of < 2 nm are ideal since they exhibit a high specific surface area (high density of adsorption sites) enabling high adsorption at low relative vapor pressures ($P/P_0$). Such pores can be further chemically adapted to tune the adsorption affinity with specific types of VOC molecules exhibiting different polarity indexes. Owing to the small size of VOC, forbidding an individual molecular identification, it is thus only possible to modulate the chemical affinity during adsorption by changing

the polarity of the pore surface with organic functions that exhibit more or less polar characteristics[30–32]. Such materials are elaborated as thin films using simple high throughput chemical liquid deposition processes such as dip-coating[33]. They require further thermal curing, typically around 400 °C to stabilize the inorganic backbone, but this treatment should be adapted to prevent the decomposition of the organic function.

In this chapter we show that the combination of all-dielectric metal oxides sensitive materials and metasurfaces, all prepared by simple high throughput sol-gel methods, can lead to relatively high sensitivity (1 ppm) and relatively good chemical selectivity for VOC sensing, using simple reflectivity transduction at visible frequency. The metasurface is composed of $TiO_2$ (Anatase) nanopillars and is obtained by NIL technique[34–36] and organized in a 2D hexagonal pattern on a Si wafer. It is then capped by microporous Hybrid Silica (H-$SiO_2$) layer. The reflectivity of the layer has then been measured in the visible range with increasing vapor pressure. The measured sensing performances are sensitivity *S* up to 4500 nm/RIU (0.2 nm/ppm), reflection intensity changes up to R* = 17 ($0.55\times10^{-3}$ R/ppm), *FOM* up to 12, with a *Q*-Factor of 4 for a specific wavelength, which is compatible with sub-ppm gas detection by simple specular reflection. These performances have been compared to the theoretical responses of the corresponding Bruggeman Effective Medium Approximation (BEMA) model of the system, revealing the critical role of the pillar in exalting the signal. Structural characterizations and spectroscopy were performed by Fourier Transform infrared spectroscopy (FTIR), Scanning Electron Microscopy (SEM), Atomic Force Microscopy (AFM), X-Ray Diffraction (XRD), and ellipsometry (See appendix 2).

# 2. Experimental section

## 2.1. Preparation of hybrid-silica (H-$SiO_2$) sensitive plain coatings

Sol-gel initial solution was prepared from 0.3 TetraEthylOrthoSilicate (TEOS) and hybrid silanes precursors (0.3 Methyltriethoxysilane, 0.3 Phenyltriethoxysilane) dissolved in a mixture of 25 isopropanol: 11 water: 3 hydrochloric acid (molar ratio). The solution was aged one day at room temperature before using for film deposition (shelf-life between 2 and 10 weeks). The deposition was performed by dip-coating using an ACE-dip from Solgelway on the silicon wafer. Silicon wafer substrate was first cleaned with detergent, acetone, and ethanol in an ultra-sound bath. Then, dip coating using the withdrawal speed of 2 $mm.s^{-1}$ at low humidity (< 10%) was applied to adjust the final thickness of 480 nm. The as-prepared coating was then calcined at 400 °C for 10 min. The final refractive index was obtained and measured by ellipsometry at about n = 1.457. Methyltriethoxysilane leads the microporous hybrid silica as a hydrophobic thin film. Indeed, the silica layer has been elaborated with different organic contents and tested as adsorbents with common VOC, such as isopropanol, acetone, chloroform, hexane, toluene, and water as adsorbates. Therefore, this silica hybrid layer has been selected and combined with a $TiO_2$ metasurface to prepare a nanostructured composite sensitive system. The preparation of $TiO_2$ nanostructured composite embedded with Silica hybrid film will be described in 2.3.

## 2.2. Investigation of gas adsorption in the plain sensitive layer

First, the plain layer of sensitive H-$SiO_2$ material was tested in different VOC vapor environments at 0% humidity to avoid perturbation due to adsorbed water. The refractive index variations (δn) were measured using spectroscopic ellipsometry. Figure 3-1 provides the adsorption isotherm of isopropanol in the H-$SiO_2$ sensitive layer, confirming the typical Langmuir behavior for microporous materials, following equation (1) for which the fit parameters were found to be $\delta_{n\,max}$ = 0.044 and the affinity constant $b$ = 22. Using $P_{IPrOHsat}$ = 2 kPa, one can then deduce equation (2) that links the measured $\delta_n$ to the concentration in ppm of adsorbate in the environment. To detect 2 ppm of IPrOH in the air at 1 Atm and 20 °C, one needs to be able to detect a $\delta_n = 10^{-4}$. The Langmuir adsorption isotherm is used to describe the equilibrium between the adsorbate and adsorbent system, where the adsorbate adsorption is limited to one molecular layer at or before a relative pressure of unity is reached. Although the isotherm initially proposed by Langmuir in 1918 is generally suitable for describing the chemisorption process when ionic or covalent

chemical bonds are formed between the adsorbent and the adsorbate[37]. The variation of RI of the H-$SiO_2$ sensitive coatings with respect to gas adsorption was followed by *in-situ* using an environmental chamber. The gas was selected to be IPrOH for its high volatility and its good affinity with the layer. Its relative pressure ($P/P_0$) was adjusted using an air-dilator system, mixing both IPrOH saturated and pure air.

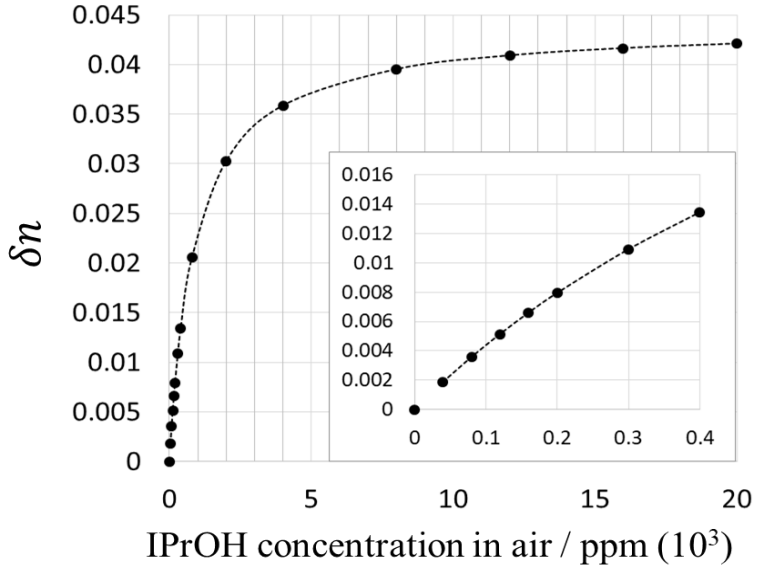



Figure 3-1. Adsorption isotherm of isopropanol in H-$SiO_2$ sensitive plain layer, plotted as δn, measured by spectroscopic ellipsometry, vs. IPrOH concentration.

$$\delta n = \delta n_{max} \frac{b\left(P/P_0\right)}{\left(1+b\left(P/P_0\right)\right)} \quad (1)$$

$$C_{IPrOH} = \frac{10^6 \, P_{IPrOHsat} \, \delta n}{P_{Atm} \, (0{,}97 - 22 \, \delta n)} \quad (2)$$

Moreover, based on FTIR measurement, the affinity bond of the hybrid silica is compared with the $SiO_2$ reference film which contains 1TEOS dissolved in a mixture of 25 isopropanol: 11 water: 3 hydrochloric acid (molar ratio). According to Figure 3-2 a), it is clear that, even if the hybrid silica-sensitive layer is calcined at 400 °C, it still embeds the methyl and the aromatic functions introduced as precursors. Thereby, it should be accessible as an adsorption site to the VOC adsorbates through the porosity and must play a crucial role in the chemical affinity difference. To go further, when testing the $SiO_2$ reference and the hybrid $SiO_2$ layer with five different VOCs at a concentration of 600 ppm and with 100% humidity (saturation), it was observed that the H-$SiO_2$ pair presents a specific affinity that is due to the difference in the layer chemical and porosity characteristics and the VOC index of polarity (see Figure 3-2 b)).

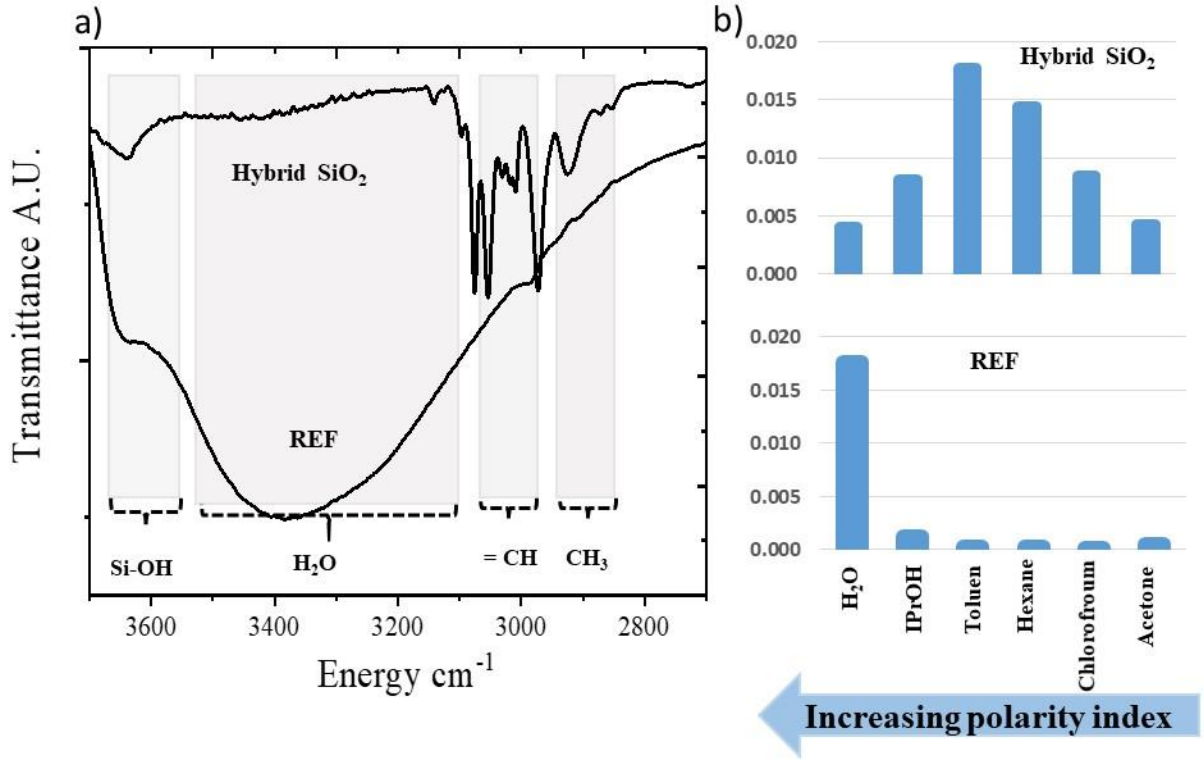



Figure 3-2. a) FTIR spectra of sensitive layer showing regions of C-H stretching from methyl and aromatic functions, and regions of O-H stretching from water (High Density (liq.); Low Density (sol.)), and silanol. b) Comparison of chemical affinity measured on a set of sensitive layer adsorbent / VOC adsorbate pairs when submitted to 600 ppm of VOC or to 100% humidity ($10^3$ δn).

As expected, the REF layer mainly adsorbs water since it contains no organics, but only highly polar Si-OH groups on the pore walls. Such reference layer acts thus as a water-selective sensitive layer, that is used to assess humidity between 0 and 100%. Indeed, the H-$SiO_2$ layer is more prone to interact with VOCs, since its adsorption of water at 100% RH is much lower than the adsorption of VOCs at 600 ppm. It has been demonstrated that when methyl groups are attached to a Si-O-Si backbone, they tend to position at the interface with the pore nanocavities upon thermal annealing without decomposing due to the stability of the Si-C bond below 450 °C in the air[38]. Importantly, competitive adsorptions of VOCs in the H-$SiO_2$ layer must be as low as possible, especially with water. When two of the selected vapors are injected in the chamber at the same time, such as IPrOH and water, they must not interfere, at least at low pressures. This has been confirmed in Figure 3-3 that shows the evolution of the H-$SiO_2$ layer when exposed successively to 100, 220, and 350 ppm of isopropanol, together with 0, 30, 60, and 90% of relative humidity.

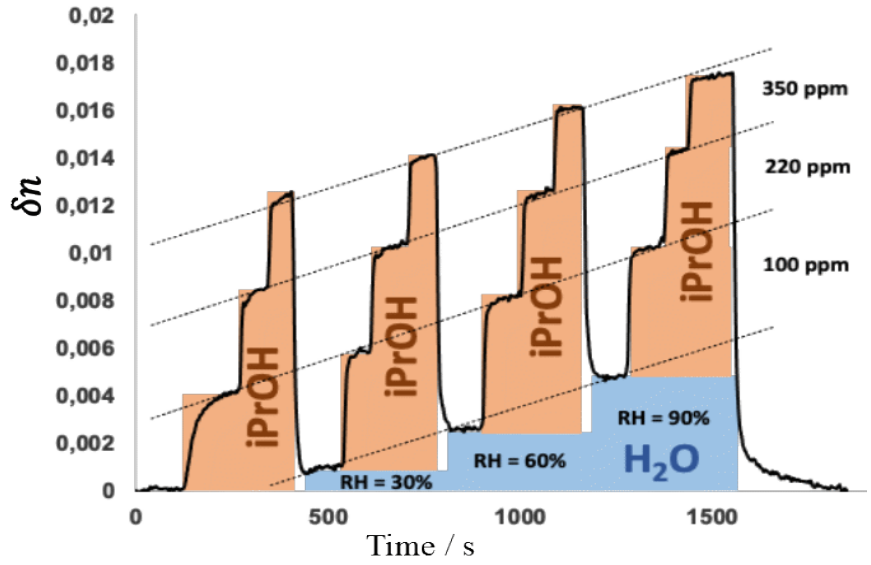



Figure 3-3. Variation of measured by ellipsometry on the H-$SiO_2$ plain sensitive layer when submitted to 100, 220 and 350 ppm of isopropanol and 0, 30, 60, and 90 % humidity.

## 2.3. Preparation of H-$SiO_2$/$TiO_2$ nanostructured composite system by environmental control T-NIL

The preparation of the $TiO_2$ nanostructured composite system was based on environmental control T-NIL using Perfluoropolyether (PFPE) stamp. The PFPE mold was obtained as inverse mold from the commercial perfluoropolyether Fluorolink (MD700) master (same master as in chapter 2). To do so, a few droplets of PFPE precursors were applied to the center of the master and spread homogenously using a solid roller. The mold was peeled off from the master after 10 min of curing under nitrogen and ultra-violet LED (365 nm, 4 W). The mold was then degassed for 15 min in a primary vacuum. For preparing the $TiO_2$ pillars, First, titania solution was prepared by mixing molar ratios of 1 $TiCl_4$: 40 EtOH: 7 $H_2O$: $4.10^{-5}$ F127 (Pluronics F127: PEO-PPO-PEO) all purchased from Aldrich. After 24 h aging at room temperature, the solution was dip-coated on Si wafer at 2 $mm.s^{-1}$ withdrawal speed under relative humidity HR < 10%. The as-prepared film was either used directly for nanoimprint or calcined at 450 °C for 10 min to yield a final thickness of 75 nm and a RI of n = 2.252 at 633 nm.

Second, As-prepared titania sol-gel film was directly transferred from the dip-coater into a nanoimprint chamber in which a 22 °C temperature and a 50% relative humidity were maintained using a constant 5 $L.min^{-1}$ flux from a Solgelway humidity controller[34]. The degassed PFPE mold was applied onto the sol-gel film under the 50% HR and then maintained at 60 °C for 15 min before demolding. Third, the imprinted sol-gel patterns were annealed at 450 °C for 10 min to ensure complete removal of the F127 polymer and crystallization. Then, the 2D microporous hybrid silica layer was coated on top of the $TiO_2$ 3D patterns by dip-coating at room temperature using 4 $mm.s^{-1}$. Thereby, the final nanostructured composite coating was annealed at 400 °C for 10 min for stiffening. Figure 3-4 a, b, and c) shows the SEM images of the nanostructured composite coating, revealing the array of $TiO_2$ pillars homogeneously organized in a 2D hexagonal pattern. The pillar aspect ratio is ~ 2 with 270 nm height and 140 nm width. A residual layer of about 10 to 20 nm thickness was spotted all over the wafer. Moreover, as revealed by AFM analysis, $TiO_2$ pillars were covered completely by sensitive microporous H-$SiO_2$ thin film, with a plain layer of 190 nm thick and the roughness (RMS) of about ~ 0.8 nm (see Figure 3-4 d)).

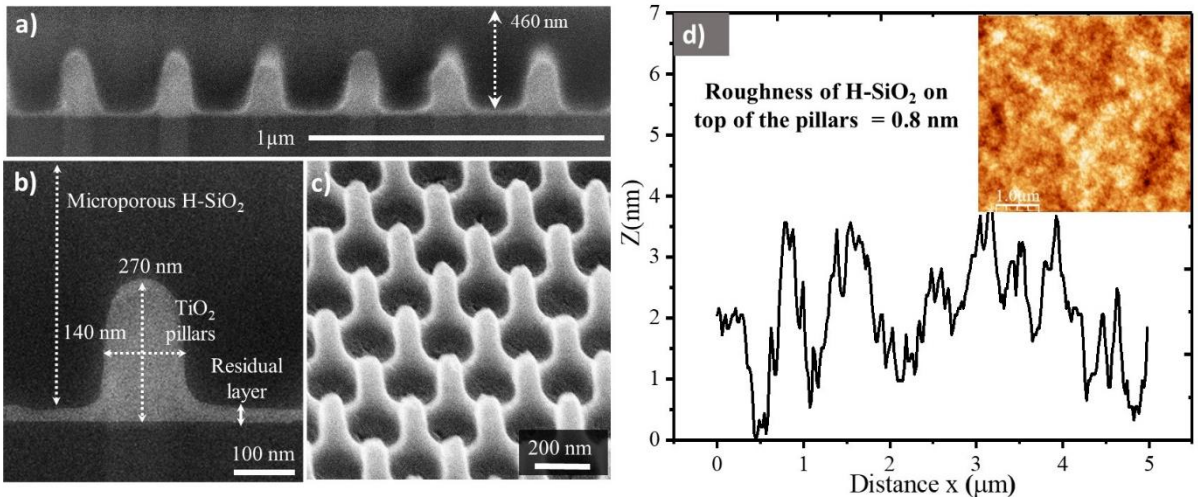



Figure 3-4. SEM images of a) and b) H-$SiO_2$ / $TiO_2$ nanostructured composite, and c) of $TiO_2$ nanostructured metasurface. d) AFM image of H-$SiO_2$ on top of the pillars shows the roughness of this coated film.

XRD investigation (Figure 3-5) shows that the $TiO_2$ plain layer and pillar array was composed of tetragonal anatase titania with the characteristics 101, 004, 200, 105, and 211 diffraction peaks of poly-oriented crystal. Both diagrams show very similar peak features, width (FWHM), and intensity, suggesting that the nanoimprinting does not change significantly the overall structuration induced by the thermal annealing. Fitting the diffraction peaks allows deducing FWHM which is inversely related to the crystal size (along the direction of the scattering vector *e.g*. the direction normal to the film, and neglecting micro strain contributions). Using the Scherrer formula we estimate a nanocrystals size of about 16±1 nm for the plain layer and 18 ± 4 nm for the pillars. This is an important statement since the refractive index of the pillars, used in the BEMA model

(see Figure 3-6), is extracted from the ellipsometry analysis of the plain layer. The fact that the anatase crystals have a similar average dimension around 20 nm suggests that RI are significantly close in both geometries.

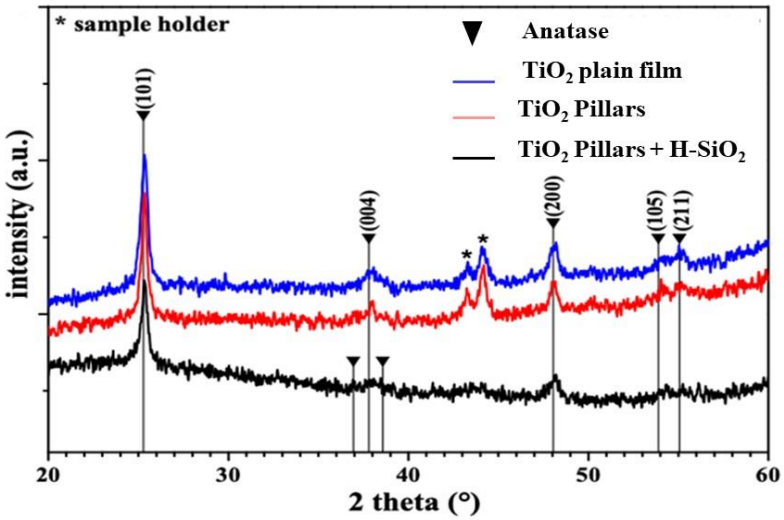



Figure 3-5. XRD patterns of the $TiO_2$ plain layer, the array of $TiO_2$ pillars, and the H-$SiO_2$ / $TiO_2$ nanostructured composite.

A simple geometrical calculation based on the pillar dimensions and distribution (assuming a cylindrical shape) provides a composite thickness of 20% Vol $TiO_2$ and 80% Vol H-$SiO_2$. This geometrical calculation is known as the BEMA. Refractive indices of $TiO_2$ and H-$SiO_2$ materials measured by ellipsometry on plain layers are 2.252 and 1.457 at 633 nm in dry air, respectively (see Figure 3-6).

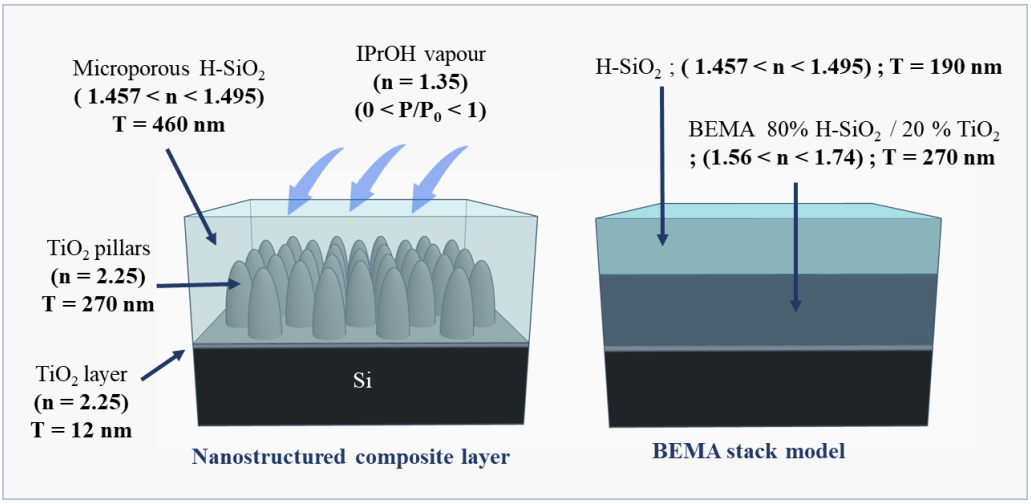



Figure 3-6. Scheme representing the experimental nanostructured composite system (experimental) and the corresponding Bruggeman Effective Medium Approximation (BEMA) multilayer stack system (model) used as sensitive coatings for RI variation and VOC concentration detection. The variation of RI is induced by the controlled adsorption of isopropanol into the H-$SiO_2$ material (layer).

# 3. Specular reflection of nanostructured sensitive layer composite systems

While ellipsometry has been used in the previous part to assess RI variations, the following part will focus on a simpler method based on specular reflectivity to assess VOC concentration in the atmosphere (see appendix 2). To do so, only one adsorbate/adsorbent pair will be used to investigate performance in sensitivity, since the transduction exploits RI variations. Experiments were conducted on a sensitive coating composed of a high index $TiO_2$ metasurface, elaborated on Si wafer, and embedded into a layer of the H-$SiO_2$ material. The role of the metasurface is to confine the visible electromagnetic radiations inside the high index nanofeatures to enhance their interaction with the surrounding sensitive material. The incident and collection angles were fixed at 45° as this configuration provided a good penetration of the polarized light into the nanostructure coating (Brewster angle 55°) while collecting high enough reflected intensity. To assess the effective influence of the metasurface, the experimental reflectance was then compared to the simulated reflectance of a corresponding 3-layer stacks coating for which the nanostructured composite thickness of the experimental sample was replaced by BEMA layer (see Figure 3-6).

As studied in the first part, the refractive index of the sensitive layer increases with a vapor pressure of isopropanol being introduced into the chamber, following a classical adsorption/desorption equilibrium behavior in microporous materials (Figure 3-1). The vapor uptake is very large at a low-pressure, going from 1.4570 to 1.4696 ± $10^{-4}$ (RI) between $P/P_0$ = 0 and 0.02. In the following investigations, only this range will be explored since for gas detection, sensitivity at low concentrations must be as high as possible (*e.g.* $P/P_0$ = 0.02 corresponds to 850 ppm in IPrOH at 20 °C). The variation of the titania refractive index for the same vapor pressure is insignificant[39]. As for the pure titania system, the RI of the sensitive material in the nanostructured composite system cannot be measured and is thus assumed to be that one of the plain layer counterparts. Specular reflectivity spectra for the nanostructured composite system between $P/P_0$ = 0 and $P/P_0$ = 0.02 ($n_{H\text{-}SiO2}$ = 1.4570 and 1.4696, respectively) are plotted in Figure 3-7 a). These are compared to the simulated reflection spectra of the corresponding theoretical BEMA system calculated for the same increments, in Figure 3-7 b). Both show a typical etalon interference trend that is relatively similar, especially at a long wavelength. The lower intensity of the specular reflectance of the experimental signal at a short wavelength (see Figure 3-7 c)) is likely due to the scattering effect of the pillars which is not detected in this experiment. This effect is less relevant in the red part of the spectrum where the pillar size and spacing are negligible with respect to the wavelength and the BEMA approximation is more precise. While the BEMA spectra undergo a global redshift of 6 nm around 670 nm, attributed to the H-$SiO_2$ RI increase of 0.0126, a redshift of around 60 nm for the same interference is observed for the nanostructured system for the same increment. The corresponding *Q*-factor is 4 at (λ = 675 nm) for both systems. This

difference is attributed to the $TiO_2$ metasurface antenna effect. Figure 3-7 d) shows the plot of the wavelength of the interference maxima versus RI for the nanostructured system. A linear RI sensitivity of around 4500 nm/RIU is found up to RI = 1.463, which is extremely high and corresponds to a sensitivity of 0.2 nm/ppm of IPrOH vapor in the atmosphere. The corresponding *FOM* is ~ 12. Such a good sensitivity corresponds to the H-$SiO_2$ /IPrOH pair.

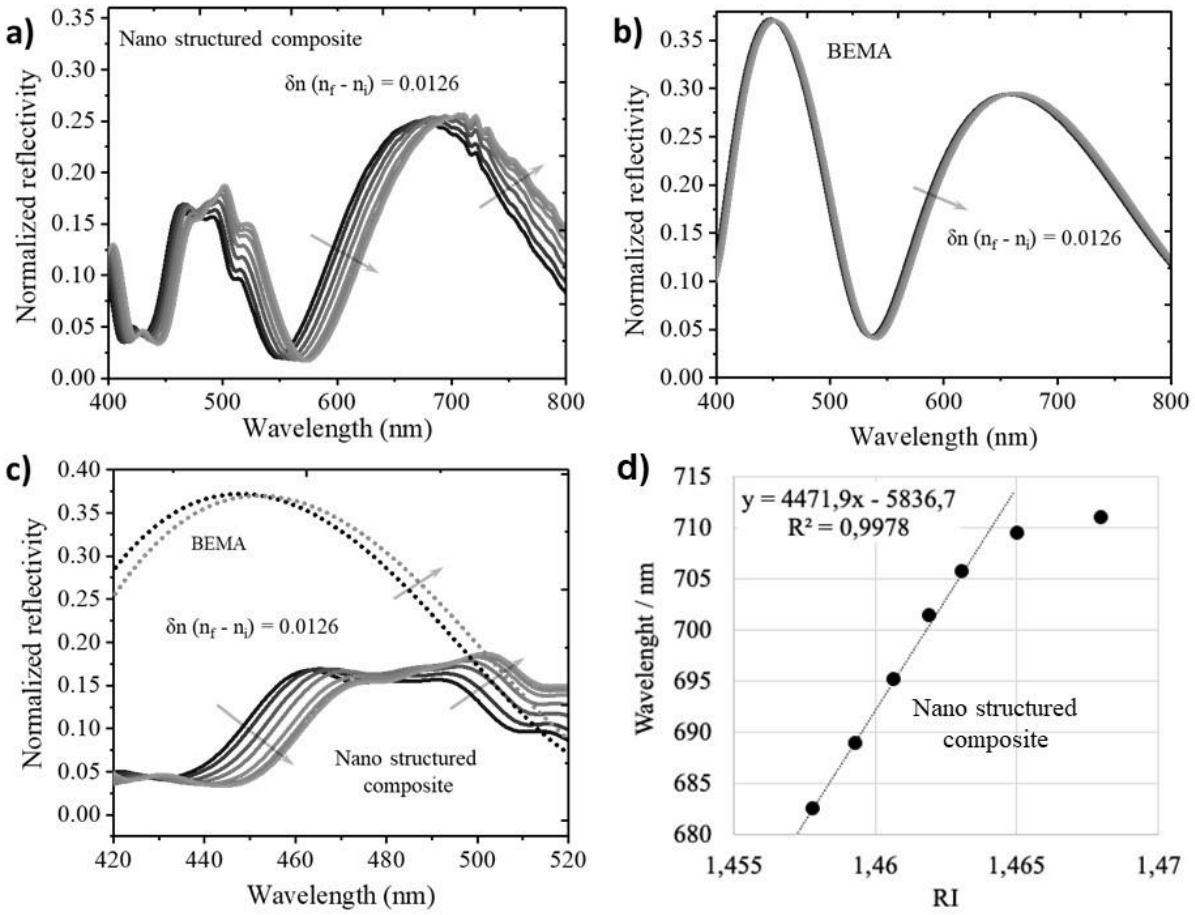



Figure 3-7. Reflectivity spectra measured at 45° incidence for the H-$SiO_2$/$TiO_2$ nanostructured composite, a) and c), and simulated for the corresponding BEMA model, b) and c), for different increments of between 1.4570 and 1.4696 d) vs. RI (sensitivity) extracted from a).

Using optical transduction through spectral shift requires a spectral analysis of the signal. More conveniently, RI variation detection can also be performed at a single wavelength using the reflected intensity collected by a photodiode[40]. In such simplified methods, the sensitivity is provided by the *R** (equation (3)) for a given wavelength, and a given RI span.

$$\boldsymbol{R^*_{(\lambda,n_i,\delta n)}} = \frac{\left(\boldsymbol{R_{\lambda,(n_i+\delta n)}} - \boldsymbol{R_{\lambda,n_i}}\right)}{\boldsymbol{\delta n}} \qquad (\mathbf{3})$$

The dispersion of $R^*$ has been determined for both the experimental and simulated reflectivity variation for different incremental $n$ and different initial RI comprised between 1.4570 and 1.4665. Figure 3-8 provides different plots of the results.

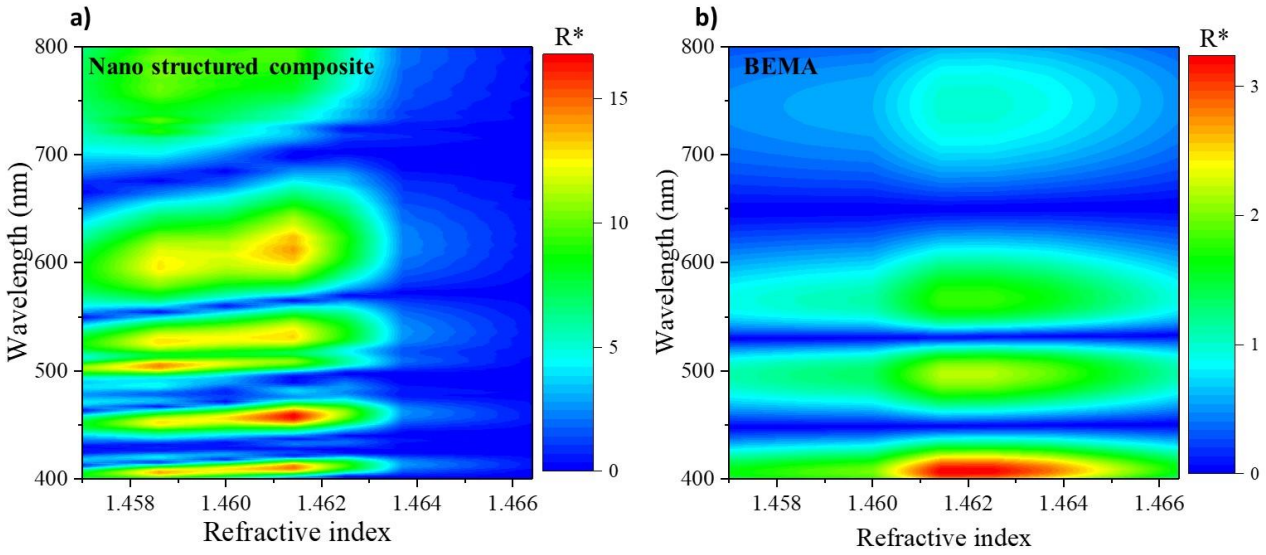



Figure 3-8. a) and b) 2D mapping of R* dispersion values for different RI measured for the H-$SiO_2$/$TiO_2$ nanostructured composite system and simulated for the BEMA system, respectively.

For the BEMA model, for which the nano-structuration of the H-$SiO_2$/$TiO_2$ composite layer is not considered, $R^*$ has an absolute maximum value between 1.5 and 3, resulting from the local reflected intensity variation induced by the red-shift of the interference fringes. In the same conditions, $R^*$ for the nanocomposite can take values from 8 to 17, which is almost one order of magnitude higher than that of the BEMA model. This mapping reveals that $R^*$ can take values with drastic differences depending on the wavelength, but also on the initial RI ($n_i$). Thus, in order to maximize the response, we select a wavelength of 408 nm for the BEMA model, and at 450 nm for the nanostructured system (in principle, narrow-band illumination at about 450 nm can be provided with blue LEDs or with lasers). We now compare the maximal reflectance sensitivity provided in Figure 3-8 a) and b) (see Figure 3-9 a) and b)). The highest $R^*$ = 17 nm/RIU is found at 450 nm for $n_i$ = 1.4607 and $n_f$ = 1.4619. It drops to 8 between $n_i$ = 1.4562 and $n_f$ = 1.4578. This suggests that if the analysis is to be performed at a specific wavelength such as 450 nm of a blue LED, the variation of $R^*$ has to be implemented in the signal treatment for the whole RI detection span through a careful calibration.

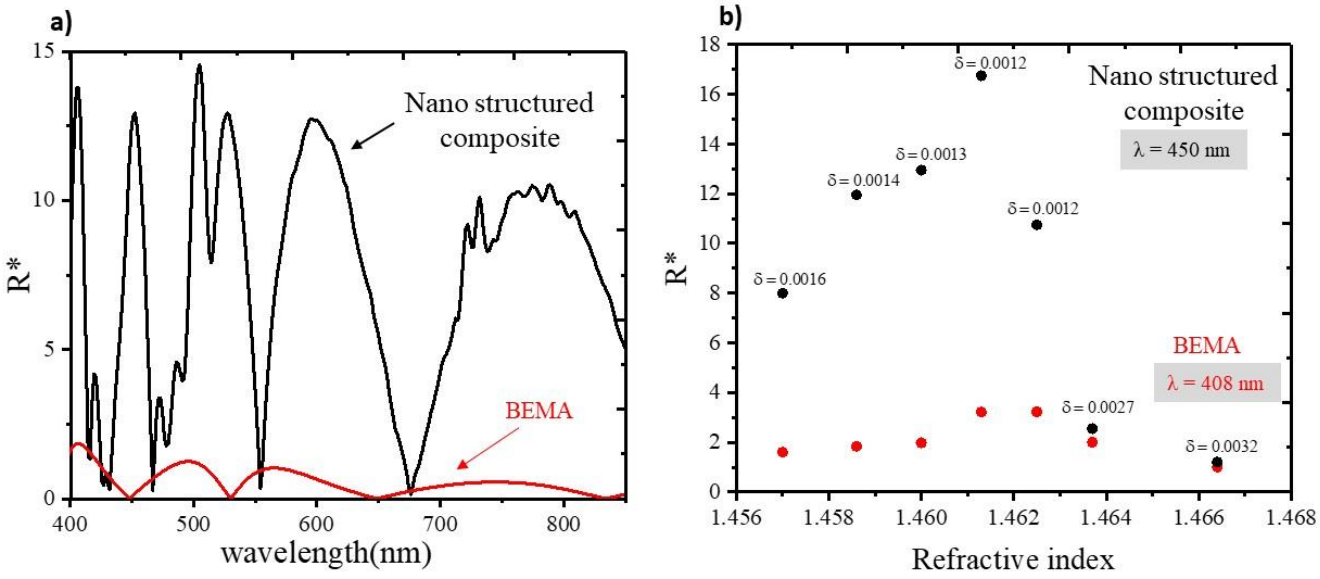



Figure 3-9. a) and b) R* dispersion and values extracted from Figure 3-8 a) and b) for both systems at an optimal wavelength of 450 and 408 nm.

# 4. Conclusion

We reported that the presence of a dielectric metasurface ($TiO_2$ pillar arrays) can significantly increase the sensitivity to RI variations in the surrounding medium in direct reflection up to 4500 nm/RIU. However, such high sensitivity can only be found in narrow conditions including wavelength, incident angle, RI, and RI span. The metasurface has also been combined with microporous sol-gel layers to detect VOC by adsorption. Optimal sub-ppm sensitivity of 0.2 nm/ppm (spectral shift) and $0.55\times10^{-3}$ R / ppm (single wavelength reflectivity) were demonstrated. Even if Q-factor and *FOM* were relatively low, the sensitivities were sensibly higher than those reported for plasmon-based systems and those simulated for pure metal oxide metasurfaces (see Table 3-1). We also showed that robust and stable silica-based hybrid layers composed of different pendant organic moieties on the inorganic backbone have a different chemical affinity with different VOC. The combination of $TiO_2$ metasurface and sol-gel sensitive materials provides good sensitivity and selectivity that constitutes critical transduction elements to design and elaborate a cost-effective "artificial nose" for VOC sensing. The present performances were not optimized exploiting simulations and could be further improved by designing a more appropriate metasurface.

# 5. References


[1] J. Becker, A. Trügler, A. Jakab, U. Hohenester, C. Sönnichsen, **2010**, 7.

[2] J. Yan, P. Liu, Z. Lin, G. Yang, *Nanoscale* **2016**, *8*, 5996.

[3] Y. Jian, W. Hu, Z. Zhao, P. Cheng, H. Haick, M. Yao, W. Wu, *Nano-Micro Lett.* **2020**, *12*, 71.

[4] B. Szulczyński, J. Gębicki, *Environments* **2017**, *4*, 21.

[5] Y. Sun, Y. Xia, *Anal. Chem.* **2002**, *74*, 5297.

[6] Y. Shen, J. Zhou, T. Liu, Y. Tao, R. Jiang, M. Liu, G. Xiao, J. Zhu, Z.-K. Zhou, X. Wang, C. Jin, J. Wang, *Nat. Commun.* **2013**, *4*, 2381.

[7] M. Couture, T. Brulé, S. Laing, W. Cui, M. Sarkar, B. Charron, K. Faulds, W. Peng, M. Canva, J.-F. Masson, *Small* **2017**, *13*, 1700908.

[8] M. G. Scullion, A. Di Falco, T. F. Krauss, *Biosens. Bioelectron.* **2011**, *27*, 101.

[9] C. L. Nehl, H. Liao, J. H. Hafner, *Nano Lett.* **2006**, *6*, 683.

[10] I. M. Pryce, Y. A. Kelaita, K. Aydin, H. A. Atwater, *ACS Nano* **2011**, *5*, 8167.

[11] C. Ma, Y. Liu, F. Zhao, F. Xu, J. Yan, X. Li, B.-O. Guan, G. Yang, K. Chen, *J. Mater. Chem. C* **2020**, *8*, 6350.

[12] H. Ni, M. Wang, T. Shen, J. Zhou, *ACS Nano* **2015**, *9*, 1913.

[13] A. Ahmadivand, S. Golmohammadi, *Opt. Laser Technol.* **2015**, *66*, 9.

[14] Y.-L. Liao, Y. Zhao, *Results Phys.* **2020**, *17*, 103072.

[15] Z. Ren, Z. Lin, X. Zhi, M. Li, *Opt. Mater.* **2020**, *99*, 109575.

[16] K. S. Modi, J. Kaur, S. P. Singh, U. Tiwari, R. K. Sinha, *Opt. Commun.* **2020**, 7.

[17] D. U. Yildirim, A. Ghobadi, M. C. Soydan, M. Gokbayrak, A. Toprak, B. Butun, E. Ozbay, *J Phys Chem C* **2019**, 10.

[18] A. J. Ollanik, I. O. Oguntoye, G. Z. Hartfield, M. D. Escarra, *Adv. Mater. Technol.* **2018**, 1800567.

[19] C. Zhang, Y. Song, M. Wang, M. Yin, X. Zhu, L. Tian, H. Wang, X. Chen, Z. Fan, L. Lu, D. Li, *Adv. Funct. Mater.* **2017**, *27*, 1604720.

[20] L. Xie, W. Gao, J. Shu, Y. Ying, J. Kono, *Sci. Rep.* **2015**, *5*, 8671.

[21] J. Becker, A. Trügler, A. Jakab, U. Hohenester, C. Sönnichsen, *Plasmonics* **2010**, *5*, 161.

[22] M. A. Schmidt, D. Y. Lei, L. Wondraczek, V. Nazabal, S. A. Maier, *Nat. Commun.* **2012**, *3*, 1108.

[23] H. Chen, A. M. Bhuiya, R. Liu, D. M. Wasserman, K. C. Toussaint, *J. Phys. Chem. C* **2014**, *118*, 20553.

[24] C. Ma, Y. Liu, F. Zhao, F. Xu, J. Yan, X. Li, B.-O. Guan, G. Yang, K. Chen, *J. Mater. Chem. C* **2020**, *8*, 6350.

[25] M. Askari, M. V. Hosseini, *J. Opt. Soc. Am. B* **2020**, *37*, 2712.

[26] M. A. Abbas, A. Zubair, K. Riaz, W. Huang, J. Teng, M. Q. Mehmood, M. Zubair, *Opt. Express* **2020**, *28*, 23509.

[27] M. D. Allendorf, C. A. Bauer, R. K. Bhakta, R. J. T. Houk, *Chem. Soc. Rev.* **2009**, *38*, 1330.

[28] T. Wagner, S. Haffer, C. Weinberger, D. Klaus, M. Tiemann, *Chem Soc Rev* **2013**, 18.

[29] O. Dalstein, D. R. Ceratti, C. Boissière, D. Grosso, A. Cattoni, M. Faustini, *Adv. Funct. Mater.* **2016**, *26*, 81.

[30] C. Sanchez, C. Boissière, D. Grosso, C. Laberty, L. Nicole, *Chem. Mater.* **2008**, *20*, 682.

[31] E. Bindini, PhD thesis, **2018** 222.

[32] E. Lancelle-Beltran, P. Prene, C. Boscher, P. Belleville, P. Buvat, S. Lambert, F. Guillet, C. Boissiere, D. Grosso, C. Sanchez, 5.

[33] D. Grosso, *J. Mater. Chem.* **2011**, *21*, 17033.

[34] T. Bottein, O. Dalstein, M. Putero, A. Cattoni, M. Faustini, M. Abbarchi, D. Grosso, *Nanoscale* **2018**, *10*, 1420.

[35] T. Bottein, T. Wood, T. David, J. B. Claude, L. Favre, I. Berbézier, A. Ronda, M. Abbarchi, D. Grosso, *Adv. Funct. Mater.* **2017**, *27*, 1604924.

[36] M. Bochet-Modaresialam, J.-B. Claude, D. Grosso, M. Abbarchi, *ACS Appl. Nano Mater.* **2020**, *3*, 5231.

[37] P. N. Dave, L. V. Chopda, *J. Nanotechnol.* **2014**, *2014*, 1.

[38] M. Boudot, V. Gaud, M. Louarn, M. Selmane, D. Grosso, *Chem. Mater.* **2014**, *26*, 1822.

[39] S. Checcucci, T. Bottein, M. Gurioli, L. Favre, D. Grosso, 14.

[40] O. Dalstein, M. Tabo, E. Alvarez, L. Roux, R. Garuz, M. Pasquinelli, L. Azzi, M. Bendahan, K. Aguir, J. Loizillon, M. Abbarchi, D. Grosso, *ACS Appl. Mater. Interfaces* **2019**, *11*, 4439.

# CHAPTER 4: 2D AND 3D (NANOSTRUCTURED PATTERNS) MULTI-STACK $TiO_2$ COMBINED WITH LOW REFRACTIVE INDEX MESOPOROUS METHYLATED SILICA THIN FILM BY SOL-GEL CHEMISTRY AND NANO IMPRINT LITHOGRAPHY

Multi-stack deposition of alternating low refractive index mesoporous and high refractive index films has been an important field of research owing to the considerable optical properties and vast application (*e.g.* Bragg reflectors, waveguides, antireflective coatings, sensors, and laser).

In this chapter, first, a multi-stack of five pairs of thin films are obtained thanks to sol-gel chemistry via dip-coating on Si and glass substrates. This multi-stack has consisted of $TiO_2$ thin film with a high refractive index (n = 2.23) and mesoporous Methylated Silica with a relatively low refractive index (n = 1.2), in sequence. The deposition of thin films one atop the other with controlled thickness at nanometric scale is a challenging task owing to the infiltration in the porosity of the multi-stack. We describe the fabrication of a sequence of multi-stacks demonstrating the possibility to build a Bragg mirror with high reflectivity at visible frequency.

Second, following the same strategy, we were able to fabricate two vertical stacks of $TiO_2$ pillars by micro-contact printing Nano Imprint Lithography (NIL) and sol-gel chemistry separated by a thin silica layer avoiding intermixing of double-stacks of 3D nanostructures, we assess optical response features by spectroscopic characterization.

# 1. Introduction

Pearls, opals, moth eyes, and butterfly wings are natural examples of photonic structures showing structural color: interference between light waves reflected by periodic or random sub-wavelength domains[1,2]. Hence, the development of periodic dielectric nanostructures, *e.g*. photonic crystals (PCs), with tailored optical and built-in chemical properties has recently been brought forward by mimicking natural photonic structures with regular periodicity in one, two, or three dimensions. These systems can inhibit the propagation of certain wavelengths, giving rise to structural color as in the case of butterfly wings.

Firstly, 2D flat multi-stacks of thin films were exploited in a variety of applications in photonics, Bragg reflector mirror, antireflection coating, solar cell, sensing, and CMOS transistor[3–7]. Typical Bragg mirror reflectors consist of alternating stacks of high and low refractive index materials each one having an optical thickness of $\lambda/4$[1,3–5]. To obtain a high reflectivity at a certain wavelength while limiting the number of layers of the multi-stack, a large RI contrast is essential. A mesoporous film can be used to reduce the refractive index of one of the two layers composing the Brag mirror. However, there are several critical parameters to be controlled (*e.g.* pre- and post-synthesis treatments, thermal treatment, selective grafting, consolidation, etching, *etc.*), to form alternated thin films with varying porosities and organic functionalities precisely located along with the film thickness[3–9]. Investigation of pore interconnection size distribution in mesoporous thin films is an important factor to study multi-stack thin films consisting of mesoporous films to avoid infiltration into pores. That is why, till today, there are several works devoted to the subsequent thermal treatment for long durations in order to consolidate the silica network without decomposition of the organic template. A wide variety of bilayer mesoporous films can be synthesized by dip-coating and stabilized at 200 °C for 10-12 h[4,5].

Furthermore, as was shown in this thesis, high-Aspect-Ratio (AR) 3D nanopatterns exhibit interesting optical behavior thanks to resonant light scattering (owing to their large refractive index and reduced size) and diffraction by their regular arrangement with a periodicity close to the wavelength of the impinging light[13,14]. Benefiting from their collective optical resonances, arrays of nanostructures display sophisticated features for light manipulation with enhanced performances rather than simple flat stacks of thin films.

Hence, the initial fabrication of the 3D photonic structures such as woodpile[15–18] elaborated rapidly in order to develop certain applications in sensing, ARC, waveguide, *etc*., during the last decades[3,6,19–22]. Whereas, recently, the chirality of the stacking 3D nanostructure arrays suggested ameliorating the optical resonances in more sophisticated capabilities for light manipulation performances[23]. Moreover, simulations and few experimental works have illustrated the possibility to fabricate superimposed stack layers of 3D nanostructure patterns on top of each other[21–24]. This control of

nanoscale feature fabrications is called Moiré stacking, which typically refers to the superimposition of two identical or similar periodic lattices with translational or really small (< 20 degrees) rotational displacement. Optical investigation of these moiré patterning has been predicted theoretically[24] recently, though experimentally didn't been explored immensely, yet. Further, fabrication of the symmetries multi-stack nanopatterns atop each other such as self-assembly colloidal particles, planar rod arrays, meta-film nanoholes, and nanohole arrays in metal films, for biological and chemical sensors applications demonstrated during the last years[19,23–33]. Even though a strong understanding of the optical response of these systems is not deeply investigated, yet.

This chapter is dedicated to the evaluation of multi-stack systems with contrast refractive index from 2D flat counterparts' aspect to 3D nanostructure replicated patterns. To this approach, firstly, multi-stack thin films are prepared by dip coating. Secondly, double-stack 3D nanostructure patterns are replicated step by step via the environmental control T-NIL method, using a micro-contact printing machine, in order to control the stack replicated adjustments. Patterns consist of high RI $TiO_2$ nanostructure patterns with ~ 130 nm height are faithfully imprinted on both glass and Si substrates by NIL and sol-gel coatings. These $TiO_2$ nanostructure patterns are then embedded with the low RI intermediate mesoporous Methylated Silica (meso-MS) thin-film. This system is established experimentally for the first time amongst the other exciting works as a 3D superimposed nanostructures pattern with their Moiré effect and the control of intermixing between each stack. This novel fabrication concept, considering the contrast refractive index stacks (n of meso-MS = 1.2 and n of $TiO_2$ = 2.23) with nanometric pillars, induced notable photonic effects. As well, the optical measurement of the 3D double stack of $TiO_2$ nanostructures compared with corresponding 2D flat counterparts and a single stack of $TiO_2$ nanostructures also is demonstrated.

# 2. Experimental section

## 2.1. Investigation of multi-stack thin films of mesoporous methylated silica and dense titania

Firstly, we present the construction of multi-stacks of dense and mesoporous thin films by using RI stacks of thin films, consisting of multilayers deposited by dip-coating under controlled conditions. We explore the potential of this fabrication approach for Bragg reflectors. Furthermore, we demonstrated the small pore size distribution of the mesoporous Methylated Silica (meso-MS) thin films, which prevented the long thermal treatment and the pore's infiltration by $TiO_2$ deposition atop.

Dense $TiO_2$ thin film was prepared from a solution composed of $TiCl_4/H_2O$/EtOH/F127 with a respective molar ratio of $1:7:40:4.10^{-5}$. The final solution was obtained by dissolving the precursors $TiCl_4$ in ethanol and water followed by aging for 1h. Similarly, the meso-MS thin film was obtained from a solution composed of TEOS/MTEOS/EtOH/$H_2O$+HCl(1M)/CTAB with a respective molar ratio of 0.7:0.3:20:5:0.18. The presence of MTEOS results in a hydrophobic character of the mesoporous silica thin film. This mesoporous solution was prepared in 2 steps. First, EtOH and $H_2O$+HCl(1M) with the addition of CTAB surfactant were kept on thermal agitation at 45 °C to enhance the miscibility of the surfactant with water/EtOH before adding the precursors and to obtain homogeneous micelles sizes. Then, In the second step, TEOS and MTEOS, are added to the solution, and for fast condensation, the solution was kept in the oven for 15 min at 70 °C. Then, the final solution was again agitated for one night before deposition.

The overall system is composed of five pairs of alternated low and high refractive index layers based on meso-MS and dense $TiO_2$ (corresponding to one pair). The deposition was performed by dip-coating at a withdrawal speed of 2 $mm.s^{-1}$ under HR% < 10 and 1 $mm.s^{-1}$ at room conditions, for $TiO_2$ and meso-MS, respectively. Each layer was stabilized at 450 °C for 5 min after deposition. The thickness and refractive index after thermal treatment at 450 °C were evaluated by ellipsometric analyses for dense titania layer with n = 2.25, T = 80 nm, and meso-MS layer with n = 1.2 (~ 50% porosity) and T = 129 nm on both Si and glass substrates.

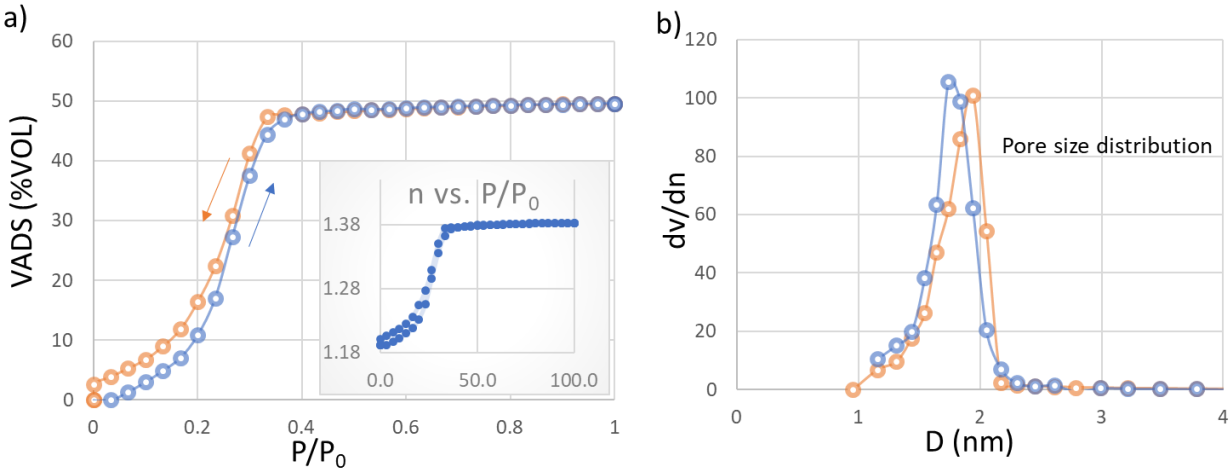



Figure 4-1. a) Absorption and desorption isotherm corresponding to the pore distribution of Vads VOL% of mesoporous methylated silica plain coating (meso-MS) measured by ellipsometry, *vs.* isopropanol relative pressure. Insert graph plotted refractive index evolution isotherm of meso-MS plain layer vs. isopropanol $P/P_0$. b) Pore size distribution extracted from isotherm using the Kelvin model[34].

In this work, we use CTAB as a surfactant. This surfactant has generally a smaller pore size of about ~ 2-3 nm rather than other agents such as F127. Moreover, adsorption and desorption isotherm of the meso-MS thin-film (see Figure 4-1) confirming the small pore size distribution of CTAB of about < 2 nm in a cylindrical model. Hence, the infiltration of the pores by the second deposition (in our case here $TiO_2$) atop was relatively avoided, whereas the solidification has occurred in a short duration with the stabilizing temperature (10 min at 450 °C). This is a considerable improvement since other reported methods required overnight mild-treatment of the low-n layer to make sure the template is not decomposed so that infiltration of $TiO_2$ does not occur. In the present case, the use of CTAB combined with a flash thermal treatment at 450 °C enables small pore formation without time for the bottleneck to enlarge upon viscous sintering. The CTAB is decomposed but the pores remain quasi totally inaccessible to the $TiO_2$ intermediates because of the pore blocking effect. According to the desorption branch of the isotherm, the size of the bottlenecks is below 2 nm. It is even likely that they are smaller than that since the desorption at such a low relative pressure of 0.25 is certainly due to catastrophic desorption instead of desorption at equilibrium [10,12,34]. The Kelvin model is thus not valid anymore and the pore size is overestimated.

A spectrophotometer was used to measure the reflection and transmission between 350 and 1000 nm from the multi-stack device of 5 pairs of $TiO_2$/meso-MS on the glass substrate (see Figure 4-2 a) and b)). The simulation is based on the nominal value of the thickness and refractive index of each stack. This simulation occurred by a reflectance calculator simulation from a complex-matrix form of the Fresnel equations. As it is shown in Figure 4-2 a) the reflection is ~ 90% comparing with ~ 95% for the simulated curve. This value determined the effective deposition of this 5 pairs multi-stack system. However, it reveals from Figure 4-2 a) experimental multi-stacks have a photonic stop

band of about 2 times narrower than nominal simulation. Moreover, around 200 nm reflectance shift of experimental multi-stack in comparison with the simulation one is observed. It is presumed that these tackles could be due to a thickness difference between the nominal and the reflected one. In all likelihood, thin-film deposition after several stacks will be affected by the dewetting or/and adherence of its underlying layers. Thereby, this phenomenon might affect thickness reduction in multi-stack films.

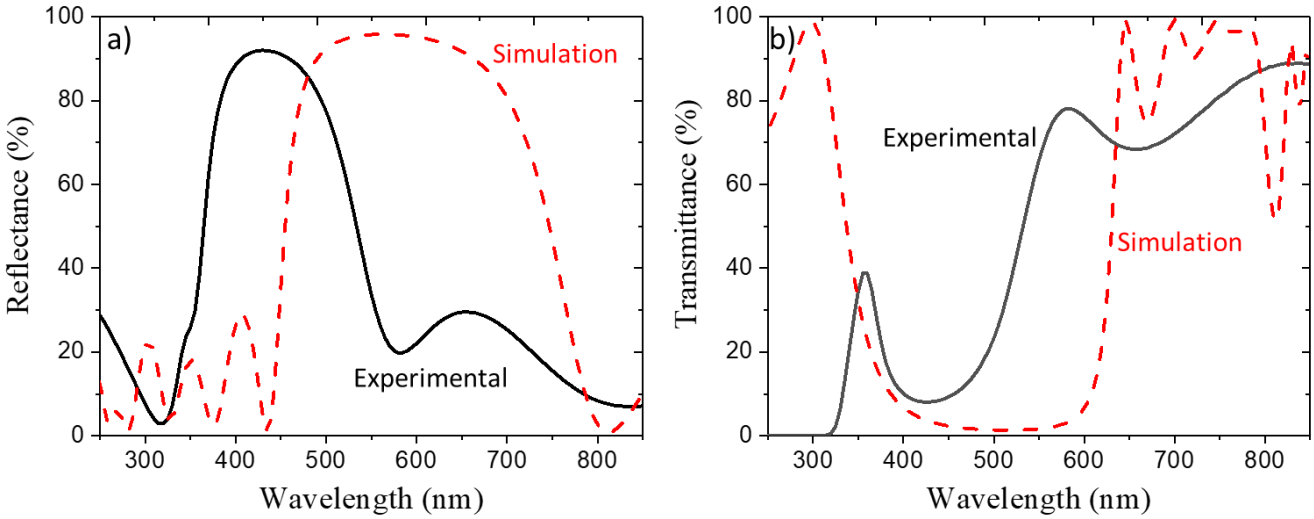



Figure 4-2. Spectrophotometer results of the 5 paires multi-stack thin films on glass substrate. a) Reflectance b) Transmittance of the system in black line in comparison with simulation in dashed red line.

Measured thickness by ellipsometry and an SEM cross-sectional view executed from the 5 pairs multi-stack on Si wafer confirmed the gradual decrease in thickness of the thin films in each pair (Figure 4-3 a)). In the first 3 pairs, $TiO_2$ and Meso-MS have relatively identical thickness, however, from the $4^{th}$ pair to the $5^{th}$ pair there is a relative reduction in thickness in both films between 10 and 20 nm. The substantial simulation of reflectance of the multi-stack based on the thickness value extracted from the SEM/ellipsometry demonstrated the more identical photonic stop band to the experimental one. Figure 4-3 d) shows the reflection data of the system in comparison with the nominal and substantial simulation. Despite this fact, the reflection of the system reaches R ~ 95 % which is a significant value comparing with simulated ones.

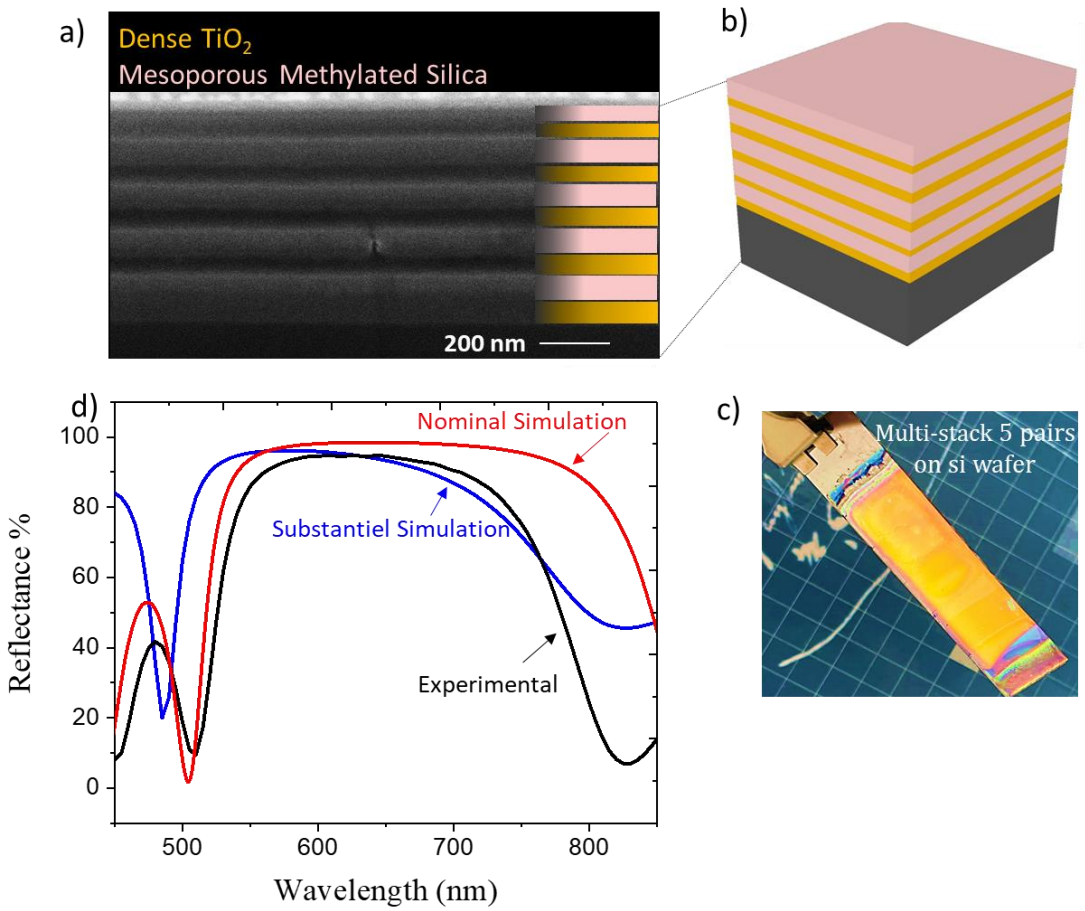



Figure 4-3. a) Cross-sectional SEM micrograph of the five pairs system. b) Schematic illustration of the sequence RI contrast multi-stack thin films. c) Optical photograph of RI contrast multi-stack thin films sample. d) Plot of the refractance of the system in black line comparison with the nominal simulatin in red line and subestantiel simulation in blue line.

It should be noted that this thickness changes from 1st pair to the last pair is the critical point of this part, which didn't optimize yet.

It requires accurate measurements of the thickness with the precise control of the deposition layer by dip coating, for optimization of the optical response of the system. Thereby, in the next section, 3D nanostructure multi-stacks are limited by deploying three layers of the thin film. Whereas the flat 2D layer is replacing with $TiO_2$ nanostructure pillars and Meso methylated silica remained as an intermediate thin film layer.

## 2.2. Fabrication of 3D double-stack super-imposed nanopatterns by replication of $TiO_2$ nanostructures combined with meso-MS thin layer by pressure and environmental control T-NIL

For high-performance optical properties, replication of nanostructures arrays was investigated during the last decades[2] by NIL. The presence of the nanostructure 3D arrays enhances the signal by almost an order of magnitude with respect to the 2D flat counterpart and is attributed to the antenna effect, enhancing the interaction of the confined electromagnetic wave with the sensitive medium. Hence, the RI multi-stack embedded with 3D nanostructure arrays is elaborated in this section as a novel fabrication method.

For this task, we exploited the NIL technique for replicating the nanostructure arrays of $TiO_2$ replacing them with the flat 2D titania thin film. NIL fabrication has occurred under the pressure and environmental control T-NIL method using a micro-contact printing machine coupled to an optical microscope to adjust each stack of $TiO_2$ nanostructure arrays atop of other (see Figure 4-4). This machine consisted of 1) the automated control of z-direction of the printer head, 2) the compressed gas pressure adjusted to 4-8 bar in order to inflate the PDMS while imprinting and, 3) the heat plate integrated with work palate to induce the cross-linking of the metal oxides composing the printed nanostructures pillars (at maximum 100 °C), (see Figure 4-4). More details are provided in appendix 1.

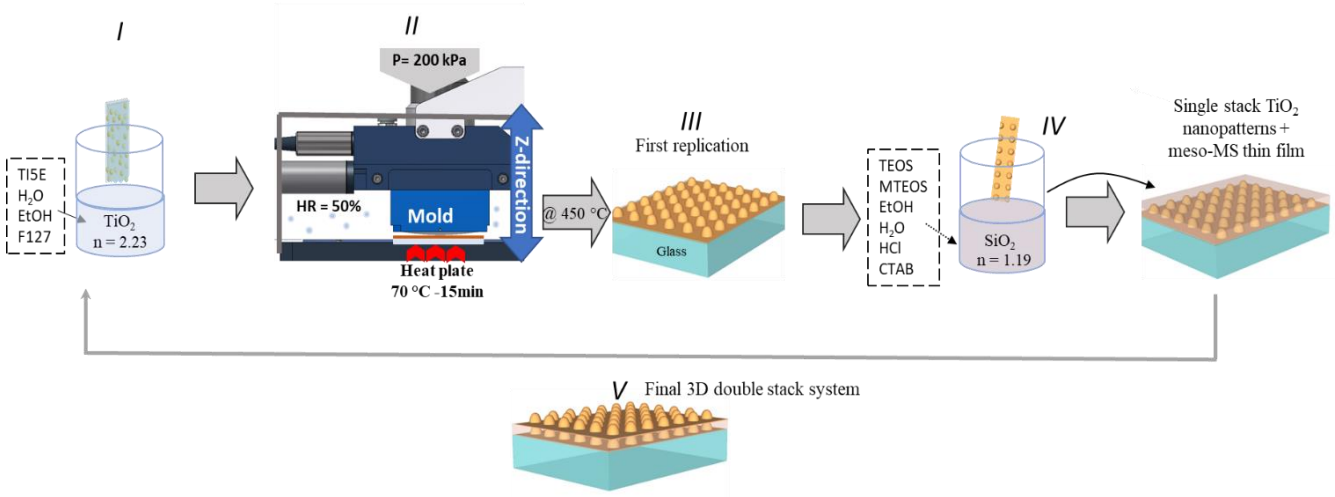



Figure 4-4. Schematic representation of 3D multi-stack nanostructure system NIL process. *I.* Dip-coating deposition of $TiO_2$ solution on e.g. glass bare substrate. *II*. Micro-contact NIL machine, imprinting pillars under P = 200 kPa, HR = 50%. *III*. After crosslinking, the PDMS pulled off and final thermal treatment occurred at 450 °C. First final imprint of $TiO_2$ replicated patterns are obtained. *IV*. Mesoporous methylated silica solution dip coated on $TiO_2$ pillars. And process will be repeated in subsequence from *I*, for *V*. Final 3D imposed pillars.

The $TiO_2$ 3D nanoarrays are fabricated as follows. Firstly, a PDMS mold was prepared from a hard master that consist of silicon pillars arranged in a hexagonal array. It was obtained via Electron Beam Lithography (EBL) and reactive ion etching and was provided by OBDUCAT Technologies. The master surface was rendered hydrophobic by immersion for 1h in a vapor of 1H,2H,2H perflunedectyl triethexysilane in a closed chamber, followed by an abundant rinsing with ethanol. The PDMS precursors and reactant mixture (90w% agent A; 10w% agent B from SILGARD) were then poured onto the functionalized master surface and cured at 70 °C for 4 hours. The PDMS mold was then peeled off after cooling and directly pumped in a primary vacuum for 10 min under ~ 10 mbar before starting NIL.

Secondly, titania solution was prepared by mixing 1 $TiCl_4$: 40 EtOH: 7 $H_2O$: $4.10^{-5}$ F127 molar ratios, all purchased from Aldrich. Afterward, both Si wafer and glass bare substrate was dip-coated into the $TiO_2$ solution at 2 $mm.s^{-1}$ withdrawal speed under relative humidity HR < 10%. The as-prepared film was transferred immediately to the micro-contact machine for nanoimprinting. The PDMS mold on the printer head was brought down in contact with the thin film under 50% HR with a pressure of 200 kPa. Subsequently, the heat plate induced the crosslinking of the pillars heating at 70 °C for 15 min. The mold was then brought back to the higher position and the sample was annealed at 450 °C for 10 min.
Structural investigation of the nano-imprinted sample was performed by Atomic Force Microscopy (PSIA XE-100 AFM) and high-resolution scanning electron microscopy (FEI Strata DB235 with 5 kV electron acceleration voltage).
SEM and AFM images account for a faithful imprint of $TiO_2$ pillars homogeneously organized in a hexagonal pattern with 130 nm height and ~ 250 nm width (see Figure 4-5 b), c) and d)). AFM analysis reveals a 75% volume shrinkage of the $TiO_2$ replicated patterns with respect to the master (shrinkage in height and width are 43% and 32%, respectively), (see Figure 4-5 a), b) and c)). The reduction in the pillar dimensions is a volume shrinkage, attributed to the typical elimination of the volatile species during drying and thermal annealing of the sol-gel.

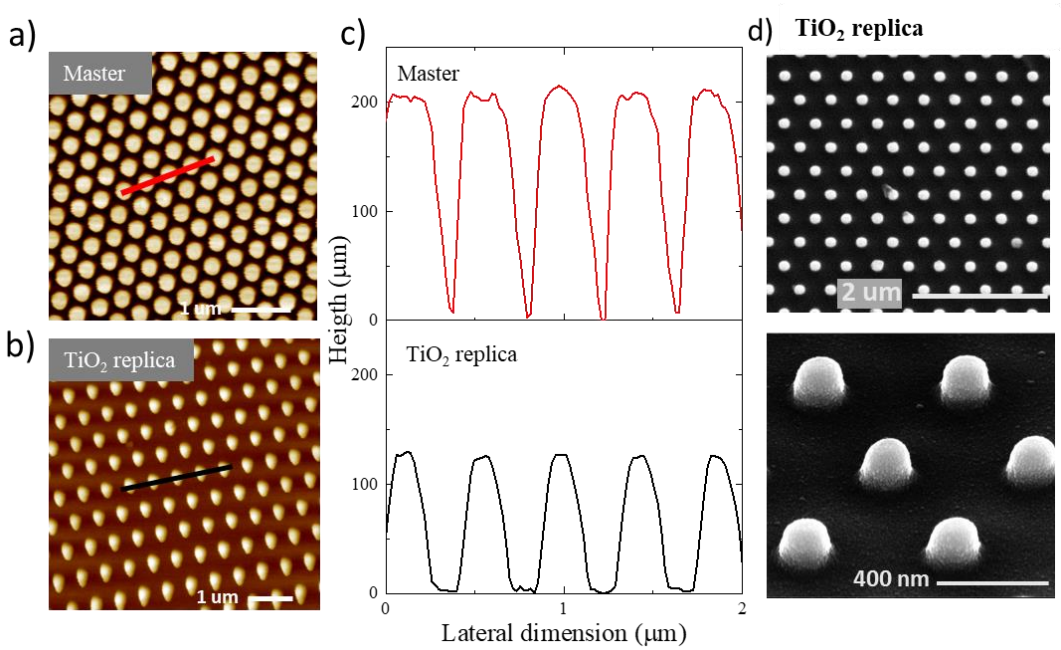



Figure 4-5. AFM images of a) Master and b) $TiO_2$ replicated patterns. C) Height profile of master (red line) and $TiO_2$ replicated patterns (black line) taken from the zone corresponding to the dashed line, indicated in a) and b). e) SEM images of $TiO_2$ replicated patterns from top to bottom panel, top view and 52° tilted, respectively.

By using the same setups (sol-gel dip coating and NIL micro-contact machine), we can print a second stack of pillars atop the first layer (see Figure 4-4). This is performed by two approaches, 1) covering the first pillars with meso-MS layer (using the same method as before explained) by dip-coating at room temperature in order to flatten the surface of the sample and 2) printing the second layer of $TiO_2$ pillars atop.
As it was mentioned before, a critical drawback to producing a multi-stack is the diffusion of the atop layer into the mesopores. For applications in optics, it is important to maintain the largest possible refractive index contrast between the pillars and the environment. At the same time, the intermediate layer must be sufficiently flat and homogenous to permit second nanoarrays to become faithfully replicated.

Figure 4-6 illustrates that the approaches to fabricated double stack pillars are faithfully achieved. From Figure 4-6 a) the final schematic of this system is presented. The visual inspection of the coating revealed a bright scattering accounting for diffraction from the high refractive index ordered pillars. The combination of two superposed hexagonal pillar arrays having a small tilt angle (randomly happened ~ 1°) one concerning the other, results in a periodic hexagonal so-called Moiré pattern (see Figure 4-6 b) and c)). They can be viewed as the superimposition of rotations of two or more Bravais lattices by a commensurable angle.

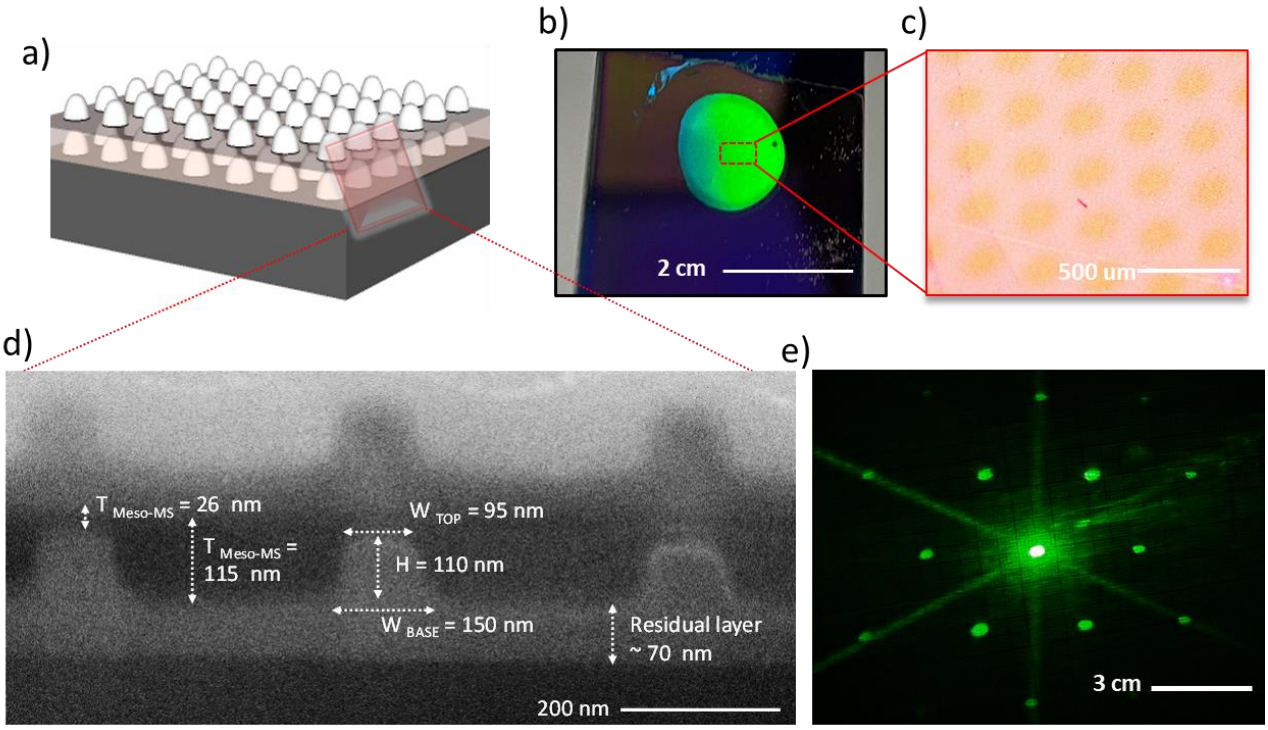



Figure 4-6. a) Schematic presenting the final 3D double stack system with $TiO_2$ pillars topography on *e.g.* Si wafer. b) Photography image (scattering green color), c) Bright field optical microscope image (50X, NA = 0.8 objective lens) demonstrates the Moiré patterns, d) Cross sectional SEM image of the and e) Diffraction pattern of 532 nm green laser light of a 3D double stack of $TiO_2$ nanostructure on a Si wafer.

To determine more precisely the morphology of the structures, a profile view of the arrays was obtained by SEM, as shown in Figure 4-6 d). The identical morphologies and dimensions of pillars were obtained from both $TiO_2$ imprinted stacks. Moreover, a thin 30 nm meso-MS layer covered homogeneously atop the first array of $TiO_2$ pillars as a separator. Furthermore, for both pillars arrays, a residual layer of an estimated thickness of around 70 nm was observed. The height of the pillars from the top level of the residual layer was obtained H = 110 ± 10 nm, while the base and the top of the pillars have the dimension of $W_{BASE}$ = 150 ± 10 nm and $W_{TOP}$ = 115 ± 10 nm, respectively (See Figure 4-6 d)).

Further evidence of Moiré pattern formation can be obtained via laser diffraction. This was obtained by shining a laser beam $\boldsymbol{\lambda}$ = 532 nm on the double 3D stack of pillars at quasi-normal incidence (~ 4 degrees) and imaging the reflected light at 43 cm far from the sample. The reflected patterns are projected on millimetric paper and photographed by a smartphone camera (see Figure 4-6 e)).

# 3. Optical investigation

Optical performances of the 3D double stack nanostructure have been addressed by measuring reflectance, transmittance (for glass bare substrate cases) exciting the samples at the quasi-normal incidence, and using spectrophotometer mounting integrating sphere. Specular reflection as a function of the incidence angle was measured by using respectively a goniometer. We investigated the 3D double stack comparing its optical properties with a single stack embedded with meso-MS above it and with the corresponding flat 2D counterpart.

Reflection spectra of samples printed on a Si wafer (Figure 4-7 a)) shows marked resonance peaks for the 3D double stack of pillars with respect to the single stack accounting for the possibility of accomplishing more sophisticated optical functions. Figures 4-7 b) and c) represented the bidirectional angular reflected intensity of 3D double stack patterns in a different scanning direction. Due to the peculiar angular hexagonal diffraction patterns, we consider the 2D hexagonal lattice effects by two high symmetry M and K points with the reciprocal lattice vector directions. Thereby, scanning broad angular reflectance from 2° to 50° indicated once in K hexagonal lattice symmetry direction (Figure 4-7 b)) and then, by rotating sample 90 degree, to M symmetry of hexagonal lattice zone. Note also that relevant angular spectral applied for single stack patterns as it is shown in Figure 4-7 d).

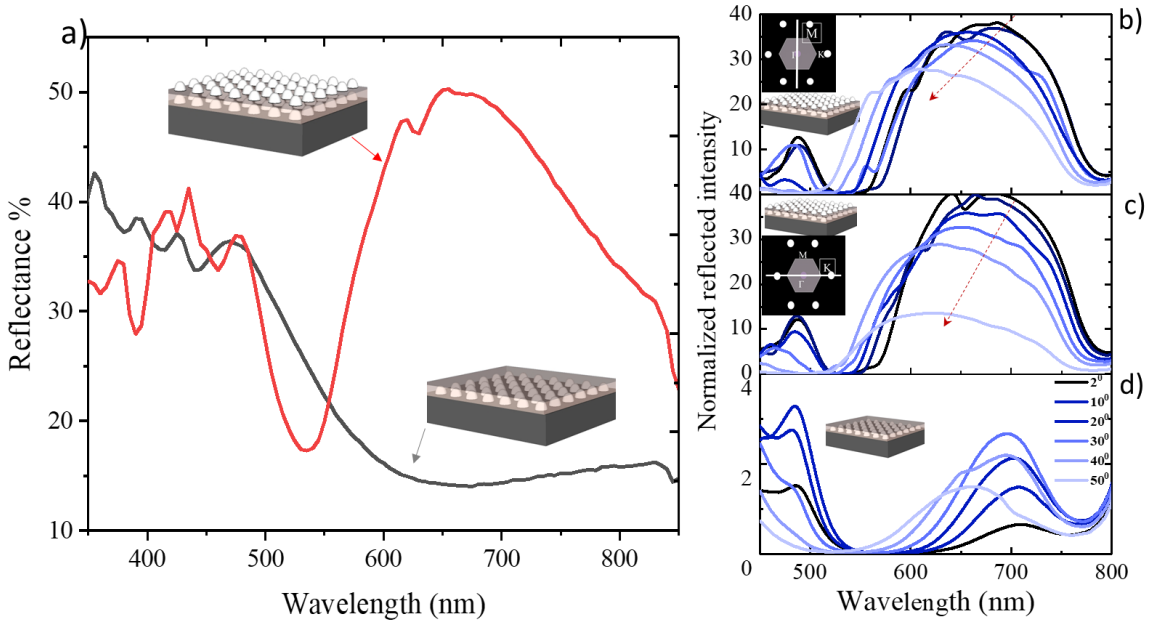



Figure 4-7. a) Total reflected intensity for the 3D double stack nanostructure (red line) and single stack nanostructure (black line) were measured by spectrophotometry. Angle-resolved specular reflection from 2° to 50 °normalized to the reflection of the mirror b) For 3D stack nanostructure patterns scanned through the K and c) Scanned through M symmetry of hexagonal Brillion zone and d) For single stack nanostructure patterns.

Total reflection and transmission of a single and 3D double stack of pillars as well as the flat 2D counterparts on glass bare substrate were measured by a spectrophotometer (Figure 4-8). Multiple and sharper peaks emerge in both transmission and reflection spectra (see Figure 4-8) in the case of complex geometries 3D double stack nanostructure patterns with respect to plain layer 2D flat multi-stacks. Multi-stack plain layers indicate the same reflected intensity spectra features with the RI multi-stack 3D nanostructured patterns systems, although sharp peaks and narrow resonance arose from the promising interference and diffraction in presence of nanostructure 3D and 2D arrays (see Figure 4-8 a)). Furthermore, it was revealed from the spectra transmitted intensity a reduction of about 15% for single stack nanostructure patterns in comparison with its corresponding plain layer stack. Moreover, 3D double stack nanostructure patterns illustrated near 40% transmittance decline in comparison to the 2D plain layer stacks (see Figure 4-8 b)).

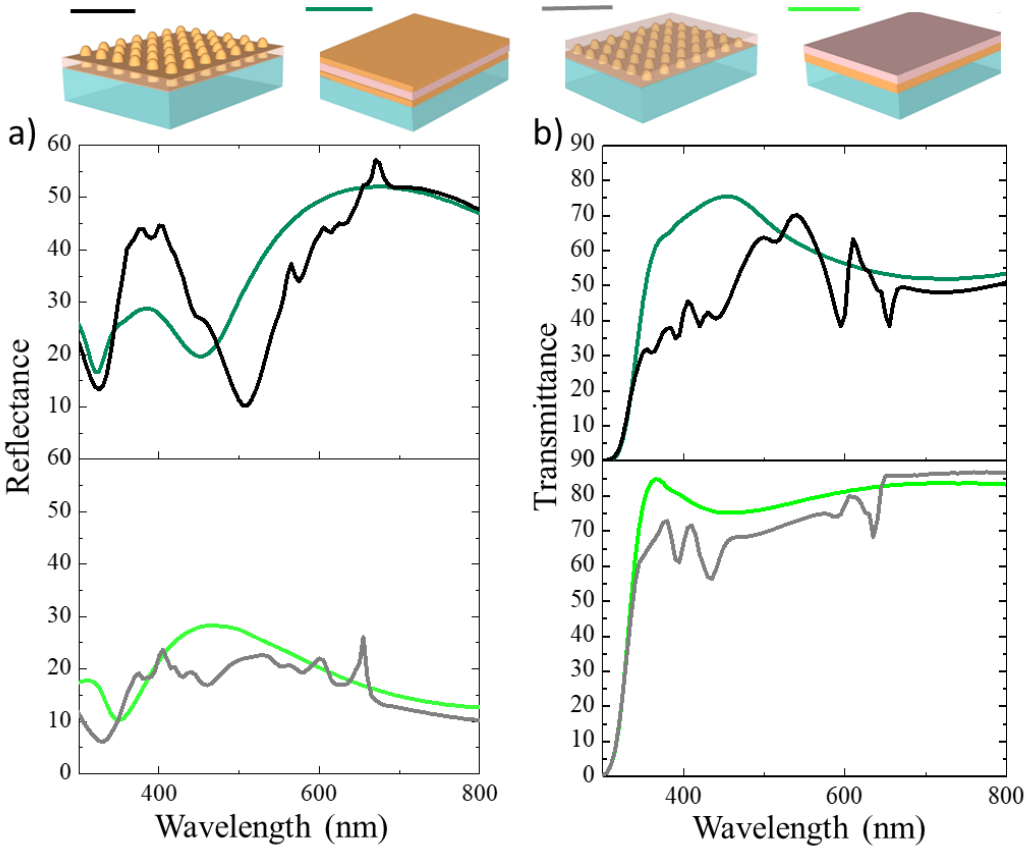



Figure 4-8. a) Total reflectance and b) Total transmittance spectra for top panels: double 3D stacks nanostructure patterns (black lines) and its corresponding 2D plain thin film stacks (dark green lines) and bottom panels: 2D single stack nanostructure patterns (gray lines) its corresponding 2D plain thin film stacks (light green line).

# 4. Conclusion

This chapter is dedicated to the presence of the alternating the low and high refractive index multi-stacks embedded with a 3D double stack of $TiO_2$ nanostructure arrays (Moiré stacking) enhancing the resonances peak and the light interference, in comparison with its corresponding 2D plain thin-film multi-stacks or even the single $TiO_2$ nanostructure replica covered with low RI thin film.

First, We showed the deposition of $TiO_2$ film atop meso-MS in a sequence of 5 pairs homogeneously over the entire surface (glass and Si substrate) according to the methods proposed before by Faustini et al[5]. Whereas, spectroscopy analysis of the samples highlights the photonic bands R ~ 90 - 95% for both glass and Si wafer, close to the simulation. Then, the system framed in superposition $TiO_2$ (n = 2.23) nanostructure replicated patterns, which advanced the new fabrication of imposed stacking NIL method, which never been existed before. This fabrication was accomplished thanks to the rapid, cost-effective, and simple fabrication route: sol-gel chemistry, and environmental control T-NIL.

Moreover, we illustrated the intermediate Meso-MS thin film (n = 1.2) with the remarkably thin thickness (~ 30 nm) on the first imprinted $TiO_2$ nanostructure patterns. Moreover, avoiding intermixing is demonstrated. We reported the deposition of high RI dense $TiO_2$ on the thin meso-methylated silica film with considerable control of pore infiltration while final annealing occurred rapidly in comparison with other existed studies in which thermal treatments took place in a long duration.

It should be considered that there are several critical parameters for optimization this system consists of 1- the control on the thickness of deposited thin-films in the multi-stack system, 2- the number of contrast RI stacks, 3- the shape of the scattering geometry of the pillar (aspect ratio and morphologies), 4- an increasing number of superimposing nanostructure patterns stacks, and finally the residual layers free of nanostructures arrays. These optimizations of parameters didn't fit the time of this thesis; indeed, they can be the novel elaboration path in the continuation of this project.

# 5. References


[1] H. Shen, Z. Wang, Y. Wu, B. Yang, *RSC Adv.* **2016**, *6*, 4505.
[2] H. K. Raut, V. A. Ganesh, A. S. Nair, S. Ramakrishna, *Energy Environ. Sci.* **2011**, *4*, 3779.
[3] C.-Y. Fang, Y.-L. Liu, Y.-C. Lee, H.-L. Chen, D.-H. Wan, C.-C. Yu, *Adv. Funct. Mater.* **2013**, *23*, 1412.
[4] P. C. Angelomé, M. C. Fuertes, G. J. A. A. Soler-Illia, *Adv. Mater.* **2006**, *18*, 2397.
[5] M. Faustini, D. R. Ceratti, B. Louis, M. Boudot, P.-A. Albouy, C. Boissière, D. Grosso, *ACS Appl. Mater. Interfaces* **2014**, *6*, 17102.
[6] M. C. Fuertes, S. Colodrero, G. Lozano, A. R. González-Elipe, D. Grosso, C. Boissière, C. Sánchez, G. J. de A. A. Soler-Illia, H. Míguez, *J. Phys. Chem. C* **2008**, *112*, 3157.
[7] Z. Deng, H. Jiang, Y. Hu, Y. Liu, L. Zhang, H. Liu, C. Li, *Adv. Mater.* **2017**, *29*, 1603020.
[8] J. Briones, E. Briones, 9.
[9] I. Pavlichenko, A. T. Exner, G. Logvenov, G. Scarpa, P. Lugli, B. V. Lotsch, *Can. J. Chem.* **2012**, *90*, 1069.
[10] J. Loizillon, M. Putero, D. Grosso, *J. Phys. Chem. C* **2019**, *123*, 30398.
[11] B. Baumgartner, J. Hayden, J. Loizillon, S. Steinbacher, D. Grosso, B. Lendl, *Langmuir* **2019**, *35*, 11986.
[12] J. Loizillon, B. Baumgartner, C. Sinturel, M. Abbarchi, B. Lendl, D. Grosso, *J. Phys. Chem. C* **2019**, *123*, 23464.
[13] S. Zhu, H. Li, M. Yang, S. W. Pang, *Nanoscale* **2018**, *10*, 19927.
[14] I. Wathuthanthri, Y. Liu, K. Du, W. Xu, C.-H. Choi, *Adv. Funct. Mater.* **2013**, *23*, 608.
[15] T. Glinsner, P. Lindner, M. Mühlberger, I. Bergmair, R. Schöftner, K. Hingerl, H. Schmid, E.-B. Kley, *J. Vac. Sci. Technol. B Microelectron. Nanometer Struct.* **2007**, *25*, 2337.
[16] R. Kothari, M. R. Beaulieu, N. R. Hendricks, S. Li, J. J. Watkins, *Chem. Mater.* **2017**, *29*, 3908.
[17] C. Peroz, V. Chauveau, E. Barthel, E. Søndergård, *Adv. Mater.* **2009**, *21*, 555.
[18] W. Li, Y. Zhou, I. R. Howell, Y. Gai, A. R. Naik, S. Li, K. R. Carter, J. J. Watkins, *ACS Appl. Mater. Interfaces* **2018**, *10*, 5447.
[19] Y. Zhang, W. Liu, Z. Li, Z. Li, H. Cheng, S. Chen, J. Tian, *Opt. Lett.* **2018**, *43*, 1842.
[20] M. Miyamoto, T. Kubo, M. Sonehara, T. Sato, Y. Fujishiro, K. Shiota, 8.
[21] S. Checcucci, T. Bottein, M. Gurioli, L. Favre, D. Grosso, M. Abbarchi, *Adv. Opt. Mater.* **2019**, 1801406.
[22] M. Bochet-Modaresialam, J.-B. Claude, D. Grosso, M. Abbarchi, *ACS Appl. Nano Mater.* **2020**, *3*, 5231.
[23] Z. Wu, Y. Liu, E. H. Hill, Y. Zheng, 44.
[24] P. Wang, Y. Zheng, X. Chen, C. Huang, Y. V. Kartashov, L. Torner, V. V. Konotop, F. Ye, *Nature* **2020**, *577*, 42.
[25] H. A. Gómez-Urrea, M. C. Ospina-Medina, J. D. Correa-Abad, M. E. Mora-Ramos, F. J. Caro-Lopera, *Opt. Commun.* **2020**, *459*, 125081.
[26] H. A. Gómez-Urrea, J. Bareño-Silva, F. J. Caro-Lopera, M. E. Mora-Ramos, *Photonics Nanostructures - Fundam. Appl.* **2020**, *42*, 100845.
[27] V. Saveljev, S.-K. Kim, J. Kim, *Opt. Eng.* **2018**, *57*, 19.
[28] S. M. Lubin, W. Zhou, A. J. Hryn, M. D. Huntington, T. W. Odom, *Nano Lett.* **2012**, *12*, 4948.
[29] M. Tang, H. Xie, J. Zhu, X. Li, Y. Li, *Opt. Express* **2012**, *20*, 2942.
[30] S. Wu, H. Xia, J. Xu, X. Sun, X. Liu, *Adv. Mater.* **2018**, *30*, 1803362.
[31] J.K. Gansel, M. WeS.Burger, S. Linden, *OPTICS EXPRESS*, **2010**,18,/ oe-18-2-1059.pdf, .

[32] A.J. Mastroianni, S.A. Clarifge, A.P. Alivisatos, *J. AM. CHEM. SOC*. **2009**, 131, 8455–8459mastroianni2009.pdf, .
[33] B. M. MAoz,A.B. Moshe, D. Vestler, O.Bar-Elli, G. Markovich, *Nano Lett.* **2012,** 12, 2357−2361 , doi.org/10.1021/nl300316f | maoz2012.pdf, .
[34] C. Boissiere, D. Grosso, S. Lepoutre, L. Nicole, A. B. Bruneau, C. Sanchez, *Langmuir* **2005**, *21*, 12362.

# GENERAL CONCLUSION AND PERSPECTIVES

This thesis aims at the investigation of a novel sol-gel coating production technology known as Soft-Nano Imprint Lithography (environmental control Thermal-NIL) and propose applications for each manufactured system. Sol-gel chemistry allows us to control the desirable properties of the as-prepared chemical solutions. A liquid deposition procedure with precise thickness and homogeneity control is used to deposit thin films on a defined substrate. In addition, the NIL fabrication approach revealed the capacity to create a variety of 3D high aspect ratio nanometric morphologies with high resolution, throughput, speed, and cost-effectiveness. For these reasons, in this thesis, we showcase first, methylated silica nanostructure patterns on a large glass substrate, second, $TiO_2$ high aspect ratio nanostructure patterns imbedded with a micro-porous silica thin film atop, and third, the feasibility of the double-stack alternating refractive index of super-imposed 3D nanostructure patterns atop each other separated by a 2D mesoporous methylated silica flat layer.

The examination of various combinations of top-down and bottom-up approaches – which were successfully used in soft-lithography processes and enabled the development of unique photonic systems – exemplifies the scientific approach. Furthermore, results obtained here showcase the tremendous potential of combining different techniques (materials, fabrication parameters, methods, and morphologies) to open various opportunities and developments in realistic applications compatible with industrial fabrication methods.

In chapter 1, I provided a detailed description of nanofabrication and NIL technologies, including their history and recent progress, soft-NIL optimization of replication in hard inorganic materials, and their advantages over regular lithography methods. The methods are described in-depth, and they include embossing, soft polymer processing, hard inorganic materials with a high dielectric constant, as well as sol-gel chemistry. Many existing methods of NIL and their gradual elaboration are described. UV-NIL has been the dominant approach; nonetheless, it needs sophisticated chemistry and expensive, frequently toxic photo-initiators. Thermal-NIL has recently been developed in conjunction with pressure or environmental control, allowing for more straightforward chemistry. Furthermore, high thermal treatments create material stabilities and residual solvent breakdown, but they also generate a more or less significant volume shrinkage. Obtaining an accurate, shrinkage-free replication by soft-NIL in pure inorganic material remains a future problem that appears unattainable with the approaches that are revealed thus far.

We proposed the control of the residual layer of the replicated pillars when fabricating high aspect ratio methylated silica or $TiO_2$ nanopatterns with graded morphologies (nipple-dimple), replicated single and double face as broad-angle, broadband, anti-reflection coating, and optical gas sensors. The residual layer is a major drawbacks after the NIL replication of inorganic materials on the performance of anti-reflection coatings and is the most difficult element to control. If the residual layer is reduced, ARCs are expected to have better antireflective qualities due to reduced reflected intensity. There is an approach that is currently being investigated: micro-transfer molding. Adopting this approach in conjunction with the T-NIL technology is recommended. Another possibility is that by managing the chemical affinity between the replicated patterns and substrate layers, the brittle replicated pillars can be avoided.

In addition, the fabrication of $TiO_2$ nanopatterns composite framed by a soft layer of micro-hybrid silica provides good sensitivity and selectivity that constitutes critical transduction elements to design and elaborate a cost-effective "artificial nose" for optical gas sensors. The performance of this nanocomposite optical transduction system in terms of refractive index variation sensitivity has been increased. In gas sensing, the selected microporous hybrid silica-sensitive components demonstrated an unusual partial selectivity. There is also a brief investigation of gas sensitivity based on changing inlet gas concentration (nm/ppm). Nonetheless, it is far away from the thesis' main themes; it would be a good candidate for a deeper examination. We demonstrated successful replication concerning the novel exploration route of sol-gel chemistry and NIL technique based on the multi-stack fabrication of alternating high ($TiO_2$, n = 2.2) and low (meso methylated silica n = 1.2) refractive index layers. The fabrication of double-stack 3D nanostructures validates the possibility of replication for 'n' stacks. The investigative studies, on the other hand, are still ongoing, and the findings and observations are preliminary. A deeper study on multi-stacking is necessary to confirm the efficiency of the systems in terms of optical performance—replication of the higher aspect ratio nanopillars, which are expected to feature a greater intensity peak and sharper resonances. Moreover, instead of the 2D flat thin layer of the meso-MS, its 3D replication nanostructure pillars are suggested. Furthermore, the deposition of the initial films is proposed to be optimized in terms of its thickness and roughness.

Finally, the replication of ferroelectric materials like $BaTiO_3$ is currently being researched. The use of nanoscale devices to elaborate the system based on and electrical conversion enhancement is recommended. Because of its built-in electric field, $BaTiO_3$ nanoparticles are ideal for increasing the electrochemical performance of energy conversion devices. Therefore, located in-between photonic crystal cavities and plasmonic nanoparticles, Mie resonators offer an alternative way to enhance light-matter interaction at the nanoscale. The elaboration of a new method of replication of the 3D $BaTiO_3$ NPs Mie resonators nanopillars will be the subject of new studies for original optical devices. This fabrication is under investigation in collaboration with the Institute of Quantum Electronics and Optical Nanomaterial of ETH-Zurich. Thus, this thesis proposes new sol-gel materials that improve throughput, flexibility, and resolution while addressing some of the drawbacks

of conventional lithography approaches. We also developed a prototype to show the practicality of the latter technique, paving the way for sol-gel soft-NIL technologies in a variety of industrial applications. To conclude, the fabrication of high aspect ratio hybrid silica and $TiO_2$ nanostructures patterns and their combination in 3D structures super-imposed in a successive stacking system was described during this Ph.D. work. It demonstrates how the sol-gel chemistry/nanoimprinting coupling may be used to create sophisticated 2D and 3D designs on very large surfaces at a minimal cost. More importantly, it eliminates the need for costly and harmful commercial resins with restricted physical qualities. Indeed, the versatility of chemical compositions accessible by sol-gel brings an additional dimension to this mode of manufacture, making possible the direct structuring of ceramics where optical (n, k, emissivity), electrical (conductivity, piezoelectricity), mechanical (hardness), chemical (surface, specific surface associated with porosity) properties can be chosen amongst the inorganic materials.

# APPENDIX 1

# 1) The general concept of sol-gel chemistry

In the early 1940s, elaboration of sol-gel technology on transparent oxide layers for glass coating has been started by Schott and co-workers. The sol-gel process becomes an interesting method for several industrial uses due to the low-temperature synthesis, simple equipment uses, thin-film formability, and its versatility to obtain materials with a wide range of forms and functionalities. Moreover, the sol-gel chemistry induces the possibility of tuning the structure of various materials down to the nanometer scales. The sol-gel process provides the formation of metal oxides by inorganic polymerization of molecular precursors in solutions such as metal salts or metal alkoxides. These syntheses are generally carried out in hydro-alcoholic or aqueous media under hydrothermal conditions. In sol-gel chemistry, sol is the stable suspension colloidal (nanoparticles) in liquid with a small dispersed solid size of < 10 μm. These particles can be amorphous or crystalline, dense, porous, or polymeric substructure.

Two important reactions take place in the sol-gel process: hydrolysis and condensation. The reaction of precursors with water is hydrolysis, whereas, the exchange of the hydroxyl ions is called a condensation reaction. With time and successive condensation, molecules grow bigger and the inorganic polymers are formed. Indeed, precursors are hydrolyzed or condensed, either in aqueous or organic solvents, to form inorganic polymers composed of M-O-M bonds. For inorganic precursors, hydrolysis occurred by nucleophilic substitution of the initial ligand with water to yield $O^-$, OH, or $OH_2^+$ ligands, depending on the nature of the metal and the pH. Likewise, in condensation reactions, hydroxo or oxo bonds are formed by the elimination of a molecule of water or the acid form of the initial ligand (see Figure 1). In both reactions, kinetics govern the configuration of the intermediates and final product and are controlled by a fine-tuning of the pH (acidic or alkaline catalysis), the concentration, the molar ratio of water, the temperature, and the precursor reactivity[1].

$$\equiv M\text{-}X + H_2O \leftrightarrow \equiv M\text{-}OH + HX \quad (a) \qquad \text{Hydrolyse}$$

$$\equiv M\text{-}OH + \equiv M\text{-}OH \leftrightarrow \equiv M\text{-}O\text{-}M + H_2O \quad (b)$$

$$\equiv M\text{-}X + \equiv M\text{-}OH \leftrightarrow \equiv M\text{-}O\text{-}M + HX \quad (c) \qquad \text{Condensation}$$

Figure 1. Equation of sol-gel process reactions[2].

There are two important systems in the sol-gel process; silicate and non-silicate systems. The principle behind the silicate system is the transformation of Si-OR and Si-OH. To obtain the sol stability, cross-linking through Si-O-Si should be maximized. The

hydrolysis and condensation induce more electrophilicity for silicon atoms. The most used silicates are Si $(OC_2H_5)_4$ or tetraethoxysilane (TEOS) and methyltriethoxysilane precursor (MTEOS). However, non-silicate systems such as 'transition metal oxides' (in particular $TiO_2$), are more reactive than silicate systems due to their elevated coordination number (> 4) and high electrophilicity. In non-silicate systems, insoluble species can be formed and undergo precipitation or crystallization[1–3].

In this thesis silicate systems (hybrid micro/mesoporous silica) and non-silicate systems ($TiO_2$) were prepared by sol-gel chemistry. Understanding the sol-gel chemistry phenomena leads to the elaboration of the self-assembly, as well as good control of liquid deposition processes for thin films.

# 2) Liquid deposition technique

The liquid deposition technique is thus today regarded as a reliable process, complementary to dry deposition techniques because they combine excellent control over the layer's inner structure and composition while keeping the manufacturing rapid and cost-effective. Amongst the various existing liquid deposition techniques, the most used are spin-coating and dip-coating as they have many advantages. In this thesis, all film deposition was performed by dip-coating and spin coating.

# 3) Dip coating

Dip coating is one of the most used methods in the laboratory and industry to deposit the homogenous thin film on a surface with a controlled thickness. The principle of the dip coating is to dip the substrate into the solution and vertically withdrawn at a constant speed (see Figure 2). Deposition by dip-coating leads to the coated thin film on both sides of the substrate. The thickness of the thin film is governed by the deposition parameters such as withdrawal speed, temperature, relative solvent, vapor pressure, *etc*. Figures 2 b) and c) illustrate the two regimes in dip-coating induced by the withdrawal speed leading to the thickness of the thin film. At high withdrawal speed, the film formation is determined by the viscus dragging. This regime is called a draining regime. The theory of this regime was established by the Landa Levich model (LL), (Equation 1). This equation determines the thickness (h) of the deposited film, where $\boldsymbol{\eta}$, $\boldsymbol{\rho}$ and $\boldsymbol{\gamma}$ are viscosity, density, and the LL viscous drag, respectively. Contrary, at low withdrawal speeds (< 0.1 mm.sec$^{-1}$ ), the film formation is followed by the Laplace model, no dragging is involved, and the film thickness is directly related to the solvent evaporation[4–6]. This regime is called the capillary regime.

$$h = \frac{0.94\,(\eta u)^{2/3}}{\gamma_{LV}^{1/6}(\rho g)^{1/2}} \qquad \text{Equation (1)}$$

Moreover, Faustini et al. used an experimental approach to investigate the variation of sol-gel coating thickness applied at speeds ranging from 0.01 to 20 mm.s$^{-1}$[5]. This semi-empirical model equation (given in Figure 2 d)) allows predicting the final film thickness h as a function of the withdrawal speed u. Where k is the material proportional constant (proportional to the inorganic molar concentration in solution and the volume fraction of inorganic material in the final film), E the evaporation rate (dependent on the relative vapor pressure), L the substrate width, D the fluids physical constant and u the withdrawal speed.

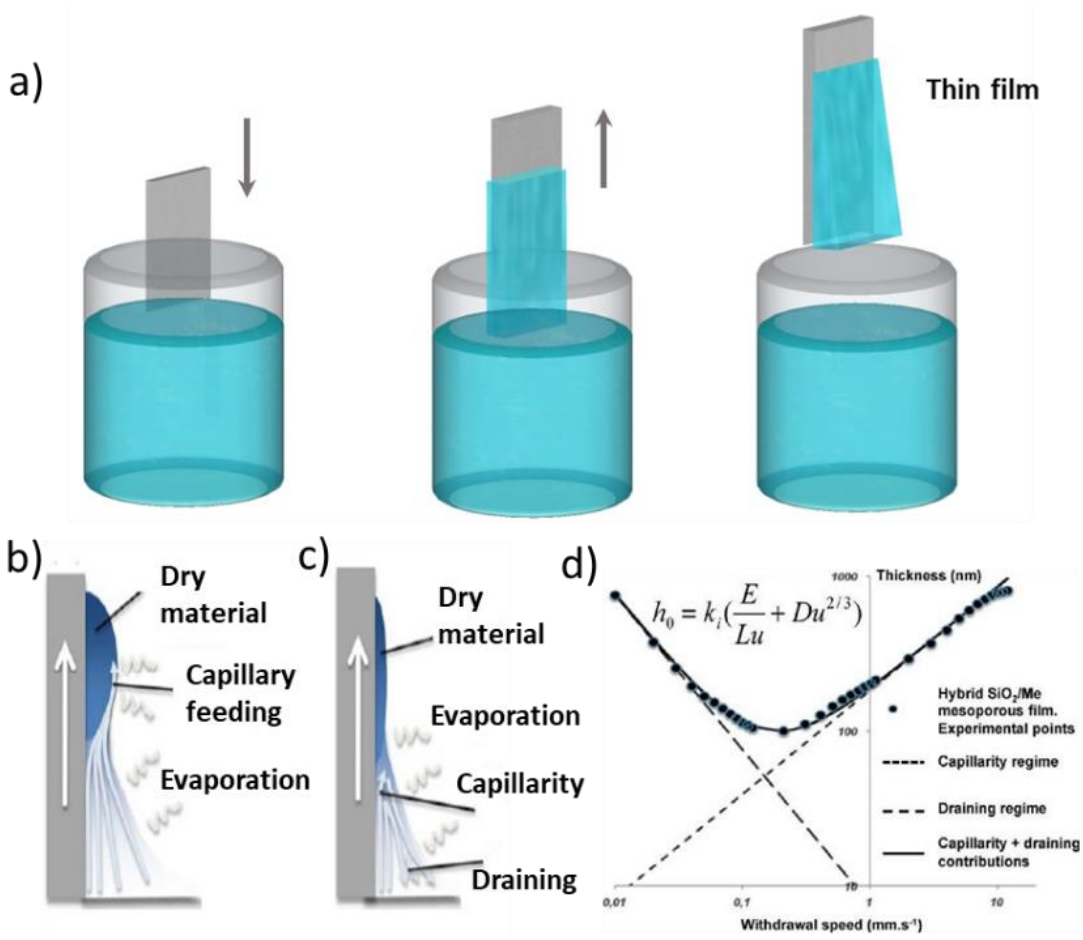



Figure 2. a) A schematic presents a dip coating steps. Scheme of the meniscus for b) Capillary regime and c) Draining regime. d) Plot of the thickness versus withdrawal speed (log-log scale) for a thin film deposited by dip coating[5].

# 4) Spin coating

Spin coating is another convenient method used during the years in the industry and laboratory to deposit a thin film on one side of the surface. In this method, the substrate is rotated at a chosen spin speed (up to 10,000 rpm) to spread the material by centrifugal force. In general, increasing the speed spin induces a drastic decrease in the thickness of the film. The process of spin coating is divided into three stages (see Figure 3):

1- Dropping the initial quantity of the solution on the substrate.
2- Spinning up the solution with the chosen speed and acceleration (rpm).
3- Evaporation of the solvent to form the thin film.

Several parameters contribute to the final thickness of the thin film coated by spin coating, include, centrifugal force (w), the initial concentration volume of the solution used ($C_0$), solvent evaporation rate (e), density ($\rho$), and viscosity of the solution (η), (see Equation (2)).

$$h = C_0\left(\frac{3\eta e}{2(1-C_0)\rho}\right)^{1/3} \omega^{-2/3} \qquad \text{Equation (2)}$$

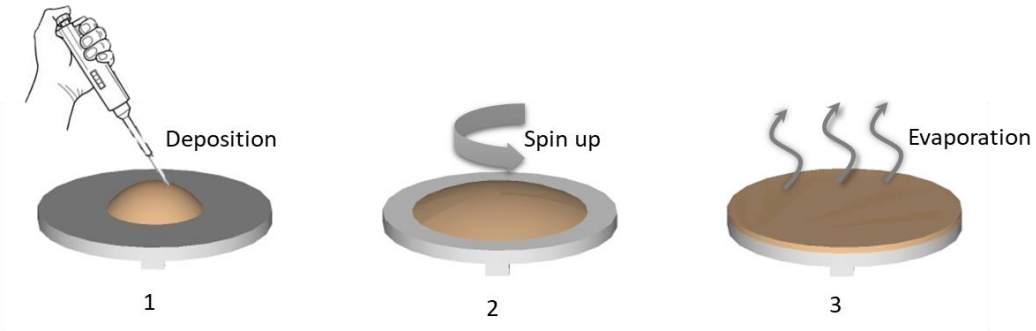



Figure 3. Schematic representing three steps of spin coating

# 5) Evaporation Induced Self-Assembly

The liquid deposition technique is an efficient method to deposit the homogeneous thin film on various substrates in a controlled way as mentioned before. The deposited formulation can be combined with templating agents to produce an organized mesostructured, that can be transformed into organized porosity upon elimination of the templating agent. The self-assembly of the thin film during the liquid deposition technique occurs by evaporation of the volatile solvents. Formation of the mesostructured takes place via self-assembly of the templating surfactants into micelles during evaporation et step called Evaporation Induced Self-Assembly (EISA). The concentration in partially

condensed inorganic precursors and organic molecules progressively increases until it reaches the micellar critical concentration. After this limit, micelles start to form with the hydrophilic outer ring, surrounded by inorganic precursors[4,5,7,8].
The mechanism of EISA has been described by Grosso and coworkers[9] and can be divided into four steps that follow each other during the deposit process (see Figure 4):
1- Rapid evaporation of solvents.
2- Creation of an equilibrium between the water content in the film and the atmospheric relative humidity.
3- Formation and stabilization of the hybrid mesophase.
4- Consolidation of the inorganic network by condensation.

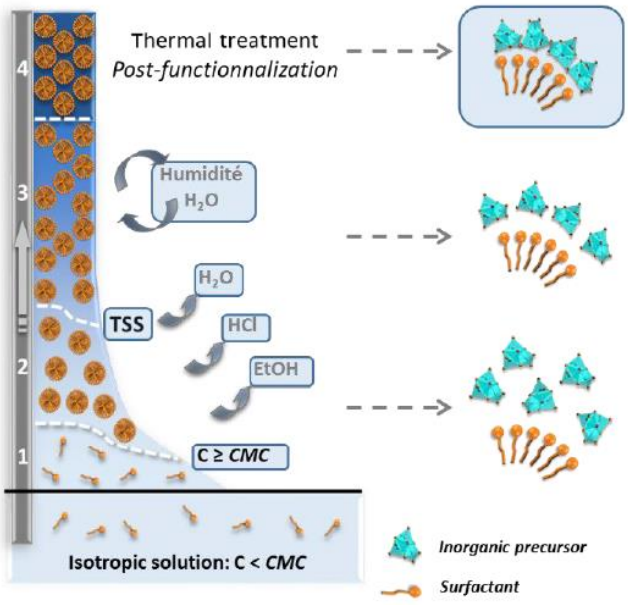



Figure 4. Formation of the thin film by Evaporation Induced Self-Assembly (EISA)[8].

There are two principal categories of agent surfactants: CTAB and Pluronic F127. This phenomenon has been specifically studied for various systems with different surfactants such as $SiO_2$/CTAB[9],[10], $SiO_2$/Pluronics[11], and $TiO_2$/Pluronics[12]. CTAB is a Bromure Hexadecyltrimethylammonium. The second one corresponds to the active tension non-ionic soft materials. This agent is the copolymer amphiphiles from the pluronic family with a chemical formula of ($[PEO]_x$ – $[PO]_y$ - $[PEO]_x$). The difference between these two types of the template is their molecular weights and the size of the pore that they can generate with the inorganic network[8].

# 6) Micro-contact printer machine

This micro-contact-printing (µCP) process machine has been developed by GeSiM-Germany as a NIL system for replicating the patterns onto the substrate by pressure UV-

NIL or/and T-NIL in a controlled way of positions. In this thesis, we recently started to deploy µCP for replicating the alignment superposition 3D nanostructure patterns.
The µCP has consisted of several components (see Figure 5):

1- A transparent substrate holder integrated with heating palate.
2- A printer head moving in the z-direction with a stamp holder fixed to it.
3- An electronic control unit with microcontrollers and pneumatic controls.
4- Air pressure to inflate and pump the mold.
5- A microscopic accessory (camera lenses, or inverse microscope) is linked to the µCP to follow the imprint and adjust the sample if stack position replication requests.

In our case, using the environmental control T-NIL, the µCP was modified by the adopted humidity chamber, constructed by us, to control the input airflow for selecting relative humidity (%) inside the chamber while imprinting.

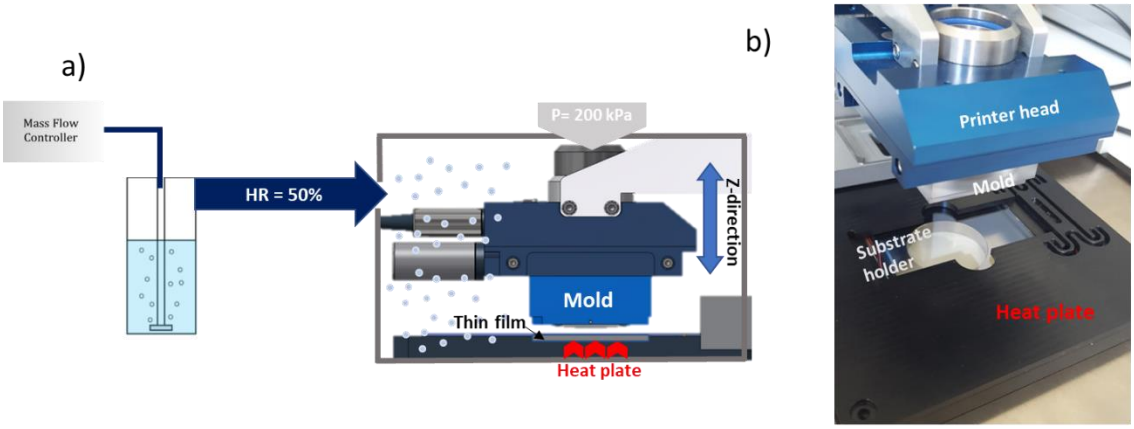



Figure 5. a) Schematic presentation of Micro-Contact Printng (µCP) processing machine. b) The image of heat plate, substrate holder and the mold fixed to the printer head.

# APPENDIX 2 : OPTICAL CHARACTERIZATION

## 1) Ellipsometry

Ellipsometry is a precise characterization technique based on the measurement of the depolarization of a beam of light after being reflected by materials.
This measurement provides the optical properties (refractive index (n) and extinction coefficient (k)), and the thickness (T) of the material. Ellipsometer consists of the source and receiver. The light spot from the source is about 1.2×0.3 $cm^2$ at an angle of 70 degrees. This spot size can be reduced to about 300 $\mu m^2$ by using focus probes. Furthermore, the ellipsometer provides broad-angle measurements by varying the angle from 45 to 70 degrees of incident light (source) and reflected light (receiver). Ellipsometry using variable angle is called ellipsometry spectroscopy which determined the intensity of reflected or transmitted light of the deposited thin film on different substrates (*e.g.* Si, glass, polymer, *etc.*).

The relative changes in amplitude $\boldsymbol{\Delta}$ and phase $\boldsymbol{\psi}$ of the reflected beam are recorded as a function of the wavelength of the incident beam ($\boldsymbol{\psi}$, $\boldsymbol{\Delta}$= f($\boldsymbol{\lambda}$)). Commonly, these materials are one or some stack of thin-film layers. To determine the optical properties of the thin film, a model is built to represent the stacks (Figure 6). The experimental measurements should be fitted by the created stack models by software 'Wase 32'. If the studied material is dielectric and transparent in the visible range, which is the case for most materials studied in this thesis, it can be modeled by a simple Cauchy dispersion model where $n \sim A + B/\lambda^2$.

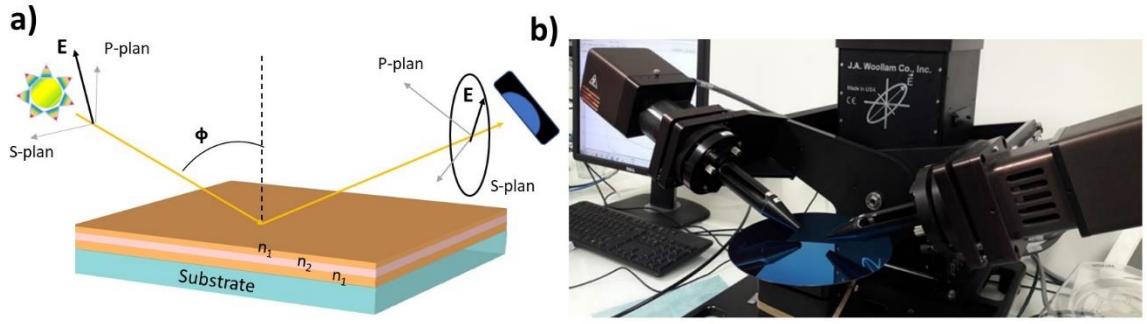



Figure 6. a) Schematic of ellipsometry device. b) Image of the ellipsometer used during this thesis. The polarized light source is on the left and the detector on the right. The ellipsometer is equipped with focus probes to decrease the area analyzed by the beam.

# 2) Environmental ellipsometry

Environmental ellipsometry provides the optical properties and thickness evolution of the thin films as a function of the relative humidity or gas partial pressure. As explained in Chapters 3 and 4, an in-situ ellipsometry chamber has been designed where a controlled flow of gas is injected (see Figure 7). For this reason, accurate mass flow controllers are used. A flow of dry air ($P/P_0 = 0$) is mixed with a flow of air going through a bubbler containing a solvent or water ($P/P_0 = 1$), lead to precise control of the solvent relative vapor pressure. The atmosphere inside the chamber is modified by changing the inlet gas partial pressure by water or other solvents (isopropanol, toluene, ethanol, acetone) at a constant temperature. The measurement results of *in-situ* environmental ellipsometry permit the realization of the isotherm; adsorption and desorption. Moreover, for the mesoporous thin film, this measurement provides information about the pore sizes, the volume of the pores, and the Young modulus of the films. In environmental ellipsometry spectroscopy, the reflected intensity of the film will be measured as a function of this evolution of its refractive index variation by changing the solvent partial pressure and/or relative humidity inside the chamber.

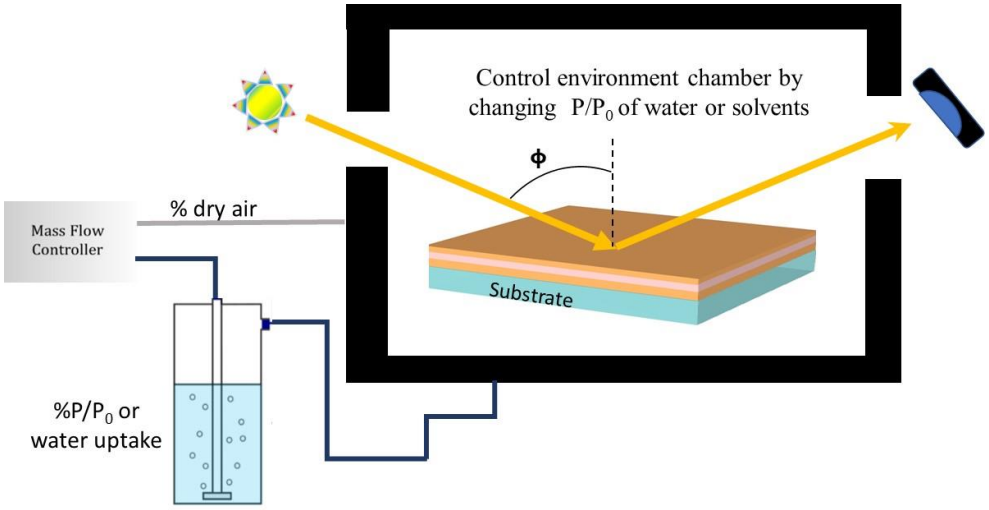



Figure 7. Environmental ellipsometry setup.

# 3) Atomic Force Microscopy (AFM)

An AFM is a scanning microscope that probes a sample surface at nanoscales. It consists of a tip positioned at the end of the cantilever and an optical system using a laser to detect the tip deflections. The laser deviation of AFM provides the topography of the surface down to the atomic resolution. As the tip approaches the surface, attractive forces between the surface and the tip, lead the cantilever to bend toward the surface. The

position sensor works by tracking a laser beam that is reflected from the cantilever. There are two major methods of AFM imaging: Contact AFM and non-contact AFM. In contact AFM, the cantilever scans across a sample with its tip touching the sample surface. Because the tip is in contact with the surface, strong repulsive forces caused the cantilever to bend while passes over the surface features. There are several advantages of this technique however, one of the disadvantages is the damage caused on the surface and grinds down the tip, which reduces the quality of the image. In a non-contact one, the cantilever oscillates just above the surface, and the tip does not touch the surface directly. This kind of interaction between tip and surface induces the oscillation amplitude of the cantilever and constructs the image of the surface topography. Images taken in this thesis from AFM followed the non-contact AFM method.

# 4) Spectroscopy, Spectrophotometry, and Goniometer

In this thesis, the spectroscopic characterization of light (reflection, transmission, and scattering) was performed by either spectrophotometer mounting, optical microscopy, or spectro-polarimetric goniometer.

The reflected light intensity spectrum was performed by Zeiss microscope, 10X and 50X objective with NA = 0.25 and 0.8 respectively, connected to the optical fiber (D = 150 μm) and the spectroscopy device. The detector determines the intensity reflected from the surface, normalized in respect to the mirror.

Furthermore, the spectrophotometer was used to measure the reflectance, transmittance, and scattering from the sample. The spectrophotometer is the analytical tool in the laboratory allowing us to measure the spectra features (R, T, S) normalized by the spectralon plate reference. Collimated light strikes on the diffraction grating and is then separated into the component wavelength.

Moreover, the bidirectional reflectance distribution function (BRDF) was measured with a spectro-polarimetric goniometer for the wide-angle range between 0 to 70 degrees. Here, the spectrum is acquired by a spectrometer, which is linked to the optical head with an optical fiber bundle. To calibrate the target measurements, references are required. Spectro-polarimetric goniometer offers two references; a spectralon plate (for the measurement of the diffusing surface) and a mirror (for the measurement of specular reflection). All the samples are normalized by the mirror in this thesis. Besides, the goniometer includes three angles: the illumination angle ($\boldsymbol{\theta}_{\text{illumination}}$), the detection angle ($\boldsymbol{\theta}_{\text{detection}}$), and the illumination phase angle $\boldsymbol{\phi}$. Detection and illumination angles are determined equal value ($\boldsymbol{\theta}_{\text{illumination}} = \boldsymbol{\theta}_{\text{detection}}$), and $\boldsymbol{\phi}$ was fixed at 90 degrees in all thesis experimental investigations.

# References


[1] C. J. Brinker, In *Chemical Solution Deposition of Functional Oxide Thin Films* (Eds.: Schneller, T.; Waser, R.; Kosec, M.; Payne, D.), Springer Vienna, Vienna, **2013**, pp. 233–261.
[2] C. Gerardin, F. Babonneau, P. Llewellyn, M. Linden, D. Reardon, X. Paquez, D. Grosso, 138.
[3] C. Sanchez, C. Boissière, D. Grosso, C. Laberty, L. Nicole, *Chem. Mater.* **2008**, *20*, 682.
[4] E. Bindini, G. Naudin, M. Faustini, D. Grosso, C. Boissière, *J. Phys. Chem.* 28.
[5] M. Faustini, B. Louis, P. A. Albouy, M. Kuemmel, D. Grosso, *J. Phys. Chem. C* **2010**, *114*, 7637.
[6] M. Faustini, D. Grosso, *Comptes Rendus Chim.* **2016**, *19*, 248.
[7] M. Faustini, D. R. Ceratti, B. Louis, M. Boudot, P.-A. Albouy, C. Boissière, D. Grosso, *ACS Appl. Mater. Interfaces* **2014**, *6*, 17102.
[8] P. C. Sinturel, P. N. Destouches, P. E. Duguet, D. M. Zelsmann, D. M. Faustini, P. D. Grosso, D. L. Favre, 169.
[9] D. Grosso, F. Cagnol, G. J. de A. A. Soler-Illia, E. L. Crepaldi, H. Amenitsch, A. Brunet-Bruneau, A. Bourgeois, C. Sanchez, *Adv. Funct. Mater.* **2004**, *14*, 309.
[10] P. Innocenzi, L. Malfatti, T. Kidchob, S. Costacurta, P. Falcaro, M. Piccinini, A. Marcelli, P. Morini, D. Sali, H. Amenitsch, *J. Phys. Chem. C* **2007**, *111*, 5345.
[11] F. Cagnol, D. Grosso, G. J. de A. A. Soler-Illia, E. L. Crepaldi, F. Babonneau, H. Amenitsch, C. Sanchez, *J. Mater. Chem.* **2003**, *13*, 61.
[12] E. L. Crepaldi, G. J. de A. A. Soler-Illia, D. Grosso, F. Cagnol, F. Ribot, C. Sanchez, *J. Am. Chem. Soc.* **2003**, *125*, 9770.

# PUBLICATIONS AND CONFERENCES

## *Scientific publications*

- ‘Methylated Silica Surfaces Having Tapered Nipple-Dimple Nanopillar Morphologies as Robust Broad-Angle and Broadband Antireflection Coatings’
  Modaresialam Mehrnaz, Jean-Benoît Claude, David Grosso, and Marco Abbarch, ACS Appl. Nano Mater. **2020**, 3 (6), 5231–5239. DOI: https://doi.org/10.1021/acsanm.0c00646

- ‘Sol-gel $TiO_2$ nanoimprinted metasurface combined to hybrid-silica sensitive layers for selective VOC detection with high refractive index sensitivity
  Mehrnaz Modaresialam, Gabrielle Bordelet, Zeinab Chehadi, Martin O’Byrne, Luc Favre, Magali Putero, Marco Abbarchi, David Grosso, ACS Nanoscale, **2021** (Under Revision)

- ‘Nano-imprint lithography processing of inorganic-based materials’
  Mehrnaz Modaresialam, Zeinab Chehadi, Thomas Bottein, Marco Abbarchi, David Grosso, Chem.of.mat. 2021 (Accepted)

- ‘Scalable disordered hyperuniform architectures via nano-imprint lithography of metal oxides’
  chehadi, zeinab; bouabdellaoui, mohammed; Modaresialam, Mehrnaz; Salvalaglio, Marco; Bollani, Monica; Grosso, David; Abbarchi, Marco, 2021, ACS App.Mat. Inter. (Accepted)

## *International conferences*

- ANNIC 2021, Applied Nanotechnology, Nanoscience international conferences: Poster presentation: “Methylated Silica Surfaces Having Tapered Nipple-Dimple Nanopillar Morphologies as Robust Broad-Angle and Broadband Antireflection Coatings”.

- SPIE 2021, The International Society for Optic and photonic, Oral presentation: “Methylated Silica Surfaces Having Tapered Nipple-Dimple Nanopillar Morphologies as Robust Broad-Angle and Broadband Antireflection Coatings”.

- SPIE 2021, The International Society for Optic and photonic, Oral presentation: “Dielectric nano-imprint lithography-sol-gel nanostructured for high-sensitivity refractive index sensing”.
- E-MRS 2021, European Materials Research Society, Oral presentation: “Optical sensing and antireflection coating by a novel method of fabrication sol-gel dielectric nano-morphologies”. (For September 2021 abstract accepted)